Growth Conditions for Large Diameter FZ Si Single Crystals

vorgelegt von

Diplom-Ingenieur Robert Menzel

aus Berlin

von der Fakultät II – Mathematik und Naturwissenschaften

der Technischen Universität Berlin

zur Erlangung des akademischen Grades

- Dr. Ing. -

genehmigte Dissertation

Promotionsausschuss:

Vorsitzende: Prof. Dr. M. Lensen
Berichter: Prof. Dr.-Ing. M. Bickermann
Berichter: Prof. Dr.-Ing. B. Nacke

Tag der wissenschaftlichen Aussprache: 11. Oktober 2012

Berlin 2013

D83

Contents

Abstract (in German language)

Die industrielle Züchtung versetzungsfreier Silizium-Einkristalle nach der Floating Zone (FZ) Methode trifft bei steigendem Kristalldurchmesser auf zwei wesentliche Hindernisse: das Risiko des elektrischen Durchschlags am Induktor und die Gefahr der Versetzungsbildung bzw. das Platzen des Kristalls infolge hoher thermomechanischer Spannungen. Gegenstand der vorliegenden Arbeit ist die Untersuchung geeigneter Wachstumsbedingungen und Methoden zur Überwindung dieser Probleme.

Mit Hilfe eines numerischen Modells des FZ Prozesses werden Lösungsmöglichkeiten für die genannten Probleme erarbeitet und experimentell auf deren Umsetzbarkeit überprüft. Der Einfluss unterschiedlicher Prozessparameter auf die thermischen Spannungen im wachsenden Kristall wird verglichen. Die Möglichkeit des Einsatzes einer zusätzlichen Strahlungsheizung zur Reduzierung thermischer Spannungen wird experimentell untersucht.

Das Risiko des elektrischen Durchschlags lässt sich durch die Absenkung der Frequenz des Induktorstromes verringern. Ein FZ Prozess bei niedrigerer Arbeitsfrequenz für Siliziumkristalle großen Durchmessers ist bisher in der Literatur nicht beschrieben und dessen Realisierung stellt einen Schwerpunkt der Untersuchungen in der vorliegenden Arbeit dar. Es wird ein Versuchsaufbau vorgestellt, der die Züchtung von versetzungsfreien Einkristallen bei reduzierter Arbeitsfrequenz ermöglicht. Dabei wird ausführlich auf das Abschmelzen des Vorratsstabes eingegangen, welches in diesem Zusammenhang eine besondere Schwierigkeit darstellt. Der Einfluss der Frequenz auf die Kristallisationsphasengrenze und die Widerstandsverteilung wird durch Messungen an den gezüchteten Kristallen bestimmt.

Eine zentrale Aufgabe bei der Entwicklung eines Prozesses zum Züchten großer Durchmesser ist die Gestaltung geeigneter Induktoren. Hierzu werden Ergebnisse der dreidimensionalen numerischen Simulation der Jouleschen Wärmeverteilung infolge der speziellen Induktorgeometrie vorgestellt.

Abstract

The industrial growth of dislocation-free silicon single crystals with large diameter by the floating zone (FZ) method meets two major drawbacks: the increasing risk of arcing at the inductor and the generation of dislocations or cracking of the crystal due to high thermo-mechanical stress. Subject of this thesis is the investigation of suitable growth conditions and methods to overcome these limiting factors.

With the help of a numerical model of the FZ process solutions for these problems are investigated and examined on feasibility by experiments. The influence of different process parameters on the thermo-mechanical stress in the growing crystal is compared. The possibility to use an additional radiation heater to reduce thermal stress is examined.

The risk of arcing can be reduced by lowering the frequency of the inductor current. A FZ process at reduced working frequency for large-diameter silicon crystals is not yet described in the literature and its implementation is a key aspect of this thesis. Detailed attention is drawn to the melting behavior of the feed rod, as this is a particular difficulty in this context. Furthermore, it is elaborated on the impact on the crystallization interface and the resistivity distribution on the basis of measurements on crystals grown at reduced frequency.

An essential task in the development of a process for the growth of large-diameter Si crystals is the design of a suitable inductor. Results from three-dimensional numerical simulations of the distribution of the Joulean heat due to the specific shape of the inductor are presented.

Structure of the Thesis

In the first chapter the floating zone (FZ) process is described as it is currently used in the industry for the production of high purity silicon crystals with large diameter. In this context it is elaborated on the technological limitations and problems observed in the growth of silicon crystals with a diameter of up to 8 inches.

The second chapter deals with the mathematical model of the FZ process as known from the literature. Hence, it is the basis for explanatory approaches made on experimental observations described in later chapters. Furthermore, the basic equations and boundary conditions in the numerical simulations are given here. The program implemented for the computation of the phase boundaries is described.

In chapters three and four the impact of the shape of the inductor on the temperature field and the thermo-mechanical stress in the crystal is studied by means of a three-dimensional electromagnetic and an axisymmetric heat transfer model. The use of an additional radiation heater to reduce thermal stress in the crystal is examined numerically and by an experiment. Results from temperature measurements at different gas pressures are presented. It is concluded that neither a modification of the shape of the inductor nor an increase of the filling gas pressure in the chamber is appropriate to sufficiently lower the increased risk of arcing in the growth of crystals with larger diameter.

Consequently, the fifth chapter is dedicated to the FZ growth of crystals at reduced working frequency, this being another measure to reduce the risk of arcing. It is elaborated on the impact on the melting behavior of the feed rod and the influence of the increased EM forces on the molten zone. Results from growth experiments are presented.

Nomenclature

Table 1-1: List of Symbols

Symbol	Unit	Description
A	A/m	magnetic vector potential
B	T	magnetic field
C	N/m^2	elastic stiffness
c_p	J/(kg·K)	specific heat capacity
E	N/m^2	Young's modulus
E	V/m	electric field
f	Hz	frequency
F	N/m^2	surface force density
f	N/m^3	volume force density
g	m/s^2	gravitational constant
h	J/kg	latent heat of fusion
I	A	electric current
J	A/m^2	volume current density
j	-	imaginary unit
i	A/m	surface current density
k	$W/(m^2K)$	heat transfer coefficient
K	1/m	curvature
L	m	length
n	-	surface normal
p	N/m^2	pressure
q	W/m^2	heat flux density
r	m	radial coordinate
R	m	radius
T	K	temperature
u	m/s	velocity
U	V	voltage
v	m/s	pull speed
z	m	axial coordinate

α	°	angle
α	1/K	coefficient of thermal expansion
β	°	growth angle
γ	N/m	surface tension
Γ	-	boundary
δ	m	skin depth
ε	-	emissivity
η	kg/(ms)	dynamic viscosity
λ	W/(mK)	heat conductivity
μ	Vs/(Am)	permeability
ν	m/s	pull rate
ν	-	Poisson's ratio
ρ	kg/m^3	density
σ	N/m^2	mechanical stress
σ	S/m	conductivity
ϕ	V	scalar potential
ω	1/s	angular frequency
Ω	1/s	rotation rate
ϵ	-	elastic strain

Vectors and tensors are denoted by boldface letters (**x**). Complex-valued quantities are underlined ($\underline{x}$)

List of Abbreviations

CZ   Czochralski method
EM   Electromagnetic
ETP   External triple point
FEM   Finite-element method
FZ   Floating zone
IKZ   Institute for Crystal Growth
ITP   Internal triple point
LPS   Lateral photo-voltage scanning
PLS   Photoluminescence scanning
HF   High frequency

1. Introduction

1.1 The FZ Process

The highest purity of silicon crystals grown from the melt can be achieved with crucible-free methods. A contamination with oxygen, carbon or from any crucible material is avoided. Among the crucible-free growth techniques the floating zone (FZ) method stands out for its ability to produce dislocation-free single crystals with large diameter. Large crystals of high purity have a number of scientific and industrial applications. One extraordinary example is the widely noticed international Avogardo project launched in the year 2003. The Avogardo project was an attempt to determine the Avogadro constant and define the SI unit kilogram based on the number of atoms in a sphere of highly enriched mono-isotopic silicon [1]. The nominal diameter of a 1 kg ^{28}Si sphere is ≈93.6 mm and, hence, a crystal of at least this diameter was needed. The growth of a crystal with the required specifications was possible using the FZ method.

For the semiconductor industry the specific electronic properties of silicon crystals grown by the FZ method are of interest. Due to the high purity and the achievable high resistivity, the wafers cut from those crystals are mostly used as substrates in discrete devices for high-power applications like power MOSFET's or power thyristors. FZ silicon can be found e.g. in rectifiers, electrical trains or inverters for windmill and photovoltaic installations.
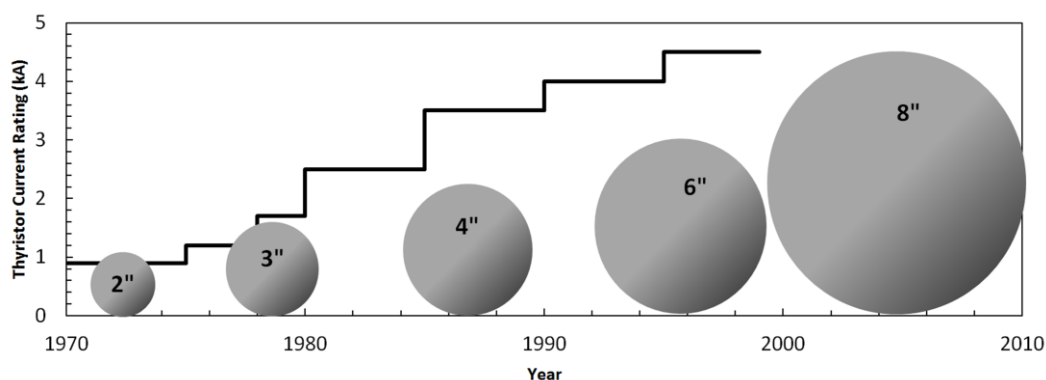

Figure 1-1   Progress of the maximum available FZ wafer diameter and development of the supported current rating of power thyristors. Source:[3]

Some of the devices made from FZ crystals are manufactured from one single wafer. Here the diameter of the wafer can be crucial for the device performance. In a power thyristor the supported direct current is determined by the diameter and the resistivity of the used silicon wafer. First thyristors were based upon silicon wafers with a diameter of 33mm and supported a direct current of up to 1000A [2]. Due to the progress in the FZ wafer development, thyristors with higher current ratings were available (see Figure 1-1). Thyristors based on 6" wafers, supporting a direct current of 4500A, have been developed [3]. These high current levels are required e.g. for power distribution systems such as high-voltage DC (HVDC) transmission networks.

The basic principle of the FZ method is to move a molten zone vertically through a feed rod in order to grow a crystal below the molten zone. In practice feed rod and crystal are continuously moved downwards (see Figure 1-2 a,b). The heat source used to achieve the molten zone can be an inductor or a radiation furnace. In the classical FZ method for smaller crystal diameters the molten zone is approximately cylindrical and of the same diameter as feed rod and crystal (see Figure 1-2a). According to the Heywang criterion for the stability of cylindrical liquid zones the maximum zone height for silicon is about 16mm [4]. The maximum crystal diameter that can be pulled by the classical FZ method is smaller than 15mm. To grow crystals with larger diameter the needle eye technique was developed, which is depicted in Figure 1-2 b.

In the needle eye technique the melting front is connected to the lower melt volume by a liquid bridge partly narrower than crystal and feed rod. The shape of the molten zone is mainly governed by the capillary pressure and the hydrostatic pressure. The heat source is a high frequency (HF) pancake inductor with a central hole that must closely surround the liquid neck to keep it molten. Due to the high heater power necessary in a process for crystals with large diameter it is no longer feasible to use solely radiative heating as the transmission efficiency is too low.

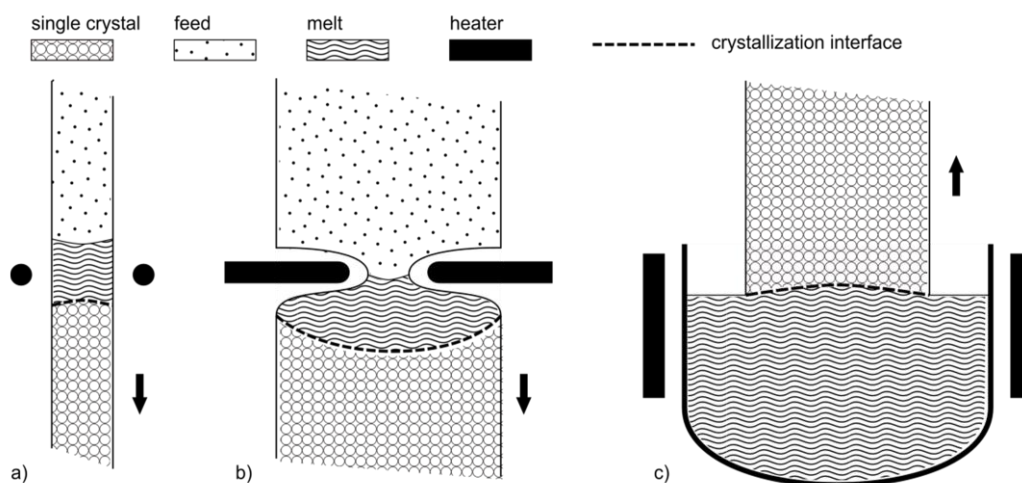**Figure 1-2**   Configurations for the growth of Si single crystals.
                     (a) The classical FZ method
                     (b) The FZ method with needle eye technique.
                     (c) The CZ method.

In the Czochralski (CZ) method a crystal is pulled from a melt in a crucible (see Figure 1-2 c). Similar to the FZ method, the CZ method allows the growth of large dislocation-free Si single crystals but the grown crystal is inevitably contaminated by the crucible material.

The growth of larger silicon crystals by the FZ method is technologically challenging and more expensive. The price per square inch of a wafer is increasing with the diameter. This is mainly a consequence of the high quality of the feedstock material required for the FZ growth. Long cylindrical rods of constant diameter, free of voids, cracks, inclusions and contaminations are required. A constraint in the process is that a certain ratio between the feed rod diameter and the crystal diameter must be maintained and, hence, ingots with large diameter are required for the growth of large-diameter crystals. The chemical vapor deposition (CVD) for large ingots is costly. Low deposition rates are required to achieve the smooth surfaces and crack-free feed material.

Nevertheless, the huge cost saving of using larger wafers outweighs the increase of the costs per square inch. For wafers from FZ crystals the 6 inch diameter is widely established in the industry. The subsequent step in wafer size is, driven by production line requirements, the 8 inch wafer. The first FZ crystal of 8 inch diameter was grown in 2000 by the Wacker Siltronic AG. The market demand for FZ crystals of 8 inch diameter is continuously increasing and only a few competitors in the market are able to master the complex process technology necessary for such large crystals.

Large FZ silicon crystals with 8 inch diameter would be needed for the standard 156mm x 156mm pseudo-square wafers used in photovoltaic applications. FZ silicon has a huge technological potential in the solar energy sector. Solar cells from crystals grown by the FZ method are of higher efficiency than solar cells from crystals grown by the CZ method. The higher efficiency of the FZ material is a result of the higher purity, the absence of light induced degradation and the longer minority carrier lifetime. However, FZ silicon is rarely used for solar cells at present and the vast majority of the monocrystalline wafers for solar applications are manufactured by the CZ method.

The higher efficiency is compromised by the high production costs due to the complexity of the FZ process. There are constant efforts to make FZ silicon competitive to CZ silicon by lowering the costs of the feedstock material or finding means to use ingots of lower quality in the process, e.g. feed rods from EM casting [5]. Another approach is to melt cheaper silicon particulates or granules instead of an ingot [6], [7]. A survey on the applicability of the FZ method in the solar cell production is given in [8].

The initial technique that allows to grow a dislocation-free single crystal is the Dash method named after its inventor William C. Dash [9]. At the start of the process a molten silicon drop is formed on the tapered preheated feed rod and is contacted with a seed crystal of a defined crystal orientation. Once the top of the seed is molten and a smooth solid-liquid interface has formed, the seed is pulled downwards with a rather high pull rate (8-16mm/min), whereby the heater power is reduced. In that way a thin neck with 2-3 mm diameter is grown in which, as a result of the low thermal stress in such a thin neck, the movement and multiplication of dislocations is diminished [10]. During neck growth, existing line dislocations propagate mainly in $\langle 110 \rangle$ direction and will vanish for any other pulling direction. As the dislocations propagate along the $\langle 110 \rangle$ direction, some dislocations will remain for this growth direction, even with the Dash method.

After the thin neck has gained a few centimeters of length, all dislocations are removed from the thin neck and no new dislocations appear due to their high energy of generation. Subsequently, by controlling the growth rate by the heater power, the crystal pull speed and the feed rod supply rate, the diameter of the crystal is increased until the target diameter is reached. The pull speed is in the range of about 2-5 mm/min, depending on the crystal diameter. Typically the growth of crystals with larger diameter requires a lower pull speed.

The absence of dislocations is a precondition for the growth of single crystals by the FZ method. Only a dislocation-free crystal can withstand the high thermals stress without generation of dislocations. If a first dislocation occurs, the consequence is strong dislocation multiplication leading to a polycrystal.

The FZ process setup is depicted in Figure 1-3. The crystal and the feed rod are fixed at separate spindles. The weight of large crystals standing on the thin neck can become a serious issue during the growth. A crystal support system helps carrying the weight of the heavy crystal, the thin neck alone could not sustain. Although the process is more and more automated by the help of video monitoring and feedback control systems, the crystal grower is still needed, especially in the more complex start- and end-cone phases. The crystal grower mainly controls crystal pull speed, feed push rate and heater power. Crystal and feed rod are rotated to provide axial thermal symmetry required for the growth of a cylindrical crystal, homogeneous melting of the feed rod and mixing of the melt.

Melt mixing is important for a homogeneous distribution of dopants in the crystal. For the use in electronic devices, the resistivity should deviate only a few percent and a low radial resistivity variation across the wafer is desired.

As a protective atmosphere the growth chamber is commonly filled with argon gas. To incorporate dopants into the melt phosphine (PH_3 for n type) or diborane (B_2H_6 for p type) can be blown to the free melt surface.

A more expensive but more sophisticated and precise doping method is the neutron transmutation doping (NTD) method. In the NTD method an undoped crystal is exposed to neutron irradiation in a nuclear reactor. The neutron capture of the silicon isotope ^{30}Si forms an unstable ^{31}Si isotope. ^{31}Si subsequently transmutes to phosphorus ^{31}P leading to an n-type material. Unfortunately there is no such reaction for p-type doping.

Besides, a small amount of nitrogen (<1%) is added to the gas atmosphere for two purposes. Firstly, nitrogen suppresses the aggregation of single point defects[11]. Single point defects incorporated during the growth do not necessarily affect the performance of a semiconductor but their aggregation to large clusters during cooling of the crystal is critical and may deteriorate the quality of an electronic device [12]. Secondly, nitrogen lowers the risk of arcing. Arcing prematurely terminates the process and occurs if the voltage at the inductor exceeds the breakdown voltage of the gas atmosphere.
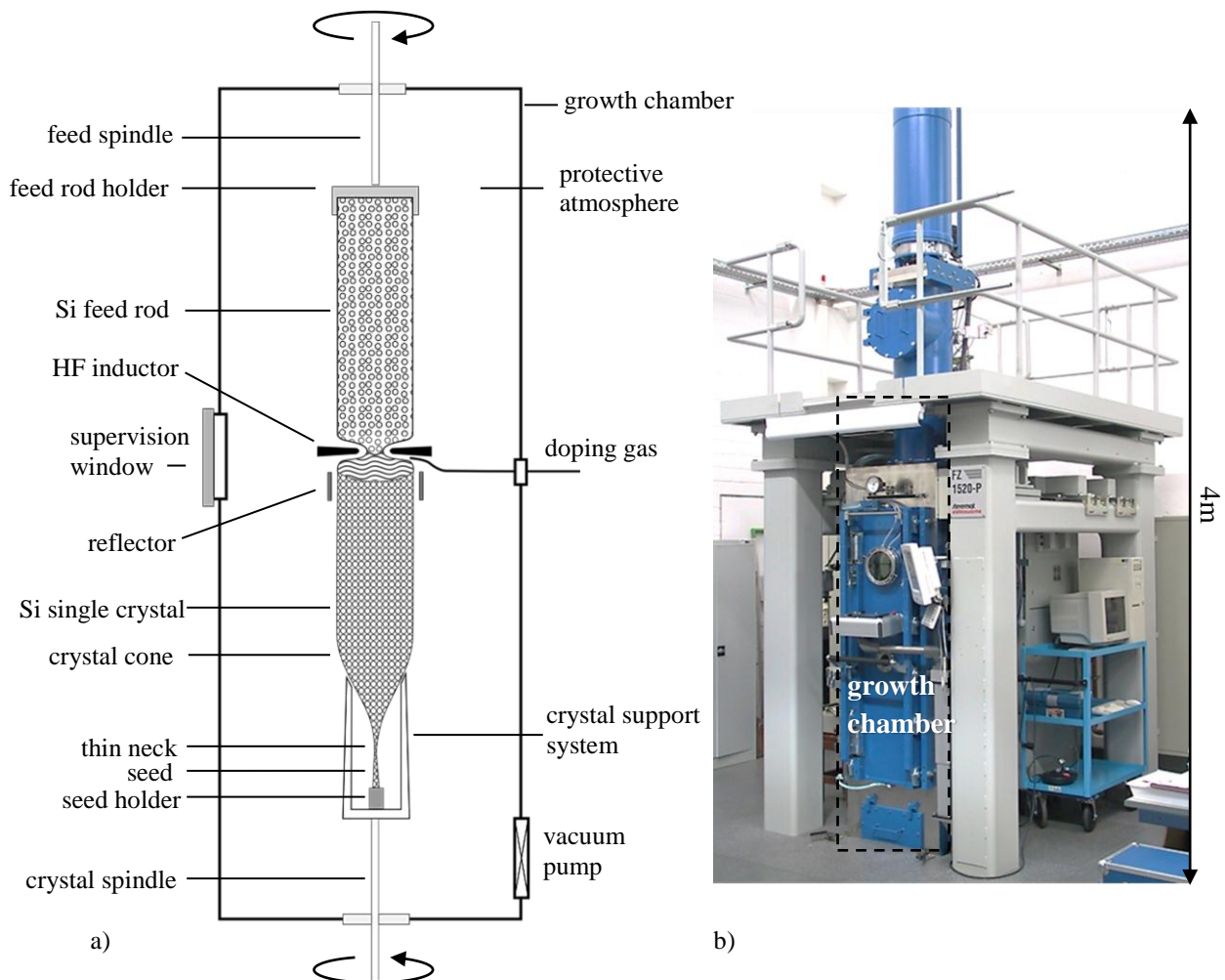

Figure 1-3   The FZ process for large-diameter Si single crystals.
                    a) Scheme of the FZ process
                    b) FZ crystal puller at the IKZ-Berlin.

1.2   Technological Limitations

The risk of arcing is a fundamental problem when growing crystals with larger diameter. The larger the diameter of the crystal, the more inductively induced power is necessary and the higher is the voltage needed at the inductor terminals. The width of the slit in the inductor cannot be increased as a high symmetry of the induced power distribution is necessary, in particular in the growth of large-diameter crystals

Adding nitrogen to the argon gas atmosphere suppresses the risk of arcing only to some extent. Adding more nitrogen has no additional positive effect or may have adverse effects, e.g. the precipitation of silicon nitride at the crystal surface. Growing dislocation-free crystals with large diameter in vacuum is not possible as evaporated silicon accumulates at the cold inductor and solid particles will fall back to the molten zone and cause generation of dislocations.

Commonly a high frequency between 2.6 to 3MHz of the inductor current is used. Such high frequencies are necessary as a sufficiently small penetration depth of the electromagnetic (EM) field is required to ensure a proper melting of the feed rod. A substantial improvement could be achievable by lowering the frequency. At a lower working frequency less voltage at the inductor is required to generate the necessary Joule power. Consequently, a higher power output required for a larger crystal diameter could be obtained without arcing. However, the application of a lower working frequency implies the necessity for a method to ensure a proper melting of the feed rod.

Another possibility to lower the risk of arcing is to increase the pressure of the gas atmosphere. Unfortunately, higher gas pressure promotes convective cooling of the crystal and can increase the thermal stress.

It is a particular challenge to avoid too high thermal stress in the crystal during growth. If the thermal stress exceeds a critical value, the generation of dislocations or even cracking of the crystal will inevitably end the process. To reduce thermal stress commonly concentric reflector rings of copper or silver are applied. (see Figure 1-3).

The design of the inductor is one of the most crucial parts in the development of a large-diameter process. The inductor must provide a suitable power distribution during all stages of the process. The shape must allow growing the crystal cone and still be adequate to provide a power distribution for the dislocation-free growth on the target diameter. Furthermore, the shape of the inductor affects the distribution of the electromagnetic forces. Therefore, the shape of the inductor is a factor in nearly all relevant phenomena like arcing, thermal stress or melt mixing.

There is no known physical limit for the diameter of a silicon crystal but the technological effort is heavily increasing with the diameter of the crystal.

1.3   Objectives of the Present Work

The main objective of the current work is to identify suitable measures to overcome the known technological problems in the growth of large-diameter crystals and evaluate their impact experimentally and by numerical simulation. The focus is on issues encountered in the development of a FZ process for crystals with 8 inch diameter at Topsil Semiconductor A/S. The major drawbacks are the risk of arcing and the high thermal stress in the crystal.

The objectives of the current work include:

- Experimental investigation on the possibility to reduce the risk of arcing by using a lower working frequency of the inductor current than commonly used in the industrial growth of silicon single crystals with the FZ method.

- Investigation on the problem of cracking in large-diameter crystals. Examine methods to lower the thermal stress in the growing crystal. Evaluation of the role of convective cooling and the pressure of the gas atmosphere on the thermal stress level in the growing crystal

- Elaboration on the influence of the shape of the inductor, with regard to the growth of large-diameters crystals, by means of numerical simulation.

For the investigations a numerical model of the FZ process is implemented in the software package COMSOL Multipysics^{TM} and the numerical computing environment Matlab^{TM}. The model allows the calculation of the EM field, the temperature field and the thermal stress in the crystal. The model is used for parametric studies and the obtained results are compared to measurements and to results published in existing works on numerical modelling of the FZ process.

The main purpose of the numerical model is to allow a more detailed understanding of the results obtained in the experimental investigations conducted within this work. While recent publications are often focused on the numerical implementation of different features of the FZ process, the investigation of the experimental feasibility of the proposed methods is a key aspect in the current work.

Parts of this work have already been published in [13] and [14].

1.4   Related Work

A comprehensive historical survey on the emergence of the modern growth techniques for Si single crystals, starting from the growth of small germanium crystals to large-diameter silicon crystals, can be found in the work of Zulehner [15]. A more detailed description of the inductively heated FZ process is given by Lüdge et al. in [10].

Since the first usage of inductive heating during FZ growth with the needle eye technique, it was clear that high frequencies in the RF region are necessary to properly melt the feed rod. In 1987 Gupta et al. [16] experimentally investigated the possibility to melt the feed rod using lower working frequencies in a 200 - 500 kHz range. They reported that it is impossible to start the process due to the formation of outer solid shells at the tapered feed rod. In an attempt to improve the melting behavior additional reflectors in the vicinity of the melting front were applied but without success.

The impact of different reflectors types for different purposes has been intensively studied by the group of Riemann at the Institute of Crystal Growth Berlin. Rost et al. [17] used reflectors on top of the inductor to positively influence the unfavorable melting behavior of as-deposited feed rods with a rough surface structure.

Lüdge et al. [18] experimentally investigated the application of such reflectors as a mean to reduce the thermal stress in the crystal. The reflector is located below the inductor, in the vicinity of the upper crystal rim. The influence of the height of the reflector and its distance to the crystal rim on the deflection of the crystallization interface was studied. The results of the measurements are compared with the results from a numerical model presented by Riemann et al. in [19]. The numerical model allows the calculation of the temperatures and thermal stress in the crystal assuming axial symmetry of the FZ system.

Several groups have presented chains of models for the numerical calculation of the relevant physical quantities in the FZ process for large-diameter crystals. This includes the calculation of electromagnetic, thermal, thermo-elastic, fluid-dynamic and dopant concentration fields.

Within the cooperation between the Institute of Electrotechnology at the University Hannover and the Department of Physics at the University of Latvia, a very substantial chain of models has been developed. In [20], Mühlbauer et al. give an overview of their system of coupled mathematical models for the calculation of the EM field, interface shape, heat transfer, thermal stress, transient fluid flow and dopant segregation during FZ growth. This axisymmetric model was developed by Mühlbauer, Virbulis and Muiznieks and is explained in detail in the works [21–24].

Raming [25] calculated the influence of different types of magnetic fields on the fluid motion in the molten zone. He also shows the influence of different working frequencies on the melt flow and the dopant concentration in the crystal. Working frequencies between 1.5 MHz and 4MHz are considered. It is found that with a lower frequency of the inductor current the radial resistivity profile could be made more homogeneous [26].

Ratnieks presented in [27] , [31] a more sophisticated axisymmetric chain of models, which is adapted to the needs of modelling the FZ process for large-diameter crystals up to 8 inch. As the electromagnetic field in the FZ system is inherently three dimensional, three-dimensional calculation approaches are of higher accuracy. In [28] Mühlbauer et al. use the boundary element method (BEM) to calculate the three-dimensional electromagnetic field in the FZ system. Consequently, in [29] and [30] Ratnieks et al. show the influence of the three dimensionality of the electromagnetic field on fluid flow and resistivity variations in the crystal. To study substantially time-dependent process phases like the growth of the start and the end cone of the crystal, Rudevic*s* et al. enhanced the stationary model to a fully transient approach [32].

A chain of models for the simulation of the FZ process in axisymmetric approximation was developed in the group of Dupret. Details of the model are presented in the Ph.D. theses of Assaker [33] and Bioul [34]. The software package developed is commercially available under the name FEMAG-FZ and covers the calculation of electromagnetic field, heat transfer, melt flow and thermal stress in the FZ system.

In [35] Larsen et al. use an axisymmetric numerical model to investigate the impact of convective cooling on the temperature distribution and generation of point defects in the crystal. Details of the model are published in the Ph.D. thesis of Larsen [36]. The impact of convective cooling as a function of the pressure of the gas atmosphere is modeled by using an analytical function for the heat transfer coefficient. Measurements of the shape of the crystallization interface in crystals grown at gas pressures between 1.9 bar and 3.2 bar are compared to the calculated interface shapes.

2.   Mathematical and Numerical Models

2.1   Simulation Procedure

In this chapter the mathematical background of the FZ process is described. The mathematical model is the basis for the explanation of experimental results and the numerical simulations conducted. For understanding and the efficient development of a process for large-diameter crystals, numerical simulation is indispensable as in a growth experiment many physical quantities, like electric current or temperature, are hardly accessible for observation or measurement. A particular challenge in modelling the FZ process is to consider the various couplings between the relevant physical phenomena and their interaction with the shape of the phase boundaries. Sophisticated chains of numerical models for the simulation of the FZ process have already been developed by different authors (see section 1.4)

In this work a numerical model of the FZ process is used, that has been implemented in the software package COMSOL Multiphysics and MATLAB. COMSOL is an analysis software for partial differential equations and is based on the finite element method (FEM). MATLAB is a computing environment which allows programming of numerical algorithms in its own language. COMSOL provides an extensive interface to MATLAB. The software COMSOL has shown to be appropriate to simulate HF induction heating during FZ growth.

For the simulations conducted a MATLAB script was written, which allows coupling between separate physical models, according to the features of the FZ process. The computation of the phase boundaries was implemented in this program.
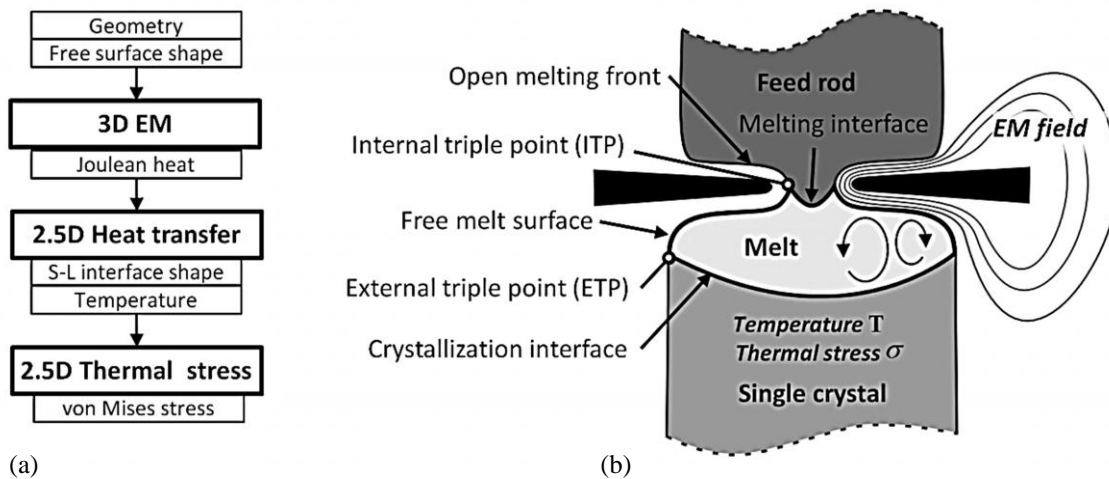
Figure 2-1   Simulation of the FZ process.
(a) Chain of numerical models
(b) Phase boundaries and calculated physical quantities in the FZ process. In the model the
    shape of the free melt surface and of the crystallization interface are calculated.

An overview of the model chain is depicted in Figure 2-1a. The model covers the calculation of electromagnetic fields, heat transfer and thermal stress in the growing crystal. Each step involves solving one or a system of coupled differential equations in COMSOL. The EM field and Joulean heat distribution is obtained using a 3D model. For the calculation of the temperature field and the thermal stress axial symmetry of the FZ system is assumed. The simulation of the temperature field in the growing crystal involves calculation of the crystallization interface.

By a common definition the position of a point at the lower tri-junction of crystal, melt and gas atmosphere is called external triple point (ETP). By a similar definition a point at the intersection line of free melt surface, open melting front and melting interface is called internal triple point (ITP). In the model used the position of these points are fixed to approximate values known from measurements conducted during a corresponding process.

The aim of the following sections in this chapter is to state, which physical theory was used, how it was applied to describe the FZ process and which assumptions were made. The differential equation(s) solved and the boundary conditions set in the numerical simulations are given.

2.2   Electromagnetic

The heat source in the inductively heated FZ process is the Joule heat generated in the silicon by the HF inductor. The sinusoidal voltage applied at the inductor terminals drives an alternating current in the inductor. The current generates an EM field in the space between inductor and the silicon. The EM field induces eddy currents and Joule heat in the silicon.

The Joule heat distribution influences the temperatures in the melt and in the growing crystal. It is governed by Maxwell's equations and can be controlled by the electric process parameters and the shape of the inductor. The shape of the inductor cannot be axisymmetric and, hence, the induced power distribution is not of axial symmetry. The crystal is rotated to achieve an approximately axisymmetric temperature field necessary for the growth of a cylindrical crystal. However, the remaining deviation from axial symmetry in combination with crystal rotation causes local temperature fluctuations and is a potential risk for the dislocation-free growth.

For induction heating during FZ growth a high working frequency in the radio frequency (RF) range, typically f=3MHz, is applied. This causes a distinct skin effect in the copper inductor and the hot silicon, which has a high electrical conductivity at high temperatures. It is well known that in this case the current density is exponentially decreasing to 1/e of its value at the surface after a skin depth of:

$$\delta = \frac{1}{\sqrt{\pi \mu f \sigma}}.$$

μ magnetic permeability
f frequency
σ electric conductivity
                                                                                                    (2.1)

The skin effect arises as the eddy currents induced by an alternating magnetic field produce a field, which opposes and partly compensates the generating field, reducing the net magnetic flux and causing a decrease in the current flow as the depth increases. Eq. (2.1) is a good approximation for a conductor of arbitrary shape if the radii of curvature of the conductor cross section are significantly larger than δ. In the current work lower working frequency is investigated. However, the frequencies considered are still in the MHz range and the skin depth is much smaller than the dimensions of the conductors in the FZ system. Table 2-1 lists the skin depth for the frequencies considered and the involved materials.

Table 2-1 Skin depth

		skin depth δ [mm]		
	σ [S/m]	f = 3 MHz	f = 2 MHz	f = 1.7 MHz
copper	$6 \cdot 10^7$	0.037	0.046	0.05
liquid silicon	$1.2 \cdot 10^6$	0.26	0.32	0.35
solid silicon	$5 \cdot 10^4$	1.3	1.56	1.72

The EM field obeys Maxwell's equations, which are described in detail in the standard works for electrodynamics, eg in [37]. To solve 3D eddy current problems Comsol uses the electromagnetic vector potential formulation. The general assumption is a time harmonic EM field due to a sinusoidal excitation with an angular frequency ω. It is assumed that all materials in the FZ system have constant, isotropic properties. Furthermore, no media with a relative permeability other than 1 is considered. Maxwell's equation for the time-harmonic EM field can then be written as:

$$\mu_0 \underline{\mathbf{J}} = \nabla \times \underline{\mathbf{B}}$$

$\underline{\mathbf{B}}$	magnetic field
$\underline{\mathbf{J}}$	current density
μ_0	vacuum permeability

(2.2)

In a good conductor the term for the displacement current density is much smaller compared to term for the conduction current density. For this case the relation between the volume current density and the electric field intensity can be written as:

$$\underline{\mathbf{J}} = \sigma \underline{\mathbf{E}}$$

$\underline{\mathbf{E}}$	electric field
σ	electric conductivity

(2.3)

The electric and the magnetic field are coupled. The current flowing on the inductor generates a magnetic field in the vicinity of the inductor. The time variation of this magnetic field induces an electric field that causes eddy currents flowing on the silicon surfaces. The magnetic field generated by the eddy currents modifies the source current distribution on the inductor.

By definition the magnetic field and the electric field can be expressed in terms of the magnetic vector potential and the electric scalar potential as follows:

$$\underline{\mathbf{B}} = \nabla \times \underline{\mathbf{A}}, \quad \underline{\mathbf{E}} = -\nabla \underline{\phi} - j\omega \underline{\mathbf{A}}.$$

$\underline{\mathbf{A}}$	vector potential
$\underline{\phi}$	electric scalar potential

(2.4)

The combination of Maxwell's eq. (2.2) and Ohm's law eq. (2.3) with the definitions of the potential yields:

$$\nabla \times \left(\mu_0^{-1} \nabla \times \underline{\mathbf{A}} \right) + \sigma \left(\nabla \underline{\phi} + j\omega \underline{\mathbf{A}} \right) = 0.$$

(2.5)

This differential equation describes the EM field in terms of the vector potential for the three spatial directions. There are four unknowns in the model: the three components of the vector potential and the scalar electric potential. Another equation is needed, which is obtained by requesting the principle of current conservation:

$$\nabla \cdot \underline{\mathbf{J}} = 0.$$

(2.6)

By taking the divergence of Ohm's law eq. (2.3) and with respect to eq. (2.4) this equation can be written as:

$$-\nabla \cdot \sigma \left(j\omega \underline{\mathbf{A}} + \nabla \underline{\phi} \right) = 0$$

(2.7)

The vector potential **A** is not well-defined by the eq. (2.4). Due to the fact that the curl of a gradient field vanishes, the gradient of an arbitrary spatial function could be added to **A** without changing **B**. In general, a gauge fixing is required to provide uniqueness of the solution. Enforcing the Coulomb gauge adds another equation to the system:

$$\nabla \cdot \underline{\mathbf{A}} = 0 \tag{2.8}$$

From the known vector potential the magnetic and the electric field can be obtained from eq. (2.4).

Due to the distinct skin effect the EM field in the conductors is concentrated in a thin skin layer near the surface. As can be seen in Table 2-1, resolving the exponential decrease of the induced volume current density in the liquid silicon at f=3MHz would require a fine FEM mesh with several layers in a region of only 0.35mm. To avoid the need to resolve the exponential decrease of the current in the skin layer the so called standard impedance boundary condition (SIBC) is applied. Detailed derivations of the SIBC or Leontovich boundary condition are given in [38–40]. It is applicable if the skin depth is far less than the thickness of the conducting structures.

The SIBC relates the components of the electric field and the magnetic field tangential to the surface via a surface impedance. The SIBC boundary condition is imposed to model the interfaces between the conductors and the gas atmosphere in the FZ process. Enforcing the SIBC at the surfaces allows removing the inner volume of the conductors from the model and, hence, reducing the number of unknowns in the numerical simulation. The system of equations for the EM field needs to be solved only in the domain bounded by the surfaces of the conductors and an artificial bounding surface (see Figure 2-2).

The distribution of the surface current density on the silicon surfaces as well as on the inductor is calculated in the model. A voltage across the inductor terminals is provided. Thus, at the outside edges of each of the inductor terminals an electric potential is defined. A normalized value of 1 Volt is chosen as the potential difference between the inductor terminals. The quantity of interest, the distribution of the Joulean heat flux or EM power density at the silicon surfaces, can be scaled later in the heat transfer model.
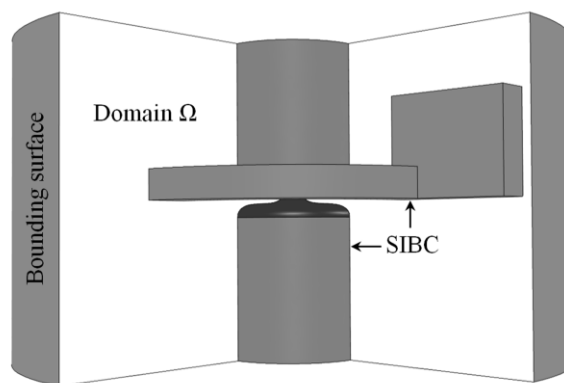

Figure 2-2   Domain (One quarter of the domain is removed to uncover inner boundaries)

2.3   Shape of the Free Melt Surface

The shape of the free melt surface during FZ growth is governed by the capillary pressure, the hydrostatic pressure and the EM pressure. The equilibrium of gravitational and surface tension forces can be expressed by the Laplace-Young equation in the form:

$$\Delta p - \rho_l g z = \gamma K,$$

Δp	pressure difference	ρ_l	density of liquid
z	vertical coordinate	g	gravitational constant
γ	surface tension	K	curvature

(2.9)

where Δp is the pressure difference to the surrounding gas. The shape of the free melt surface during the growth of a cylindrical crystal is almost axisymmetric (see Figure 2-3) and mainly governed by the capillary pressure and the hydrostatic pressure.

In the simulation procedure the interface shape is determined for fixed positions of the triple points. It is assumed that the position of the triple points and the shape of the free melt surface are not coupled to the temperature field, e.g. due to the temperature dependence of the surface tension. The influence of the melt flow and crystal rotation is omitted.

At first the axisymmetric problem, in which the EM pressure is neglected, is solved by the numerical solution of the Laplace-Young eq. (2.9). The axisymmetric Laplace-Young equation can be rewritten as a system of differential equations [41]:

$$\frac{dR}{ds} = \sin\beta, \qquad \frac{dZ}{ds} = \cos\beta(s), \qquad \frac{d\beta}{ds} = \frac{\cos\beta}{R} + \frac{\rho g R_c^2}{\gamma} Z - \underbrace{\frac{\Delta p R_C}{\gamma}}_{p_0}.$$

$R(s), Z(s)$ dimensionless coordinates $\beta(s)$ local angle
        s dimensionless arc length R_c crystal radius

(2.10)

where p_0 is an unknown gauge pressure. This system of differential equations is solved as an initial value problem with the Runge-Kutta method for the dimensionless arc length.
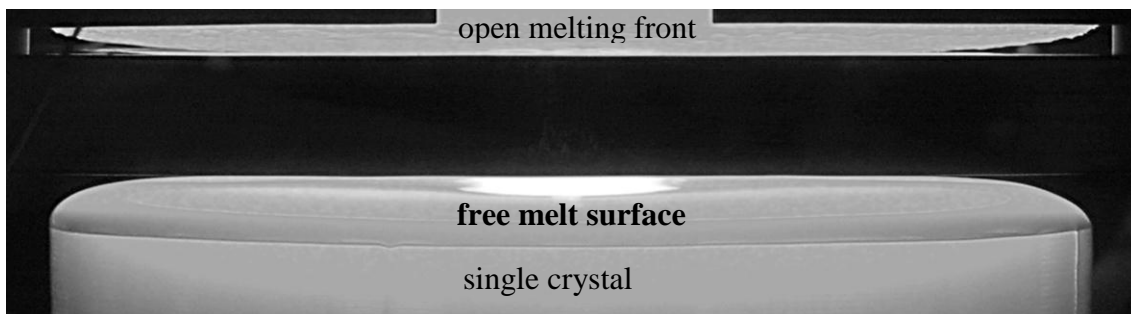

Figure 2-3   Free melt surface during FZ growth.

To solve eq. (2.10) a start angle β_0 at the initial position $(Z,R)=(0,1)$ is required. The angle β_0 at the ETP is a constant as, in a stationary process, the contact angle between solid and liquid depends entirely on the material parameters of silicon. As experimentally validated by Wuenscher [42], this value is set to $\beta_0=11°$. The gauge pressure p_0 is adjusted to obtain a physical solution, in which the curve of s is on a given position of the ITP. The R coordinate of the ITP corresponds to the radius of the melt neck, which is approximately known from measurements. It is assumed that the curve of s is vertical at the ITP, which gives the termination condition in the calculation.

Hence, the distance between ETP and ITP, the zone height, is a result of the calculation. The dimensionless coordinates R,Z are obtained and scaled with the crystal radius R_C to obtain the shape of the free melt surface. The result of an axisymmetric calculation of the shape of the free melt surface for a crystal diameter of 4 inches is shown in Figure 2-4.

Furthermore, the position of the free melt surface relative to the inductor is needed. A beneficial characteristic of the FZ process is the good visibility of the lower part of the molten zone. During the growth the position of the ETP relative to the inductor is measured and the generator power is adjusted, by the operator or control system, to meet a certain distance between inductor and the ETP. The zone height between ETP and ITP is usually hard to measure as the ITP is hidden by the inductor. As the position of the ETP in the laboratory coordinate system is kept constant, the position of the ETP can be taken as an input parameter for the stationary simulation, and determines the distance of the calculated surface shape to the inductor in the model.
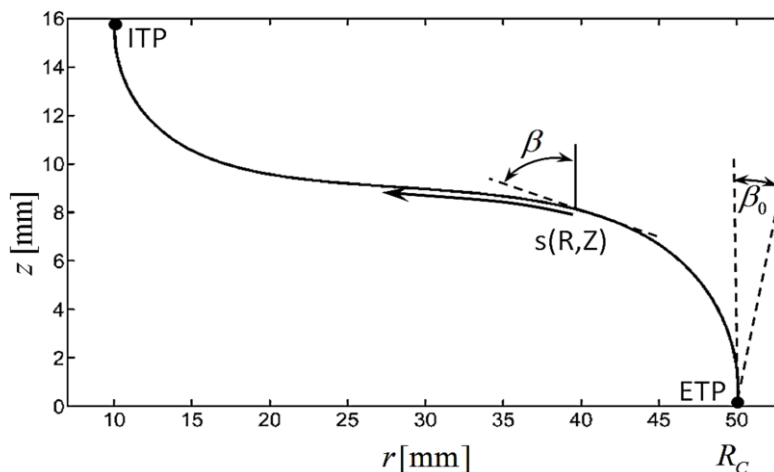

Figure 2-4   Axisymmetric shape of the free melt surface if surface tension and gravitation is considered. (4 inch diameter crystal)

If the EM pressure is considered, the balance between hydrostatic, capillary and EM pressure at the free melt surface can be written as:

$$\Delta p - \rho_l g z + p^{EM} = \gamma K.$$

$$p^{EM} \quad \text{EM pressure}$$

(2.11)

The EM pressure at the surface can be related to the EM power density q^{EM} (see 5.3):

$$p^{EM} = q^{EM} \sigma \delta \mu_0 / 2$$

(2.12)

The EM pressure pushes the melt in opposite direction to the inductor. Generally, the inductor generates a non-axisymmetric EM field and, hence, the EM pressure distribution is not axisymmetric. The EM pressure can be considered in a 2.5D simulation assuming symmetry of the EM field, as done e.g. in [43], [44]. In [45] the 3D shape of the molten zone during FZ growth is numerically studied in microgravity. In [46] Rudevičs presents a full 3D approach to consider the EM pressure in a FZ model.

As will be shown later, the EM pressure plays a role in the use of lower operating frequencies and is qualitatively considered in the applied FZ model. The axisymmetric solution of the Laplace-Young equation is used for creating the mesh for the 3D EM model. The 3D boundary mesh of the free melt surface is shown in Figure 2-5. Details of the full 3D mesh can be found in the appendix (Figure 7-1 and Figure 7-2).
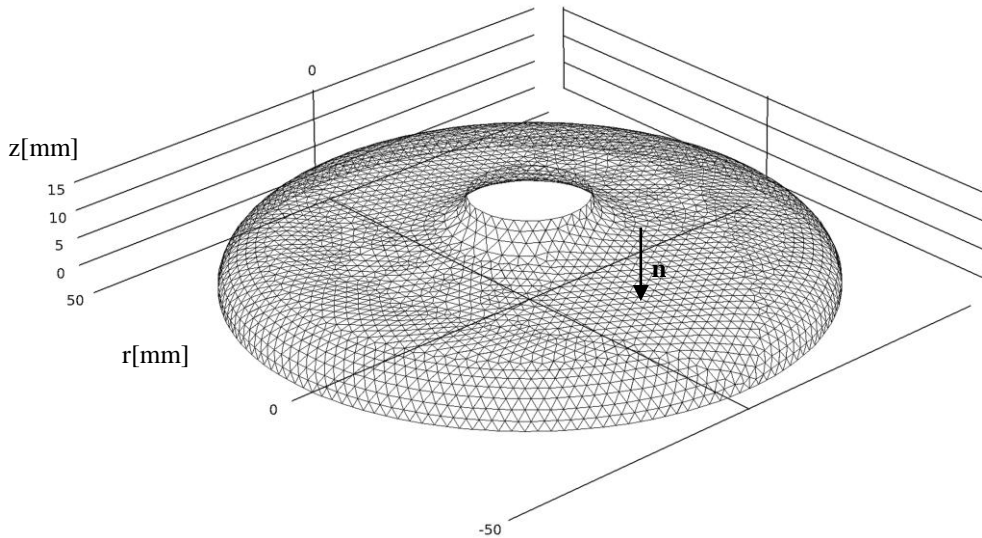

Figure 2-5   Boundary mesh of the free melt surface in the 3D model (5800 triangles).

At the vertices of the boundary mesh of the free melt surface the local imbalance D between the EM pressure and the hydrostatic pressure is evaluated:

$$D = p^{EM} - \rho_l g \Delta z.$$

(2.13)

The mesh is deformed in direction of the surface normal n by the displacement of the vertices to obtain a minimum imbalance between the pressures. The term for the surface curvature in eq. (2.11) is held constant. The impact of the EM pressure on the shape of the molten zone is comparably small. It is assumed that the contribution from the change of the curvature K is negligible and this approximation allows studying the principal impact of the EM pressure. The melt is pushed away from the inductor, according to the local magnitude of the EM pressure. Generally, a change of the z coordinates of the free surface due to the shifting of the mesh nodes results in a change of the melt volume. In a first approximation the melt volume is not preserved during the calculation. As the distribution of the EM field and, hence, the EM pressure depends on the shape of the boundary, the eq. (2.13) has to be evaluated in conjunction with the EM field simulation. The imbalance is minimized for several calculations of the EM pressure on the deformed mesh, until the change of the boundary displacement is effectual small. The EM model provides only the relative distribution of the EM quantities and not the absolute values. The absolute values can be deduced from the heat transfer model described in the next section. The heat transfer model provides absolute values of the temperature and the Joule heat and allows scaling of the dimensionless EM quantities. At first, an initial solution of the EM field is obtained using the axisymmetric shape of the free melt surface calculated with the Laplace-Young eq. (2.9). In the subsequent iteration step the absolute EM pressure can be considered with eq. (2.13). Considering the EM pressure and deformation of the free melt surface leads to a new distribution of Joule heat and requires an update of the heat transfer model. As the impact of the EM pressure on the global temperature field is small, the coupling is weak and only a few cycles in the loop depicted in figure 2-6 are necessary for a converged solution.
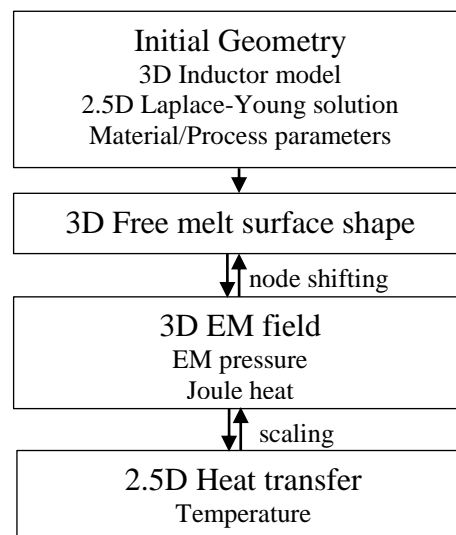

Figure 2-6   Coupling of models: In the first step the dimensionless Joule heat distribution is calculated. The heat transfer model allows scaling of the EM quantities. In the subsequent iterations deformation of the free melt surface due to the EM pressure is considered.

2.4   Heat Transfer

The heat transfer model allows studying the impact of a specific inductor shape, a reflector or an additional radiation heater on the temperature field and the shape of the crystallization interface. The latter is interesting as the crystallization interface deflection can be measured and, hence, a method to validate the heat transfer model as well as the EM model is provided. Furthermore, knowing the temperature field in the crystal is the basis for the thermal stress analysis.

For the global temperature calculation axial symmetry of the FZ system is assumed. An axisymmetric heat transfer model is applied. The temperature fluctuations due to the non-axisymmetric EM power distribution, as a result of the slits in the inductor, are not considered. The impact of the inhomogeneity of the EM field is discussed in chapter 3 by means of the 3D Joulean heat distribution. In the heat transfer model it is assumed that the EM power is azimuthally averaged as the crystal is rotated. It is obvious that this approximation gains accuracy with increasing crystal rotation rate.

The model is quasi-stationary, assuming constant pull velocities of the crystal and the feed rod. The impact of the melt convection on the shape of the crystallization interface and the temperature distribution in the crystal is neglected[1]. The assumption that the impact of the melt flow on the shape of the crystallization interface is small is well justified for the FZ process. The model applied involves calculation of the following phenomena:

- temperature field in the molten zone, single crystal and feed rod
- shape of the crystallization interface and the melting interface
- emission and reflection of heat from the surfaces due to diffuse radiation
- convective cooling due to the gas atmosphere in the growth chamber

To calculate the temperature in the crystal, melt and feed rod domain, a stationary heat transfer equation is solved in the form:

$$c_p \rho v_{C,F} \cdot \nabla T = \nabla \cdot \left(\lambda(T) \nabla T \right)$$

T	temperature	
λ	thermal conductivity	(2.14)
c_p	heat capacity at constant pressure	
ρ	density	
$v_{C,F}$	pull speed of crystal/feed	

---

[1]   In silicon heat conduction is more effective than heat convection. This is reflected in the low value of the Prandtl number of liquid silicon (Pr=0.013).

It is expressed that heat is transported in the material by two mechanisms: via heat conduction and by the downward movement of the crystal and the feed rod, with a rate of v_C and v_F respectively. The law of mass conservation yields the following relation between these velocities:

$$v_F = \frac{R_C^2}{R_F^2} v_C,$$

(2.15)

where R_C and R_F are the radii of crystal and feed rod. In the molten zone only heat conduction is considered.

To model heat exchange between radiating and reflecting surfaces the view factor method is applied. This method is widely used to describe radiative heat transfer between surfaces arbitrarily arranged in space. The materials involved in the FZ process are considered as grey bodies with a surface emissivity of ε, which is assumed as being temperature dependent in the case of solid silicon. The gas atmosphere of mainly argon is assumed to be transparent for radiation, and only diffuse surface to surface radiation is considered.

The total heat flux leaving a point of the radiating surfaces is

$$q^{rad} = \varepsilon \sigma_{SB} T^4 + (1-\varepsilon) G$$

$$\begin{array}{ll} \varepsilon & \text{emissivity} \\ G & \text{incident radition} \\ \sigma_{SB} & \text{Stefan-Boltzmann constant} \end{array}$$

(2.16)

The first term in eq. (2.16), the Stefan-Boltzmann law for grey bodies, is large at the hot silicon surfaces of higher emissivity. For the reflecting surfaces of low temperature and low emissivity, e.g. the surface of the water cooled copper inductor, the contribution from the second term in eq. (2.16) is significantly larger than the latter. The irradiation G is the sum of:

$$G = G_M + F_A \sigma_{SB} T_A$$

$$\begin{array}{ll} G_M & \text{mutual irradiation} \\ F_A & \text{ambient view factor} \\ T_A & \text{ambient temperature} \end{array}$$

(2.17)

where G_M is the mutual irradiation arriving from other surfaces and F_A is the ambient view factor. The ambient view factor describes the portion of view that is not covered by any boundaries. This applies for the upper and lower growth chamber walls, which were not modeled. For details on how the mutual irradiation G_M and the ambient view factor F_A can be obtained from a geometry see e.g [47]. In [48], [49] Guo et al. show the impact of considering specular reflecting surfaces in the FZ system.

Since the crystal in the FZ system is surrounded by a gas atmosphere of mainly argon, there is an additional heat transfer to the gas. The heat transfer to the gas atmosphere is modeled as:

$$q^{con} = \kappa \left(T - T_G \right).$$

κ heat transfer coefficient
T_G ambient gas temperature

(2.18)

The determination of the heat transfer coefficient and the temperature of the gas atmosphere have been subject to experimental investigation and is explained later (see section 4.5).

Interface Calculation

Molecular considerations indicate that the melt-solid interface during crystal growth is not sharp and that there is an ordering of atoms near the interface. For the purpose of calculating the global temperature distribution it is adequate to assume that there is a sharp transition between solid and liquid.

A moving boundary approach is used to simulate the crystallization interface. In this method the mesh deforms to align the element boundaries with the melting point isotherm. In the model the crystallization interface is represented by the mesh boundary $\Gamma_{C\text{-}M}$ (see Figure 2-7). During calculation the mesh is deformed to ensure the boundary is at the melting temperature of silicon. The calculation is performed for fixed positions of the triple points and fixed shape of the free melt surface. The procedure can be described as follows. In an initial configuration the boundary $\Gamma_{C\text{-}M}$ is given as a horizontal line (flat interface). The heat transfer equation is solved for this configuration. To ensure the boundaries of the mesh are at melting temperature, the imbalance between melting temperature and the local temperature at each node of the boundary is minimized:

$$D = T(r) - T_{MP} \qquad\qquad \text{at } \Gamma_{C-M}$$

T_{MP} melting temperature

(2.19)

In the subsequent iterations the nodes of the boundary are displaced in vertical direction, to minimize the imbalance D. The iterations are repeated until the imbalance is below a given criterion. The same algorithm is applied to determine the shape of the melting interface $\Gamma_{F\text{-}M.}$ A precise calculation of the shape of the melting interface requires a dynamic calculation of the position of the ITP, which involves determining the shape of the open melting front (see e.g. [50]). In the current model the ITP and the open melting front are spatially fixed. However, the focus of the numerical studies is on the temperature field in the crystal, which is assumed to be only marginally influenced by this inaccuracy.
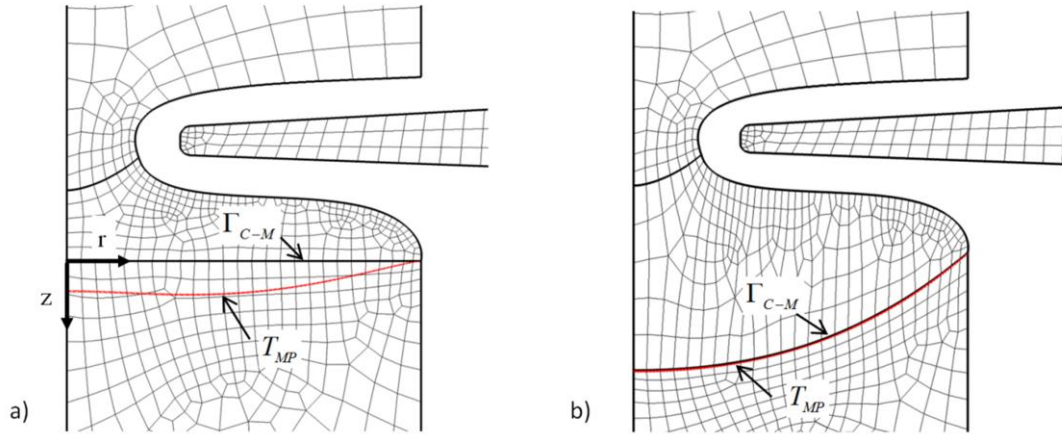
Figure 2-7   Calculation of the crystallization interface shape. The red line is the calculated
                     melting temperature isotherm in the initial a) and the deformed configuration b).
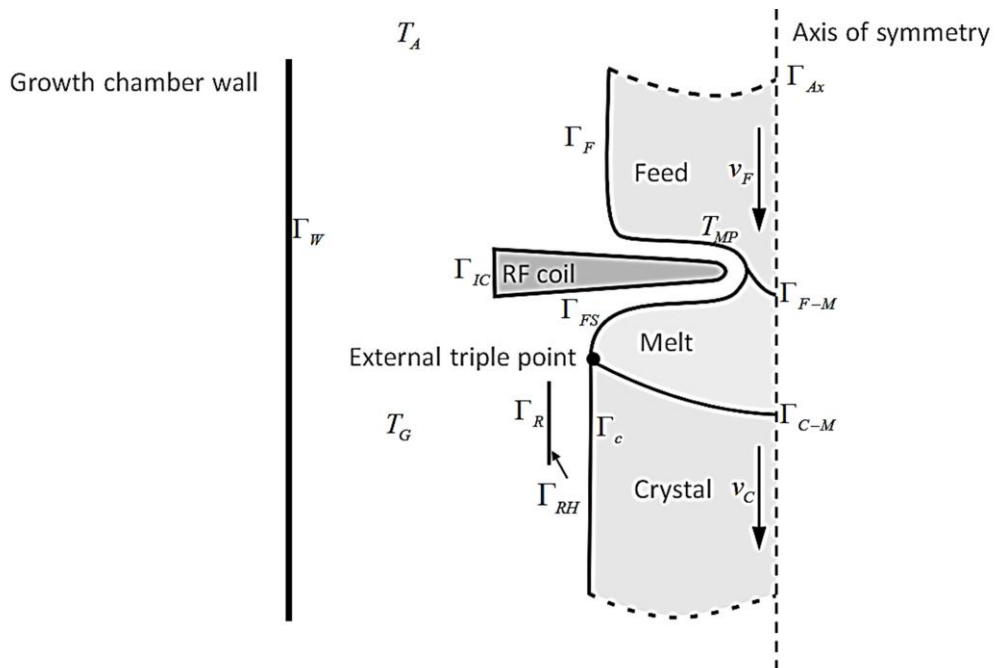   A full view of the mesh is given in the appendix (see Figure 7-3).

Figure 2-8   Boundary conditions in the heat transfer model for the FZ process

Boundary Conditions

The boundary conditions in the heat transfer model are summarized in Figure 2-8. The time averaged EM power density is considered as a boundary heat source. The EM power density calculated in 3D space is azimuthally averaged and interpolated from the 3D surface on the boundary Γ_{FS} of the 2D mesh in the heat transfer model.

The EM model provides only the dimensionless distribution of the dissipated EM power density. The absolute value of the power density can be calculated in the heat transfer model. The magnitude of the boundary heat source is given due to the fact that the temperature at the ETP must reach melting temperature. This can be expressed via an additional constraint in the temperature calculation. The dimensionless EM power density, from which only the spatial distribution is known, is scaled until the melting temperature is reached at the ETP in the calculation. This type of problem is also referred to as a backward problem.

Considering the induced EM power and heat transfer by radiation and convection to the surroundings, the heat balance at the free melt surface can be written as:

$$\lambda_l \nabla T\big|_l \cdot \mathbf{n} = q^{rad} + q^{con} - q_{az}^{EM} \qquad \text{at } \Gamma_{FS}.$$

$$
\begin{array}{ll}
\lambda_l & \text{heat conductivity of the liquid (l)} \\
T & \text{temperature} \\
\mathbf{n} & \text{surface normal} \\
q^{rad} & \text{radiative heat flux} \\
q^{con} & \text{convective heat flux} \\
q_{az}^{EM} & \text{azimuthal average of the EM power density}
\end{array}
$$

(2.20)

Heat dissipation due to radiation and convective cooling at the solid silicon surfaces of the feed rod and the single crystal is considered with:

$$\lambda_s \nabla T\big|_s \cdot \mathbf{n} = q^{rad} + q^{con} \qquad \text{at } \Gamma_F, \Gamma_C.$$

$$\lambda_s \qquad \text{heat conductivity of the solid (s)}$$

(2.21)

The boundary conditions at the crystallization interface and the melting interface have to account for the release or consumption of the latent heat Δh. The continuity of the heat flux at the solid liquid interfaces is expressed by the Stefan condition. The production of latent heat at the crystallization interface and consumption of latent heat at the melting interface is taken into account.

The Stefan condition at the crystallization interface reads:

$$\left(-\lambda_l \nabla T\big|_l + \lambda_s \nabla T\big|_s\right)\cdot \mathbf{n} = \rho_s\,\Delta h\,\mathbf{n}\cdot \mathbf{v}_C \qquad\qquad \text{at } \Gamma_{C-M}.$$

$\quad\Delta h \qquad$ latent heat of fusion   (2.22)

$\quad\rho_s \qquad$ density of the solid

Similarly, the Stefan condition at the upper melting interface can be written as:

$$\left(-\lambda_l \nabla T\big|_l + \lambda_s \nabla T\big|_s\right)\cdot \mathbf{n} = \rho_s\Delta h\,\mathbf{n}\cdot \mathbf{v}_F \qquad\qquad \text{at } \Gamma_{F-M}. \qquad (2.23)$$

The heat fluxes near the interface in the melt and the solid silicon are equal except for the latent heat.

At the open melting front the temperature is fixed to the melting temperature of silicon:

$$T = T_{MP} \qquad \text{at } \Gamma_{OMF}. \qquad\qquad (2.24)$$

The water cooled walls of inductor, growth chamber and the reflector are set to constant temperature:

$$T = 300K \qquad \text{at } \Gamma_W, \Gamma_{IC}, \Gamma_R. \qquad\qquad (2.25)$$

In cases where the impact of a radiation heater below the inductor is studied, the radiative heat flux q^{rad} is explicitly defined at the boundary $\Gamma_{RH.}$

In the axisymmetric model the normal gradient of the temperature is zero at the axis of symmetry:

$$\nabla T \cdot \mathbf{n} = 0 \qquad \text{at } \Gamma_{ax}. \qquad\qquad (2.26)$$

2.5   Thermal Stress

For the calculation of thermal stress in the growing single crystal, axial symmetry of the FZ system is assumed. The theory of linear elastic deformation is applied. It is applicable for small and slow deformations in materials, for which a linear relationship between the components of stress and strain can be presumed and the deformation is reversible. For the given problem a dislocation-free Si crystal is considered and, hence, no plastic deformation or yield is taken into account. The impact of the weight of the molten zone above the crystal and the stress due to its own mass exposed to gravitational forces is not taken into account.

Due to a thermal load, the material at each point in the crystal is reversibly displaced along a displacement vector **u**. In the case of small displacements, the state of strain can be expressed by the symmetric strain tensor:

$$\epsilon = \frac{1}{2}\left(\nabla\mathbf{u} + \nabla\mathbf{u}^{\mathrm{T}}\right).$$

(2.27)

ϵ strain tensor

The strain tensor describes the local change of distance between two points in the volume and is a function of the gradients of the displacements. Only a non-homogenous displacement field leads to a new shape of the body and causes strain.

In the case of a thermal load, the deformation of the body caused by mechanical stress is superimposed by the deformation due to stresses caused by temperature differences [51]. The linear relationship between stress and strain in a body with temperature differences is represented by Hooke's law with thermal deformation:

$$\boldsymbol{\sigma} = \mathbf{C}\left[\epsilon - \alpha\left(\mathrm{T} - \mathrm{T}_0\right)\boldsymbol{\delta}\right].$$

(2.28)

$\boldsymbol{\sigma}$ stress tensor $\mathbf{C}$ elastic stiffness tensor
T_0 reference temperature $\boldsymbol{\delta}$ Kronecker tensor
α coefficients of thermal expansion

A detailed derivation of the latter equations can be found in the standard works for thermal stress analysis, e.g. in [51]. The 9 components of the stress tensor:

$$\boldsymbol{\sigma} = \begin{pmatrix} \sigma_{11} & \sigma_{12} & \sigma_{13} \\ \sigma_{21} & \sigma_{22} & \sigma_{23} \\ \sigma_{31} & \sigma_{32} & \sigma_{33} \end{pmatrix}$$

(2.29)

can be interpreted in terms of the components of a force, acting in normal or tangential directions on the surfaces of an infinitesimally small cubic volume element (see Figure 2-9).
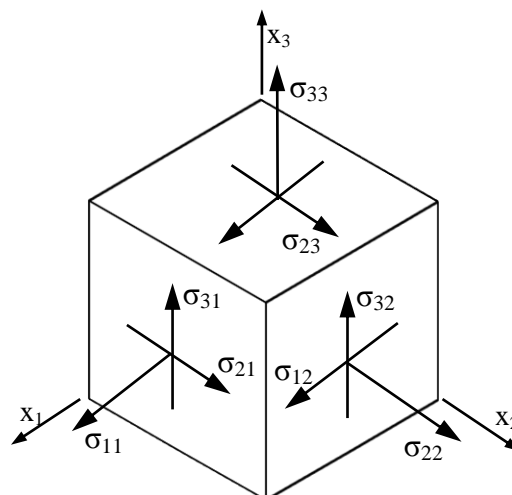

Figure 2-9   Interpretation of the 9 components of the stress tensor in Cartesian coordinates.

The normal stresses (the diagonal elements) act in direction of the surface normal, whereas the shear stresses act in tangential direction. It can be shown that only 6 of the 9 components in the stress tensor are independent [52]. Hence, a three-dimensional state of stress is determined by 6 independent stresses.

In a body under a load, a stress field will evolve in such way that the forces are in equilibrium in every point in the body. As no external forces are considered, from the equilibrium of forces it follows that:

$$\nabla \cdot \boldsymbol{\sigma} = 0. \tag{2.30}$$

The partial differential equations solved can be derived by expressing the strains in terms of the displacements (eq.(2.27)) and combining Hooke's law eq. (2.28) with the equilibrium of forces:

$$\nabla \cdot \left[\frac{1}{2}\mathbf{C}\nabla\mathbf{u} + \frac{1}{2}\mathbf{C}\nabla\mathbf{u}^{\mathrm{T}} - \alpha\left(\mathrm{T} - \mathrm{T}_0\right)\mathbf{C}\boldsymbol{\delta} \right] = 0. \tag{2.31}$$

The temperature field required in eq. (2.31) is known from the heat transfer model. The elastic stiffness tensor is a material parameter. It can be shown that in case of complete anisotropy of the material, the stiffness matrix has only 21 independent components, which applies only for the triclinic crystal system [53]. As a result of symmetry, the number of independent components in the stiffness tensor is smaller in all other crystal systems The stiffness tensor for different crystal systems and their derivation from symmetry considerations is given in the book of Nye [53].

Silicon crystallizes in a cubic structure. In the cubic crystal system the number of independent components in the stiffness matrix reduces to 3. The Voigt notation allows reducing the order of the stiffness matrix and writing it more compact as a 6x6 matrix (see [54] for details). The form of the matrix depends on the choice of the coordinate system. If the crystallographic axes are used as coordinate axes, the elastic stiffness matrix for a cubic crystal can be written as [55] :

$$\hat{\mathbf{C}} = \begin{pmatrix} c_{11} & c_{12} & c_{12} & 0 & 0 & 0 \\ c_{12} & c_{11} & c_{12} & 0 & 0 & 0 \\ c_{12} & c_{12} & c_{11} & 0 & 0 & 0 \\ 0 & 0 & 0 & c_{44} & 0 & 0 \\ 0 & 0 & 0 & 0 & c_{44} & 0 \\ 0 & 0 & 0 & 0 & 0 & c_{44} \end{pmatrix}. \tag{2.32}$$

The elastic properties of a cubic crystal like silicon are non-isotropic. The stiffness matrix and the stress field in a silicon crystal grown in the [100] direction are different from that grown in the [111] direction. Furthermore, the stress field in the silicon crystal is not of axial symmetry, even if an axisymmetric temperature field is assumed. However, computations considering the anisotropy of the crystal are very time-consuming and the differences to the

results of calculations assuming isotropic mechanical properties are small. The influence of the anisotropy in cubic crystals on the calculation of stresses was investigated by Miyazaki et al. [56], [57].

In this work silicon is treated as an isotropic material. In the isotropic case, the number of independent coefficients in the stiffness tensor reduces to 2 and the stiffness matrix can be written as:

$$\hat{\mathbf{C}} = \begin{pmatrix} c_{11} & c_{12} & c_{12} & 0 & 0 & 0 \\ c_{12} & c_{11} & c_{12} & 0 & 0 & 0 \\ c_{12} & c_{12} & c_{11} & 0 & 0 & 0 \\ 0 & 0 & 0 & \frac{1}{2}(c_{11}-c_{12}) & 0 & 0 \\ 0 & 0 & 0 & 0 & \frac{1}{2}(c_{11}-c_{12}) & 0 \\ 0 & 0 & 0 & 0 & 0 & \frac{1}{2}(c_{11}-c_{12}) \end{pmatrix}. \tag{2.33}$$

The elastic constants in isotropic media are commonly referred to as Young's modulus E and Poisson's ratio ν. The relationship between the latter and the coefficients in the stiffness tensor for isotropic media are:

$$c_{11} = \frac{(1-\nu)E}{(1+\nu)(1-2\nu)}, \qquad c_{12} = \frac{\nu E}{(1+\nu)(1-2\nu)}. \tag{2.34}$$

To obtain the thermal stress field in the growing crystal, the differential equations (2.31) are solved in COMSOL, using the material parameters given in 2.7 and with boundary conditions described in the following.

Boundary Conditions

In the process the growing crystal is spatially fixed at the seed holder. Therefore, the displacements are set to zero at the corresponding lowermost point at the crystal in the model:

$$\mathbf{u} = 0 \tag{2.35}$$

For the computation of the thermal stress in the crystal domain the precise shape of its boundaries is required. The shape of the crystallization interface is obtained in the thermal model, whereas the shape of the crystal cone is derived from measurements at grown crystals.

2.6   Validation

To verify the applicability of the chosen method and the boundary conditions set in the models, comparison to experimental data is essential. The access to measurable physical quantities is limited. In the following, results obtained in the numerical models are compared to measurements of the EM fields and the shape of crystallization interface.

Due to the harsh conditions in the growth chamber during an experiment, the measurement of the distribution of the EM fields in an experiment is practically impossible. Therefore, the EM field generated by a HF inductor used for the 4" IKZ process was measured outside the growth chamber in a measuring station.

The setup used is shown in Figure 2-10a. A small probe coil was placed in the EM field generated by the HF inductor. A HF generator with an operating frequency of 3MHz was used. The axes of inductor and probe coil below the inductor are in parallel. The measured induced voltage in the probe coil is proportional to the magnitude of the vertical component of the magnetic field, generated by the inductor. An x-y scan in a plane below the inductor allows measuring a map of the magnetic field. The vertical component of the magnetic field is calculated with the method described in section 2.2, in the corresponding x-y plane in the model. The results of measurement and calculation are shown in Figure 2-10b.
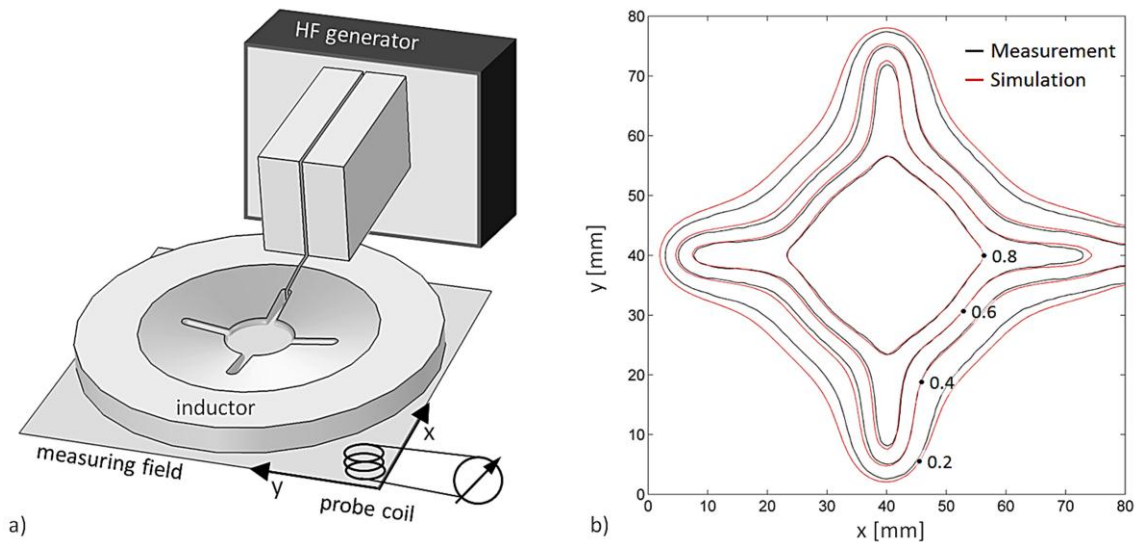
Figure 2-10   Validation of the EM field calculation. a) Setup for measuring the magnetic field in a plane below the inductor. b) Contour lines of the normalized magnitude of the axial (z) component of the measured and the calculated magnetic field.

Several contour lines of the magnitude of the vertical component of the magnetic field, which is normalized to its peak value in the center of the plane, are evaluated. The vertical component of the magnetic field is strongly decreasing in the vicinity of the edges of the hole and the side slits. It can be seen that the result of measurement and simulation are in good agreement. Although the measurement setup does not exactly reflect the situation in the growth chamber, as there is no load in form of the molten zone, it can be concluded that the method and boundary conditions applied are appropriate to describe the 3D EM field in the FZ process.

The lateral photovoltage scanning (LPS) method provides the possibility to measure the shape of the crystallization interface and is therefore a convenient method to validate the calculation of the temperatures in the growing crystal. In the LPS method a laser light beam focused on a flat silicon sample cut from the grown crystal generates free electron/hole pairs. The resistivity gradients, which arise due to the fluctuating incorporation of dopants during the growth, lead to a surface potential difference at the position of the light spot. Therefore, at the rim contacts of the sample a voltage can be measured. The magnitude of this voltage is proportional to the lateral resistivity gradient. From a scan of a longitudinal cut of the crystal, the shape of the crystallization interface, as it was during the growth, can be extracted. The LPS method was developed at the IKZ Berlin and is described in detail in [58].

The detected and the calculated crystallization interface shapes during a 4 inch growth process are compared in Figure 2-11. The deflection is measured across the diameter of the crystal. The point of reference is the position of the ETP, where the deflection is zero. It can be seen that the interface shape calculated with the method described in section 2.4 is in good agreement with the measured shape. Nevertheless, the calculated maximum deflection is 16.8mm, whereas the measured is only 15.5 mm. The small discrepancy between measurement and simulation can be explained by the fact, that heat transport due to convection in the molten zone is not considered in the heat transfer model.
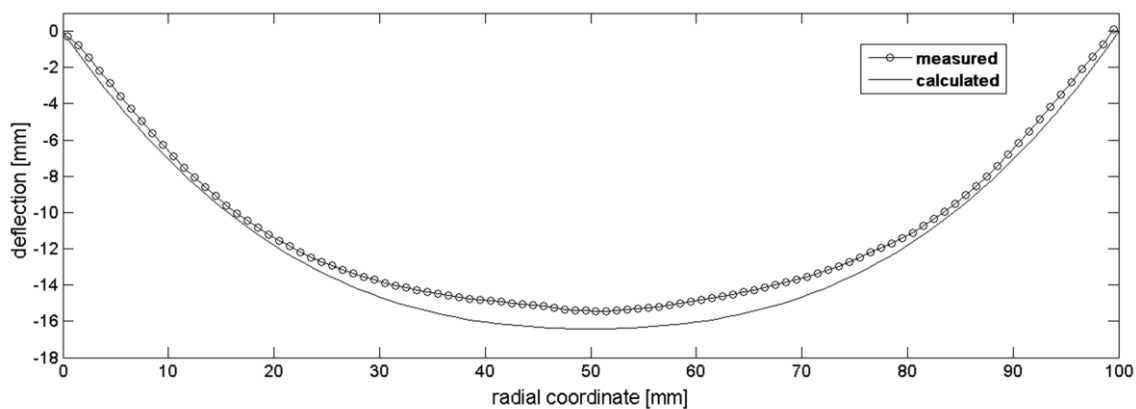

Figure 2-11   Measured and calculated shapes of the crystallization interface.
                     (4 inch process, crystal pull speed: v_C =3.2mm/min; no reflector)

2.7   Material Properties

The physical properties of silicon used in the simulations are summarized in Table 2-2.

Table 2-2 Physical properties of silicon*

Quantity		Value	Unit
Electrical Properties			
electrical conductivity (liquid)	σ_l	$1.26 \cdot 10^6$	$1/(\Omega m)$
electrical conductivity (solid)	σ_s	$5 \cdot 10^4$	$1/(\Omega m)$
Thermal Properties			
melting temperature	T_{MP}	1687	K
density (solid)	ρ_s	2330	kg/m^3
density (liquid)	ρ_l	2530	kg/m^3
specific heat capacity	c_p	1000	$J/(kg \cdot K)$
latent heat	h	$1.8 \cdot 10^6$	J/kg
thermal conductivity (liquid)	λ_l	67	$W/(mK)$
thermal conductivity (solid)	λ_s	$98.9 - 0.0943 \cdot T + 2.89 \cdot 10^{-5} \cdot T^2$	$W/(mK)$
emissivity (liquid)	ε_l	0.27	-
emissivity (solid) T<1000K	ε_s	0.64	-
emissivity (solid) T>1000K	ε_s	$0.9 - 2.6 \cdot 10^{-4} \cdot T$	-
Mechanical Properties		.	
Young's modulus	E	$1.56 \cdot 10^{11}$	N/m^2
Poissons ratio	ν	0.25	-
coeff. of thermal expansion	α	$3.2 \cdot 10^{-6}$	$1/K$

*Electrical and thermal properties are taken from [22]. Mechanical properties from [59].

3. Inductor and Joulean Heat Distribution

3.1 The HF Inductor

The shape of the HF inductor plays a decisive role in the development of a crystal growth process. The temperature field in the hot zone is to a large extent determined by the distribution of the induced Joulean heat or EM power. As the Joulean heat distribution can be controlled by the shape of the inductor, its modification allows influencing the temperature field on a comparatively large scale. Changes in the inductor geometry, as small as 1mm, can have a significant impact on the Joulean heat distribution and the temperature field. The inductor must ensure a proper, homogeneous melting of the feed rod and maintain stability of the molten zone at the same time. The 3D EM field during FZ growth was already studied e.g. by Mühlbauer et al. [29] and Ratnieks et al. [29]

The Figure 3-1 shows a sketch of a pancake inductor with lateral slits as it is commonly used in growth processes for crystals with large diameter, and also in the experiments described later. It is water cooled and sharp corners are avoided as this may lead to current crowding at the edges and cause local melting of the inductor. The material widely used is copper but also the use of silver with higher reflectivity and electrical conductivity is possible. The inductor surfaces are polished to achieve the best possible reflection of radiation from the molten zone and increase efficiency.
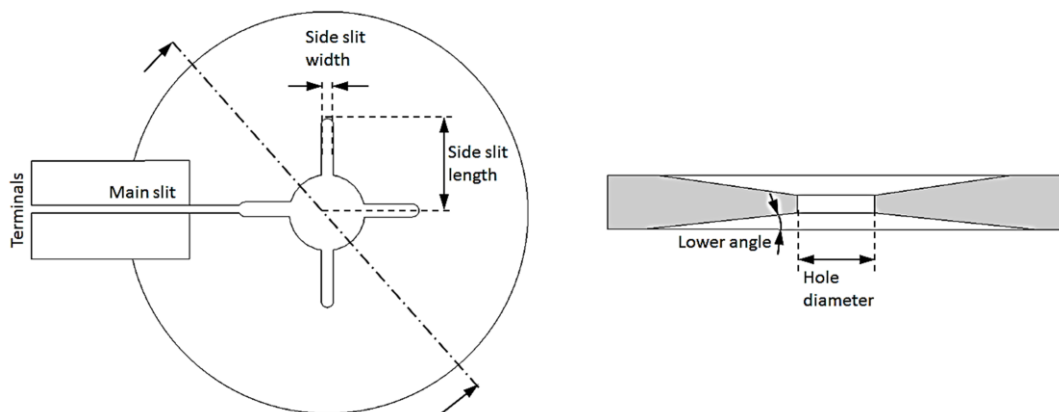
Figure 3-1   Sketch of a pancake HF inductor for the FZ process. (Top view and cross section).
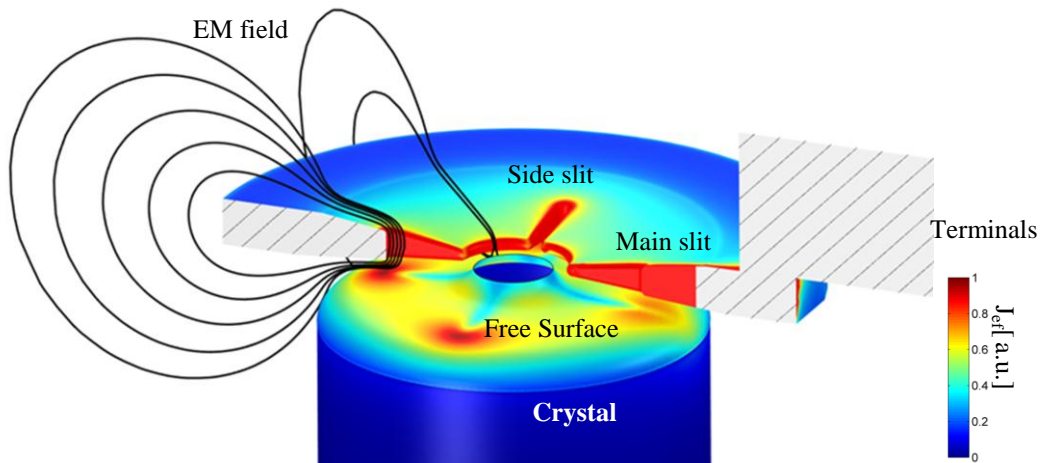
Figure 3-2   Overview of the 3D distribution of the normalized surface current density at the free melt surface and the inductor. The direction of the magnetic field is visualized by several field lines (the feed rod and one half of the inductor are not shown).

The most important features of this inductor type being able to influence the temperature field are the diameter of hole, width and lengths of the side slits and the lower angle. It is obvious that such an inductor induces a non-axisymmetric eddy current distribution as a consequence of the side slits and the main slit. Due to rotation of the crystal an almost axisymmetric temperature field will evolve in the molten zone and the crystals grows in a cylindrical shape. Nevertheless, the asymmetry of the EM field in combination with crystal rotation gives rise to local temperature perturbations.

In the following it is elaborated on the relative impact of a modification of these inductor features by means of the results of parametric simulations, conducted with the 3D EM model described earlier in 2.2. Now, the focus is on the 3D characteristics, which are not taken into account in the quasi-stationary temperature calculations, in which the FZ system is assumed to be axisymmetric.

To get a first general idea of the 3D distribution of the EM field in the FZ system, the calculated surface current distribution at the inductor and the free melt surface is qualitatively shown in Figure 3-2. An inductor with additional side slits, as shown in Figure 3-1, is considered. Only one half is shown to provide view on the free melt surface. The surface current density at the inductor has high magnitude at the rim of the hole and at the end of the side slits, where the current supplied at the terminals has to get around and is displaced from the center. Consequently, also the magnetic field has high magnitude in the vicinity of the side slits where the field lines converge. The magnetic flux in the slits is proportional to the magnetic field and the area described by the slits. The maxima of the current density at the free melt surface can be found below the end of the side slits and their magnitude depends on the extents of the slits.

3.2   Influence of Inductor Slits

The intention of applying side slits is to enforce the generation of Joulean heat at outer regions of the free melt surface. The growth of smaller crystals, with a diameter of up to 4 inch, is possible without additional means like such side slits. If no side slits are applied, the dissipated EM power is relatively more concentrated in the center close to the melt neck, which is a result of the high magnitude of the current flowing at the inner edge of the inductor hole.

In the growth of crystals with larger diameter, the dissipation of EM power at the periphery of the larger free melt surface diminishes. Without additional side slits, the augmented generation of EM power in the center region of the free melt surface and the open melting front would deteriorate the process. The consequence would be a thin, unstable liquid bridge and an unfavorable melting behavior of the feed rod near the melt neck. Furthermore, the intense heat introduction near the center of the molten zone causes a strong deflection of the crystallization interface and is related to high thermal stress in the growing crystal. High thermal stress must be avoided as it is a cause for the generation of dislocations. The relation between the EM power distribution and the thermal stress in the crystal is discussed later in 4.1.

To a small extent the induced EM power can be displaced from the center by increasing the diameter of the inductor hole, but a too large diameter of the hole can make it impossible to grow the thin neck in the start phase or may result in solidification of the melt neck later in the process. The contact of the upper melting interface with the crystallization interface will break the process. Therefore, a modification of the lower angle or the side slits is more suitable to create an appropriate EM power distribution for a large molten zone.

The main issue in the design of an inductor for the growth of a larger crystal is to identify such a suitable inductor configuration. In the following, the relative impact of the mentioned inductor shape parameters is exemplarily shown by means of the results of a parametric study. In this study a 6 inch process is considered. In each plot of Figure 3-3 a-d the calculated EM power density distribution at the free melt surface is depicted for a different parameter set. The free surface is shown as seen from above in Figure 3-2. The power distribution shown in Figure 3-3a is considered as reference case. In the cases b-d the inductor has been modified. The value of the maximum of the EM power density and the dissipated EM power at a point near the periphery of
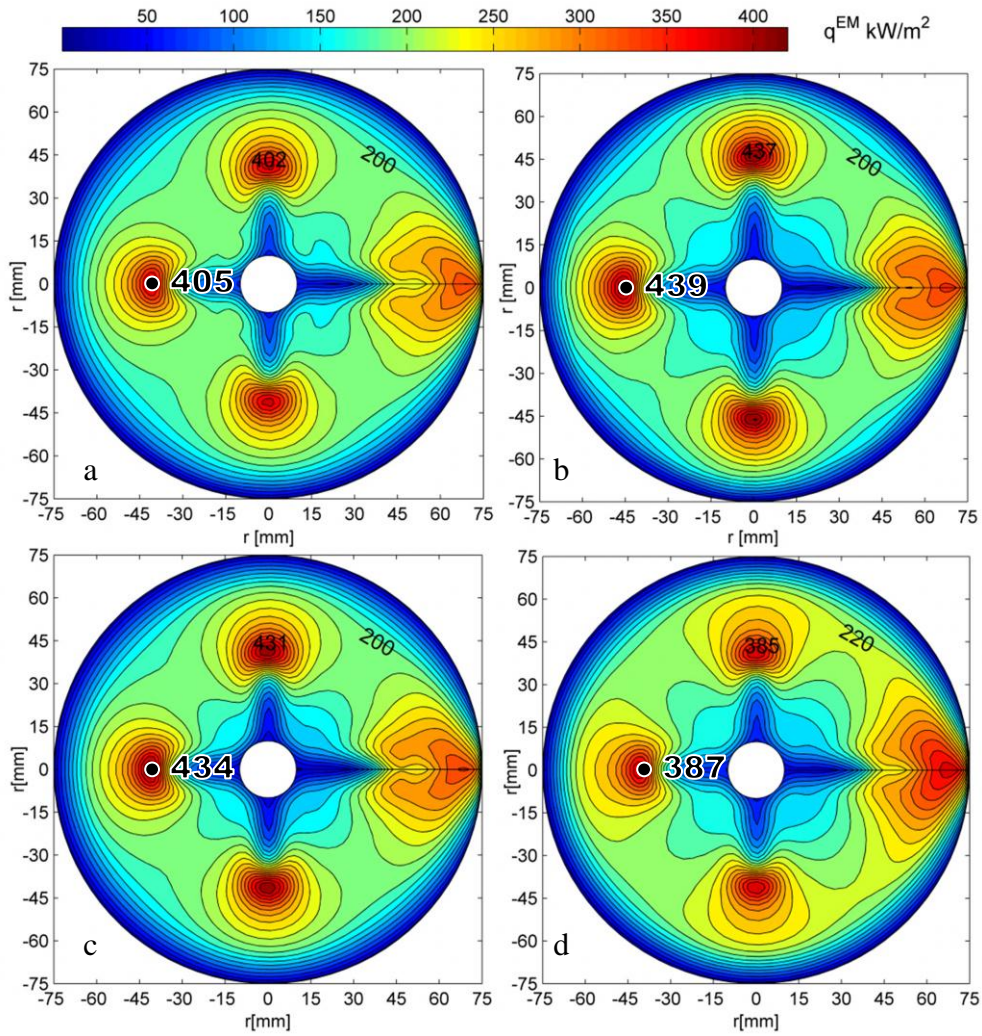
Figure 3-3   EM power density distribution at the free melt surface for different inductor shapes.

a) Reference: side slit length=40, side slit width=3 mm, lower angle =4°.

b) Side slit length is increased by 5mm

c) Side slit width is increased by 1mm

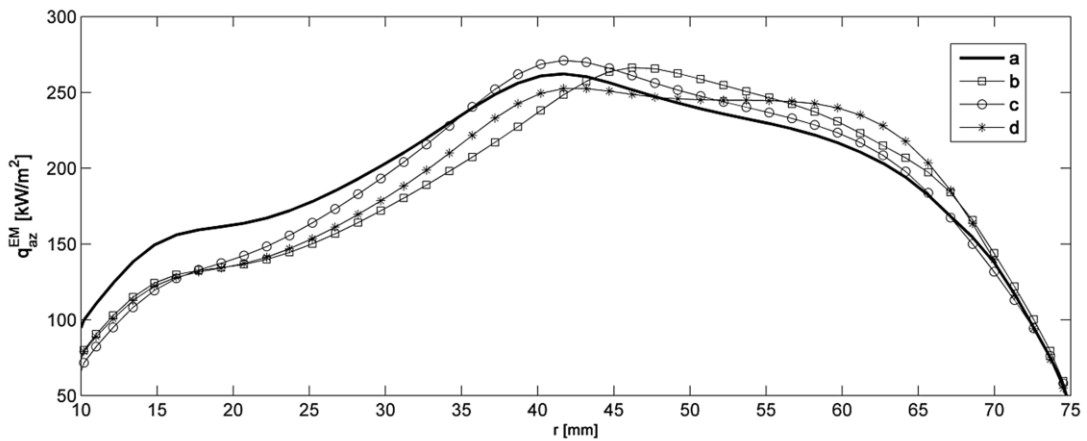d) Lower angle is increased by 1° (with respect to the horizontal)

Figure 3-4   Azimuthal average of the EM power density for the inductor configurations considered in Figure 3-3.

the free melt surface is given. The corresponding azimuthal average relevant for the global temperature distribution is shown in Figure 3-4. The results can be summarized as follows:

- The respective location of the maximum of the EM power density corresponds to the position of the end of the side slits. If the slit length is increased, the maximum moves towards the outer rim of the surface (From r=40mm in the reference in Figure 3-3a, to r=45mm in Figure 3-3b. Furthermore, the maximum of the induced EM power increases from 405kW/m^2 to 439kW/m^2. Less power is induced in the central region close to the melt neck.
- Similarly, an increase of the slit width leads to a more pronounced maximum. An increase of the slit width by 1mm causes approximately the same rise in the power maximum as an increase of the slit length by 5mm. (From 405 kW/m^2 in the reference case to 434 kW/m^2 in Figure 3-3c.
- A steeper lower angle of the inductor increases the dissipated EM power at the whole periphery of the free melt surface (see Figure 3-3d). This can be explained by the proximity effect as the relative distance of the inductor to the surface is decreasing at the rim. The heating is stronger where the inductor is closer to the melt. The power maximum decreases to 387 kW/m^2 and is less distinct, as it is "smeared" towards the rim. The maximum below the main slit is increased.

Comparing the azimuthal averages of the EM power density in Figure 3-4, it can be concluded that all these considered modifications are suitable to displace heat from the center of the molten zone. To laterally distribute the dissipated EM power, the inductor for a 6 or an 8 inch process will apparently need longer or wider side slits as an inductor for a 4 inch process.

However, it has to be taken into account that each of the modifications of the inductor shape can also have undesirable effects. In particular the rise of the maximum in the vicinity of the end of the side slits, due to an increase of their width or their length, is critical. It results in a similar distinct power maximum at the open melting front above the inductor. As has been observed in experiments, the consequence can be a local and inhomogeneous melting of the feed rod, which may hinder the smooth downward fluid flow at the open melting front. It is possible that cavities form, in which the liquid silicon accumulates and creates drop-like structures, which may come in contact with the inductor. An increase of the lower angle of the inductor raises the power level at the whole periphery of the free melt surface more homogeneously and does not affect the melting behavior. It avoids distinct local maxima at the free surface as well as at the open melting front. Unfortunately, the calculations showed that the impact of the main slit of the inductor increases if the lower angle is increased. The impact of the main slit is discussed more in detail later.

A relative increase of the EM power dissipation at the periphery of the free melt surface lowers the crystallization interface deflection and helps to reduce thermal stress. On the other hand, a less deflected crystallization interface and, hence, a lower radial temperature gradient is known to promote deviations from the desired cylindrical growth. A sharp gradient of the field is required to ensure a well-defined shape of the three-phase line. The smaller the temperature gradient near the crystal rim the larger is an impact on the shape of the three-phase line due to a local perturbation of the EM power dissipation. Therefore, length and widths of the side slits cannot arbitrarily be increased as the consequence are lower radial temperature gradients and stronger EM power perturbations. In growth experiments with very long or wide side slits in the inductor this becomes manifest in the formation of bulges or a spiral-like growth of the crystal.

An inductor configuration seemingly qualified after a stationary simulation of the cylindrical growth phase may not be suitable to create an appropriate temperature field in the start cone phase. In this regard a critical situation arises during the growth of the cone of the crystal. There is a process stage in which the crystal rim is near the end of the side slits (see Figure 3-5). In comparison to the EM power induced in the three-phase line below the non-slitted part of the inductor, a very large amount of EM power is induced in the vicinity of the three-phase line below the slit. As a result of crystal rotation this causes strong time-dependent perturbations in the temperature field. During this stage of the process, bulge formation or spiral-like growth of the crystal is likely. The problem deteriorates if longer or wider side slits are applied. In both cases the relative difference between the EM power densities induced in the three-phase-line below the slitted and the non-slitted part of the inductor increases.
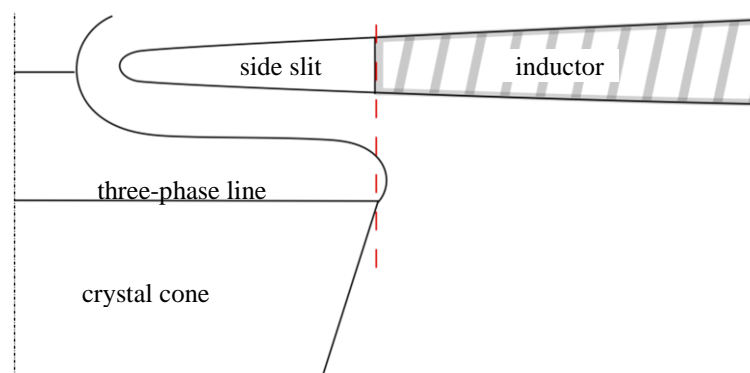

Figure 3-5   Critical phase while the diameter of the crystal cone is increased.

3.3 Impact of the Main Slit

The impact of the main slit in the inductor is similar to the impact of the side slits during the cone phase. The main slit can be considered as an infinitely long side slit. In particular in the growth of large-diameter crystals the impact of the main slit is critical. The current supplied at the inductor terminals flows mainly in radial direction and the surface current density has a relatively high magnitude at the opposing inner surfaces of the main slit, which causes a strong magnetic field mainly in vertical direction. The consequence is a distinct maximum of the induced eddy currents at the rim of the free surface below the main slit. The concentration of eddy currents and the consequent local release of a large amount of EM power close to the three-phase line give rise to a local thermal shock, being critical for the dislocation-free growth.

To illustrate the impact of the main slit, Figure 3-6 shows a detail of the inductor and the three-phase line below the inductor terminals. If it is assumed that the EM field is axisymmetric, the three-phase line is also symmetric and not influenced by the slits in the inductor. The rotation of the crystal with the rate Ω_C has then no impact on the shape of the three-phase line and the crystallization velocity v_C in vertical direction is identical to the pull speed $v_p = v_C$. The three-phase line for this case is represented by the dashed line in Figure 3-6.

If the main slit is considered, the EM field and, hence, the EM power distribution is not axisymmetric. In this case the local crystallization velocity v_C at a fixed position at the three-phase line varies due to the rotation of the crystal. In general, the shape of the three-phase line is not symmetric and the pull rate v_p represents only the average crystallization velocity.
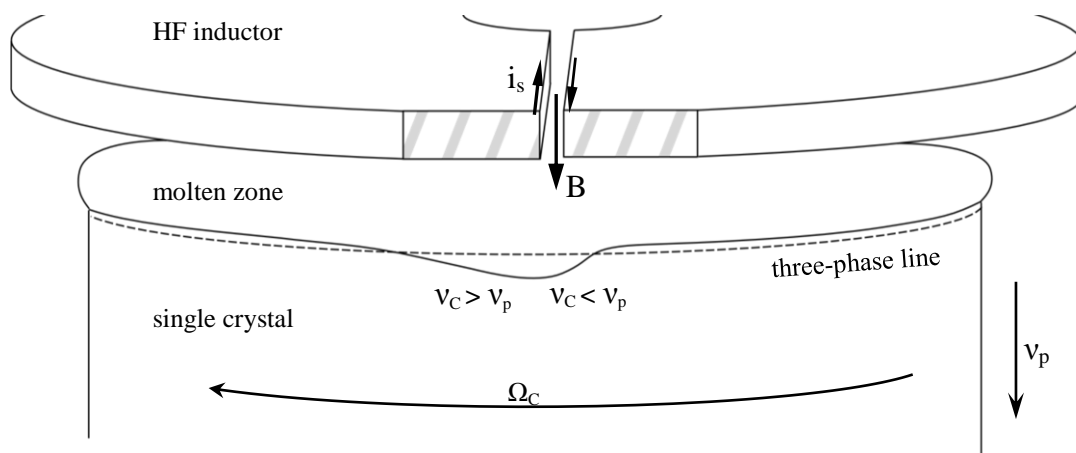

Figure 3-6   Sketch of the impact of the main slit in the inductor on the three-phase line.

The three-phase line influenced by the impact of the main slit is represented by the solid line in Figure 3-6. The deflection of the three-phase line is smaller than implicated in the Figure 3-6, but is visible to the naked eye during the process. According to the rotation rate the crystallization velocity of a point at the three-phase line varies in time. Due to the stronger heating below the main slit, the local crystallization velocity decreases ($v_C < v_p$) and the three-phase line deflects downwards until the necessary supercooling for solidification is reached.

If the main slit impact is strong enough, it is possible that v_C is zero or even back melting of already crystallized material occurs. Back melting is known to be a source for the generation of dislocations. Therefore, the crystal has to be pulled down with a sufficient rate to ensure the necessary supercooling before back melting occurs. Due to the rapid cooling at a point at the crystal region which has passed the main slit, the local crystallization velocity is higher than the pull speed ($v_C > v_p$). In general, there is also an upper limit for the pull rate after which dislocations are generated.

The involved temperature fluctuations in combination with crystal rotation and large thermal stress are known to cause growth instabilities and promote the generation of dislocations. As will be shown later in chapter 4, the thermal stress level is high in particular in the vicinity of the three-phase line. While it is evident, as a result of experimental observations, that the inhomogeneity of the EM field near the main slit is a source for the generation of dislocations, it is neither directly observable nor fully understood what specific mechanism causes the generation of dislocations. The cause is known only in certain cases, e.g. if a solid particle floats on the melt and reaches the three-phase line or if back melting is visible.

The presence of dislocations is usually not immediately noticed by the operator. The loss of structure is visible later when the characteristic ridges at the facets disappear. The ridges are related to the facet formation at the three-phase line. On the locally highly planar area of a facet the nucleation of new layers requires a larger amount of supercooling than outside the facet (see [60] for details). Consequently, the three-phase line at the facet lags behind the non-facetted part of the crystal rim, which results in the formation of a small lengthwise ridge at the crystal surface and a local melt overhang. A dislocation-free crystal grown in [100] direction shows 4 ridges, whereas a crystal grown in [111] direction shows 6 ridges, which are more or less pronounced. During growth these ridges vanish once the single crystalline structure is lost. The ridges represent an inherent deviation from axial symmetry of the three-phase line and promote the fluctuations of the EM power dissipation due to the impact of the main slit. The width of the ridges is related to the growth conditions (e.g. the rotation rate) and the shape of the crystallization interface near the rim of the crystal. Fine ridges usually indicate a sharp temperature gradient and a well-defined three-phase line,

whereas wide ridges are often a sign for the imminent disappearance of the ridges as a result of the generation of dislocations.

Certainly, diminishing the impact of the main slit is in favor for a dislocation-free growth process. To quantitatively evaluate the inhomogeneity of the EM field one may consider the induced surface current density at the three-phase line as a function of the azimuthal angle. The calculated current density at the ideal symmetric three-phase line in the 3D model is shown in Figure 3-7. Two different crystal diameters are considered. The locations of the maxima in the center correspond to the azimuthal position of the main slit. The current distribution is normalized by its value far away from the main slit, at the opposite side of the crystal.

As can be seen from Figure 3-7, the normalized current density at the three-phase line of the 4 inch crystal is 1.5 times higher in the vicinity of the main slit than it is at the base level far away from the main slit. The smaller local maxima in the curve are a result of the influence of the 3 side slits. In the 6 inch process the maximum is ca. 3.5 times higher than the base level. In combination with crystal rotation, the current maxima result in strong fluctuation of the Joulean heat generation at the crystal rim.

The impact of the main slit is increasing the larger the diameter of the growing crystal is. This can be explained by the fact that the induced current is relatively more concentrated in the center of the larger free surface. Therefore, the relative difference between the base level far away from the main slit and the maximum is increasing. The main slit impact is a serious problem especially in the growth of crystals of a diameter larger than 6 inches. Specific measures are needed to avoid the strong EM power fluctuations.

The vertical magnetic field through the main slit is related to the magnitude of the current flowing in radial direction at the inner surfaces of the main slit. The local magnetic flux
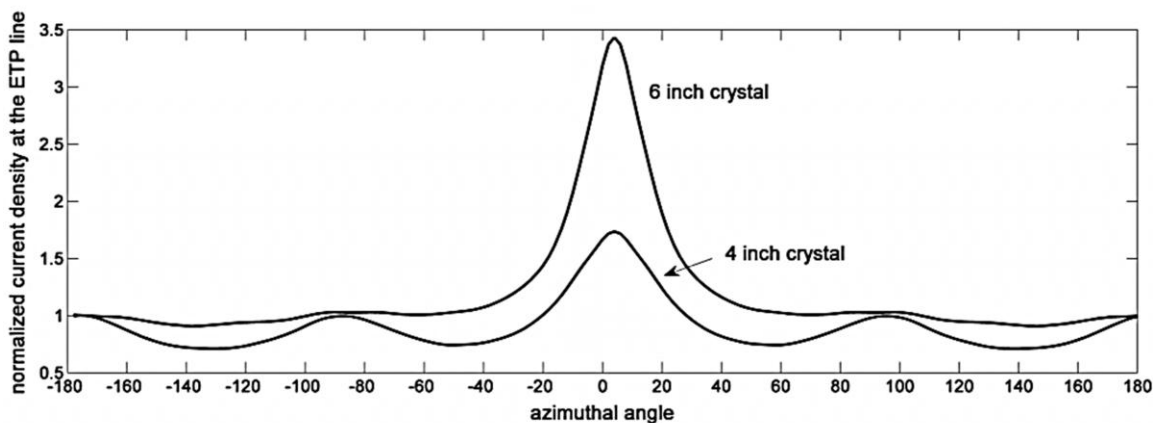

Figure 3-7   Normalized current density at the three-phase line calculated for different crystal diameters (The same inductor with a main slit width of 1mm is considered)

through a horizontal plane in the main slit depends on the magnetic field and the area described by the plane in the slits. Consequently, the impact of the main slit depends also on the width of the slit. Figure 3-8 shows the 3D distribution of the EM power density for different widths of the inductor's main slit. It can be seen that for a smaller slit width not only the power maximum decreases, but that also the maximum can be found closer to the center, further afar from the crystal rim. Hence, the main slit impact at the three-phase line can be lowered by reducing the width of the main slit. Reducing the width of the main slit is a comparably efficient and simple method to diminish the impact of the main slit. This is illustrated by a plot of the calculated current density along the three phase line for different slit widths in Figure 3-9. Commonly, a slit width of ≈1.5mm is applied since it is known from observation that a slit width below ≈1mm drastically increases the risk of arcing in a growth process. The risk of arcing can be reduced by lowering the working frequency of the inductor current as will be shown in Chapter 5.
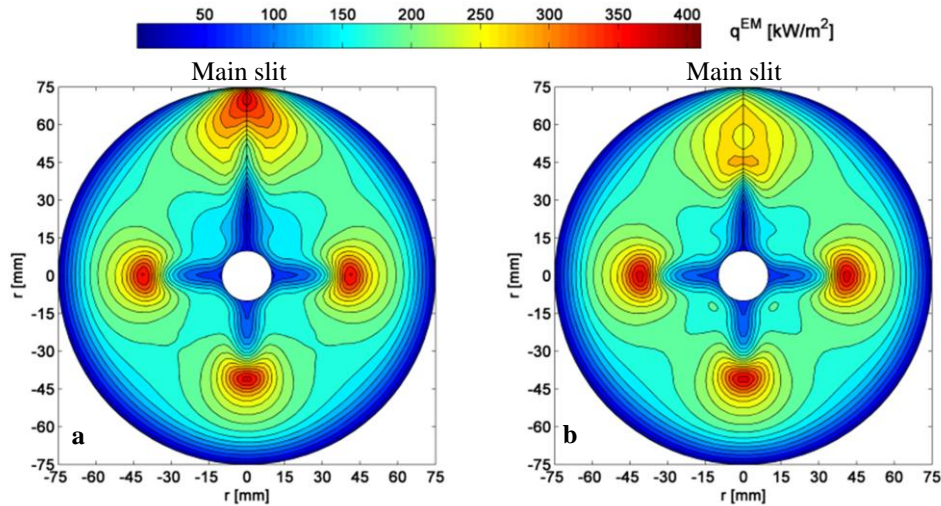
Figure 3-8   3D EM power distribution at the free melt surface (6 inch IKZ process)
                        a) Inductor with a main slit width of 1.5 mm
                        b) Inductor with a main slit width of 0.5 mm
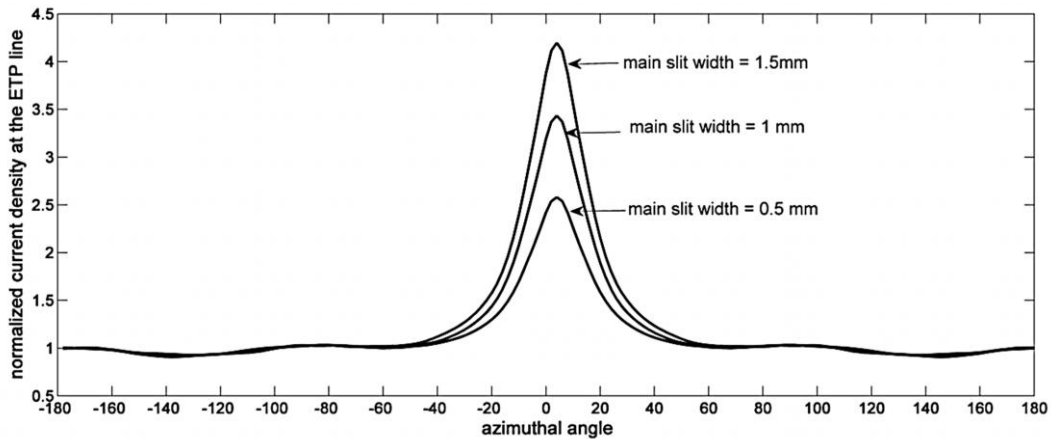
Figure 3-9   Normalized surface current density along the three-phase line for inductors with different
                        widths of the main slit (IKZ 6" process).

4. Thermal Stress

4.1 Thermal Stress in Large-Diameter Crystals

Generally, thermal stress is caused by inhomogeneous thermal expansion in a temperature field with non-vanishing second derivatives [61]. A temperature field which is linear in all coordinates results in a stress-free state, as the body only experiences free temperature bending [62]. For the temperature field in a crystal free of stresses it is true that:

$$\nabla^2 T = 0. \tag{4.1}$$

For example, a temperature field with a constant axial temperature gradient and zero radial temperature differences causes only thermal expansion of a cylindrical crystal and no thermal stress. Since high thermal stress is undesirable in crystal growth, this would be the ideal state in a growth process. The sources of thermal stress are incompatibilities of the temperature field [62]. Due to the production of latent heat at the crystallization interface and heat loss at the crystal surface, mainly due to heat radiation, the real FZ system always deviates from this ideal state. It is comprehensible that it is easier to achieve a temperature field close to the ideal state in a cylindrical crystal of small diameter and it gets increasingly difficult in a crystal with larger diameter.

Experimental observations clearly indicate that the risk for the generation of dislocations or cracking of the crystal is increasing when growing crystals with larger diameter, which is a result of higher thermal stress. Assuming a similar temperature distribution and linear scaling of the crystal dimensions in all directions, the stress field would be independent of the diameter of the crystal. However, in the growth of a larger crystal the temperature field is different and the shape of the crystal does not scale linearly. The measured maximum interface deflection is generally increasing with the diameter of the crystal as the production of latent heat is proportional to the square of the diameter (the area of the interface), while the area of the radiating surface of the crystal is approximately directly proportional to the diameter (the circumferential surface). Hence, with increasing crystal diameter, it becomes more and more difficult to dissipate the heat from the center of the crystal to the surface. Consequently, the center becomes hotter and the interface deflection increases.

A deflection of the crystallization interface means that there are radial temperature gradients in the crystal and, hence, non-zero second derivatives of T resulting in thermal stress. Even a linear radial temperature gradient results in thermal stress. Although a larger deflection of the crystallization interface, usually, is a sign for higher stresses present in the crystal, it is not possible to evaluate the thermal stress level entirely on the basis of the shape of the crystallization front, as it can be obtained e.g. from LPS measurements or temperature field calculations. Numerical simulation is essential to identify means to lower the thermal stress in the crystal. In the following, the impact of different growth conditions on the thermal stress field is studied. To put the results of the calculations shown later in context, it is first briefly elaborated on the generation of dislocations and crystal cracking due to thermal stress as known from the literature.

4.2 Dislocations and Crystal Cracking

Due to a thermal load a material first undergoes elastic deformation, which is reversible if the load is removed. A crystal, which was grown dislocation-free, is free of internal stresses after it is cooled down to constant temperature. If the yield strength in the crystal is exceeded during growth, the stress is released by irreversible plastic deformation or even cracking of the crystal.

The ideal strength of a material can be defined as the critical level of stress under which a perfect, infinite, homogeneous lattice becomes structurally unstable [63]. It is well known that crystals deform by slip. A simple approach to express the theoretical ideal strength required for slip is to consider the shear stress required for the slip of one entire plane of atoms sliding over another at the same time. Based upon this assumption Frenkel proposed that the ideal shear strength is in the order of one fifth of the shear modulus [64]. Nowadays more sophisticated models are developed to compute the ideal strength of silicon using ab-initio methods [65]. The theoretical ideal strength for silicon is high and gives only an upper limit for the stress that the crystal can sustain. As a matter of fact dislocation generation happens during the growth at much lower stresses. In 1934 Taylor, Polany and Orowan first postulated that crystals have preexisting defects (dislocations) and that it is not necessary for a whole plane to slip at the same time as the movement of dislocations allows slip to occur [63]. The critical stress for slip is the stress required to move a dislocation. During FZ growth the crystal may not contain dislocations if the Dash method is used. In [66] de Kock et al. discuss the possibility of the introduction of dislocations during FZ silicon growth as a result of point defect condensation. However, the precise mechanism of the introduction of dislocations in initially dislocation-free material is still not precisely known.

On the other hand, it is well known that the plastic deformation in crystals takes place along certain crystal planes and directions. The slip process must be considered in terms of the shear stress resolved on the slip plane in the slip direction. This was first proposed by Schmid and Boas [67]. Slip planes are usually planes with high atomic density. A slip plane and a slip direction lying in this plane form a slip system. In a diamond-like crystal like silicon the slip systems are determined by the {111} planes and the $\langle 1\bar{1}0 \rangle$ directions. To predict the generation of dislocations, a calculated stress state can be projected onto the slip planes to identify the effective shear stress acting in the slip direction. The slip process begins if the effective shear stress exceeds a critical temperature dependent value, which is a material parameter. From uniaxial tensile tests a critical value can be obtained at which plastic deformation is observed, the so called critical resolved shear stress (CRSS). The latter can be compared to the calculated effective shear stresses. The CRSS method was introduced by Jordan et al. [68], [69].

Especially for the high temperature region the data on the mechanical properties of silicon is scarce. Many thermal stress analyses in the literature for silicon single crystal growth (CZ and FZ) rely on the temperature-dependent relation for the CRSS provided by Miyazaki [57] given in Figure 4-1.

$$\sigma_{CRSS} = 10^{-7} \cdot \exp\left(10.55 + \frac{1.0147 \cdot 10^4}{T} \right) \text{MPa}$$
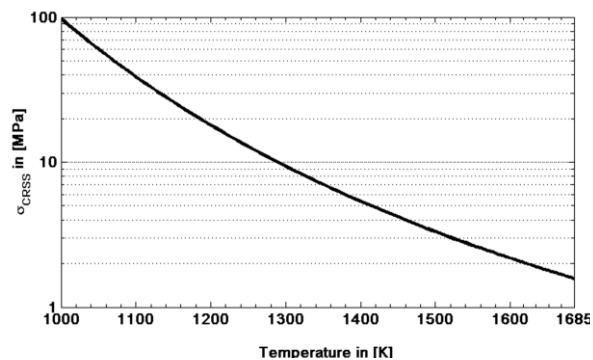
Figure 4-1 Critical shear stress for silicon according to Miyazaki [57]. The function is derived from measurements between 300K and 1288 K and allows extrapolation until the melting temperature.

The CRSS is decreasing with increasing temperature. An extrapolation until the melting temperature of silicon reveals values below 2MPa for the CRSS near the crystallization interface. As pointed out by Muiznieks et al. in [59], a principal problem arises if the CRSS method is used to predict the generation of dislocations. The thermal stress analyses in the literature for industrial crystal growth consistently exhibit a calculated thermal stress maximum near the crystallization interface, which exceeds the CRSS by more than an order of magnitude (for FZ see Riemann et al. [20] or Raming [26]). This implies that dislocations should be generated and represents a strong contradiction as crystals with large-diameter can be grown without dislocations.

Furthermore, it is known that dislocations are not only generated if a certain threshold of thermal stress is exceeded, but also occasionally more or less independent of the thermal stress level. In many cases it is not possible to clearly trace back the source or to reproduce their occurrence for a given set of growth parameters. The industry has to cope with the fact that a certain percentage of growth runs in an established process fail due to the generation of dislocations, even though the growth parameters for this process remain constant. On the other hand, unfavorable growth conditions, which generate very high thermal stress, more reproducibly cause the generation of dislocations or crystal fracture.

Based upon these issues, Muiznieks et al. [59] propose a qualitative concept for the occurrence of dislocations: It is assumed that at very high stresses always dislocations will be generated, while at moderate stresses the crystal is in a metastable state and a certain perturbation energy is necessary to leave this metastable state. This concept allows a relative analysis of dislocation generation, but not an exact prediction as the perturbation energy is unknown.

Perturbations that may induce dislocations are temperature fluctuations due to the melt motion or the inhomogeneity of the EM field. The latter can also cause back melting near the three-phase line as described earlier in 3.3. A solid particle, which floats on the melt and reaches the three-phase line, usually, causes dislocations in the crystal.

If the first dislocations are generated during growth, dislocation multiplication occurs and a slip process is initiated, in which dislocations propagate along specific slip planes back in the already crystallized material. The generated dislocation density depends on the initial stress in the material. As a result of the high thermal stress present in the crystal during FZ growth, intense multiplication of dislocations occurs, leading to a high dislocation density once the critical stress for the onset of dislocation generation is exceeded. This, finally, leads to the formation of grain boundaries and polycrystalline growth. It is not possible to grow a large-diameter silicon single crystal with dislocations by the FZ method.

In the development of a process for large-diameters the problem of crystal cracking may be observed. Figure 4-2a shows a crystal, which cracked during the cone phase of a growth experiment. If crystal fracture occurs always the lower, colder part is involved. Cracking leads to spillage of the melt volume in the chamber and immediately ends the experiment. As many materials silicon is brittle at lower temperatures and ductile at higher temperatures. As the temperature increases, silicon undergoes a brittle-to-ductile transition at 500-1000°C [70]. While the generation of dislocation is assumed to start near the crystallization interface, fracture of the crystal must be related to the stress in the lower part of the crystal.

Figure 4-2 b shows a photoluminescence measurement made on an axial cut of a crystal in which dislocation were generated during the process. The back gliding dislocations and the grain boundaries create a contrast in a photoluminescence picture. This provides a possibility to visualize the transition from dislocation-free to the polycrystalline growth of the crystal. The bright areas correspond to dislocation-free regions or regions of low dislocation density, whereas the darker areas correlate to regions of higher dislocation density. The sharp transition between the dark area and the grey area in the center marks the position of the crystallization interface at the time instant in which dislocations were generated during the process and, consequently, polycrystalline growth began. The dark area right below the sharp transition corresponds to the region of strong multiplication of dislocations and, hence, high dislocation density. The high dislocation density indicates high thermal stress in the vicinity of the crystallization interface. It is well known that the process of multiplication and dislocation gliding propagates about one crystal radius back into the dislocation-free crystallized material, the white area in the picture.

In [25] it is proposed by Raming that crystal fracture is a consequence of the generation of dislocations at the crystallization interface and the subsequent propagation into colder regions of the crystal. Unfortunately, it is practically impossible to distinguish if there were dislocations prior to the cracking or not, as both processes take place on a very short time scale and dislocations will be present in the cracked crystal in either case.

(a)   **(b)**
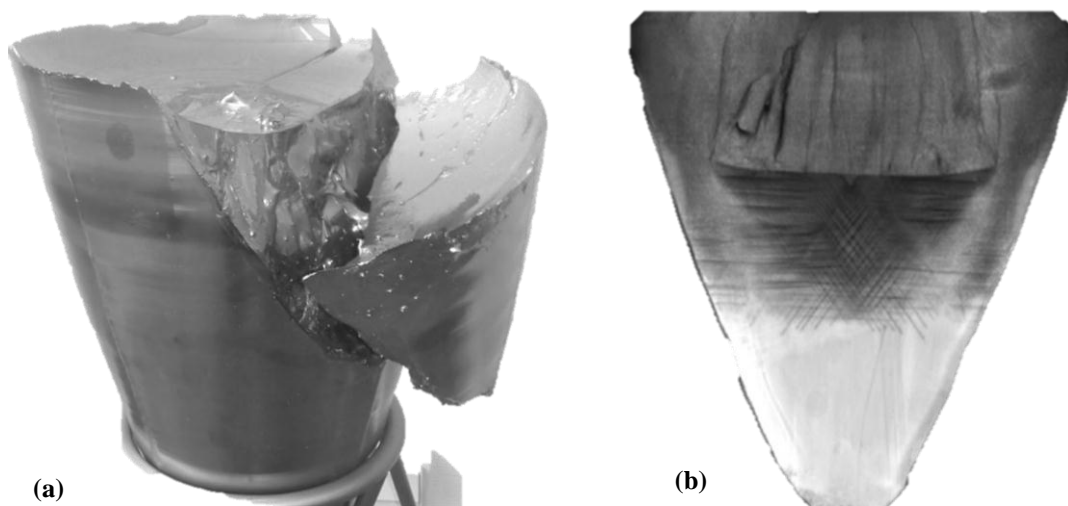
Figure 4-2   **a)** A large-diameter silicon crystal (D≈180mm), which cracked as a result of high thermal stress during the FZ process. (Courtesy of Topsil)

b) Photoluminescence measurement made on an axial cut of a crystal in which dislocations were generated during the process

4.3   Preventing high Thermal Stress

In the literature thermal stress analysis for large-diameter FZ silicon crystals is much more scarce than those for CZ silicon crystals (for CZ see e.g. Lambropoulos et al. [71], [72], Miyazaki et al. [57], Bornside et al. [73] or Noghabi et al. [74]). The thermo-elastic stress in large-diameter FZ crystals has been studied so far e.g by Mühlbauer et al. [20], Riemann et al. [19] and more intensively by Muiznieks et al. [59] and Raming [25]. In the latter works also the influence of crystal diameter, interface deflection and the impact of an external reflector is studied.

In the development of a process for large-diameter crystals thermal stress is critical and measures to reduce thermal stress are required. In the following, the influence of some of the most important process parameters on the thermal stress level is exemplarily evaluated and compared. Furthermore, the influence of an additional radiation heater and the impact of convective cooling due to the gas atmosphere in the chamber is considered.

As explained earlier in 2.5, the stress state is generally determined by 6 independent components of the stress tensor **σ**. This makes the interpretation and visualization of the stress state difficult. To evaluate the stress state, the equivalent tensile stress or von Mises stress is used, which can be derived from the general form of the stress tensor as:

$$\sigma_{vM} = \sqrt{\frac{1}{2}\left[\left(\sigma_{11} - \sigma_{22}\right)^2 + \left(\sigma_{22} - \sigma_{33}\right)^2 + \left(\sigma_{33} - \sigma_{11}\right)^2 + 6\left(\sigma_{12}^2 + \sigma_{23}^2 + \sigma_{31}^2\right)\right]} \qquad (4.2)$$

The von Mises stress is a scalar value which is often invoked to predict yielding in materials under multiaxial load. The projection of the stress state to the slip planes requires a 3D model and is omitted. It is assumed that a relative analysis of the impact of the growth parameters is possible by comparing the calculated von Mises stresses. Growth conditions that reveal a lower von Mises stress should be favorable for the dislocation-free growth. The von Mises stress usually shows a maximum near the crystallization interface and, hence, the evaluation is focused on the stress near the crystallization interface. As explained earlier, the CRSS is generally much lower than the calculated maximum of the von Mises stress and is minimal near the crystallization interface.

Considering the region where the calculated stress exceeds the CRSS can serve as a measure to estimate the dislocated region in the crystal (see Miyazaki [56], [57], [75]). The limited applicability of this method has been pointed out by Maroudas et al. [76]. However, as the focus in the current analysis is on preventing the onset of dislocation generation, which is assumed to occur near the crystallization interface, a comparison of the von Mises stress with the CRSS is redundant.

The impact of different growth parameters on the thermal stress level is exemplarily studied on the basis of a 6 inch IKZ process. The inductor parameters are those of the reference inductor considered in chapter 3 (side slit length=40, side slit width=3 mm, lower angle =4°). The pull speed is 2.5 mm/min and the crystal length is 150mm. Figure 4-3 shows the isolines of the temperature, the hydrostatic stress and the von Mises equivalent stress in the crystal for this reference case, calculated with the axisymmetric model.

The temperature gradient in the vicinity of the interface is about 120 K/cm^2, with a strong axial component, which is visible by the isotherms being close together near the crystallization interface. Apparently, there is also a considerable radial component of the temperature gradient as the isotherms bend upwards in radial direction. This leads to a stronger expansion of the crystal in the central part, where it is hotter. The hydrostatic stress component can be obtained from the stress tensor with: $\sigma_h = \frac{1}{3}(\sigma_{11} + \sigma_{22} + \sigma_{33})$. The hydrostatic stress component can be seen as a measure for the pressure or the tension exerted by the stress, which causes a change of the volume. The hydrostatic stress is varying from -20 MPa to 45 MPa, indicating compression in the central part and tractive forces in the crystal periphery, near the crystallization interface.

The von Mises equivalent stress is maximal at the crystallization interface and rapidly decreasing in direction to the seed, where the crystal is fixed. A global maximum can be found in the center and a local maximum is located at the crystal rim. In the reference configuration the global maximum is 72 MPa and the stress at the rim amounts to 59 MPa.
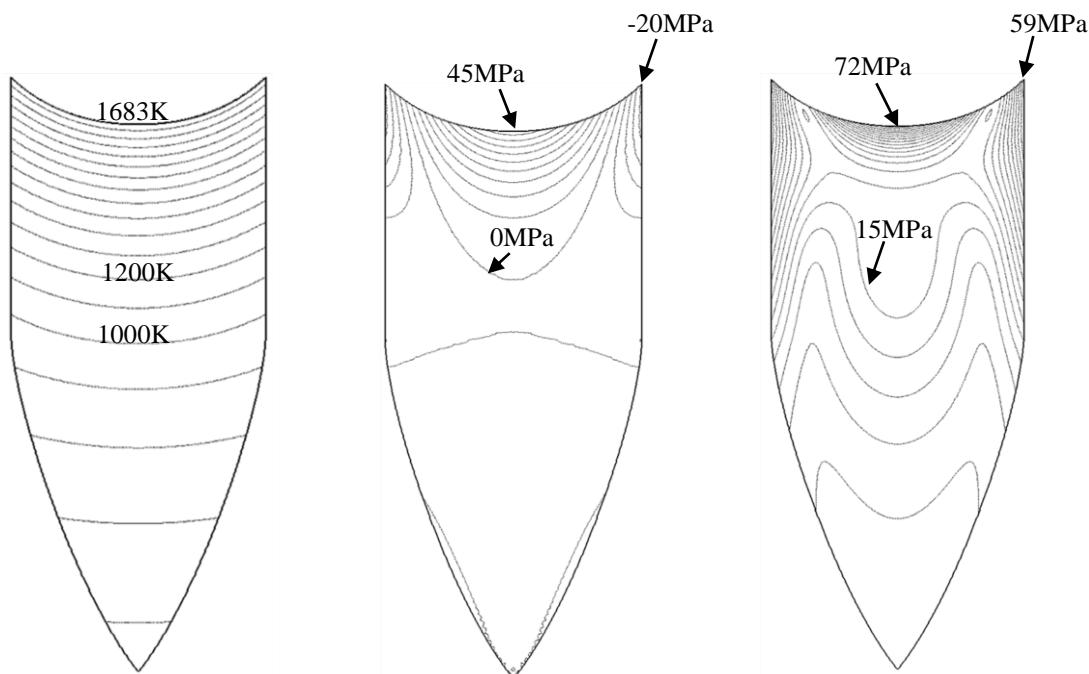
Figure 4-3   Isolines of the temperature (ΔT=50K) the pressure and the von Mises stress
                      (Δσ=5MPa) in a 6 inch crystal during growth.

Figure 4-4 illustrates the principal impact of increased pull speed and the effect of the application of a reflector in the vicinity of the crystal rim, respectively. The maximum stress increases if the crystal is pulled downwards faster, whereas the application of a reflector decreases the maximal value of the von Mises equivalent (+10MPa vs. -8 MPa). In both cases the interface deflection increases (+6 mm and +3mm).

Additional reflectors, also called thermal shields, are currently used in the industrial FZ process to reduce thermal stress in the crystal. Reflectors are mounted below the inductor and need to be water-cooled as being exposed to the intense radiation from the hot zone. According to the emissivity of the reflector material and the local temperature of the crystal, radiation is reflected back to the crystal surface. The diminishment of heat dissipation at the crystal surface reduces the radial component of the temperature gradient near the surface.
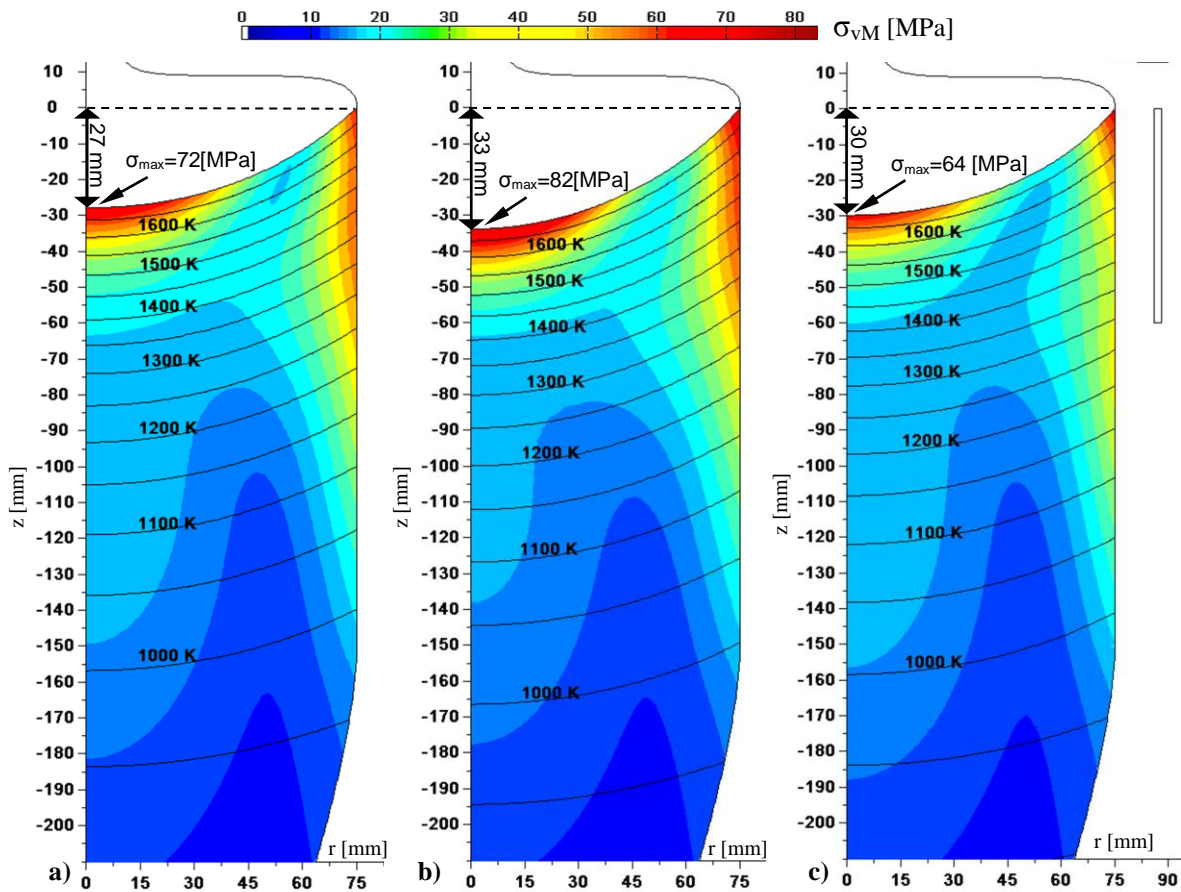
Figure 4-4   Isotherms (ΔT=50K) and von Mises stress in the growing crystal (6 inch IKZ process)
                        a) Reference (no Reflector, v_{pull} = 2.5 mm/min, crystal length =150 mm)
                        b) Pull rate increased to v_{pull} = 3 mm/min
                        c) An additional reflector with a length of 60 mm is applied

Consequently, more heat is conducted downwards in the center because it is trapped in the crystal. The axial gradient in the center is decreasing and the crystallization interface deflection is increasing. That the presence of a reflector increases the interface deflection was also experimentally found by Luedge et al. in [18]. The presence of a reflector decreases the von Mises stress mainly in the center, whereas the stress level close to the ETP is more or less unaffected. Figure 4-4c shows that the reflector decreases the thermal stress mostly in the vicinity of the crystal surface below the ETP.

In the model the top of the reflector is horizontally aligned with the ETP. In the simulation this configuration shows to be most effective to reduce the stress near the crystallization interface. In practice the reflector is usually mounted lower. For the operator and the process control measurement system, the three-phase-line must be visible during the process. Furthermore, in experiments it has been observed that the three-phase line tends to undulate if the reflector is too close to it. If the three-phase-line undulates, the melt meniscus becomes unstable as the melt is not properly supported by the solid below and melt spillage is likely.

Less Joulean heat is necessary in the simulation in the case when a reflector is applied. In this respect the use of a reflector could also help to reduce the risk of arcing as less EM power and, hence, lower voltage is necessary at the inductor terminals. However, in the calculation it is not considered that the EM field may couple with the reflector, which would counteract this positive effect. If the reflector is close to the inductor, it has to be slotted to avoid coupling to the EM field. The use of copper or silver as a reflector material is preferred due to their low emissivity, but also the use of non-conducting materials is possible. In [18] Luedge et al. use double-walled silica rings filled with titanium oxide powder and an aluminum oxide ring as a reflector and study the effectivity in comparison to conventional copper reflectors. It is concluded that these reflector types have the same efficiency compared to a conventional copper reflector.

Figure 4-5 shows the relative impact of a variation of the most important process parameters on the interface shape and the thermal stress along the crystallization interface. It is assumed that the von Mises equivalent stress at the crystallization interface is relevant and not the stress deeper in the bulk of the crystal. In all configurations the stress maximum is located in the center at the interface. However, the precise origin of the generation of dislocations is not known and the stress at the ETP amounts to high values, too.
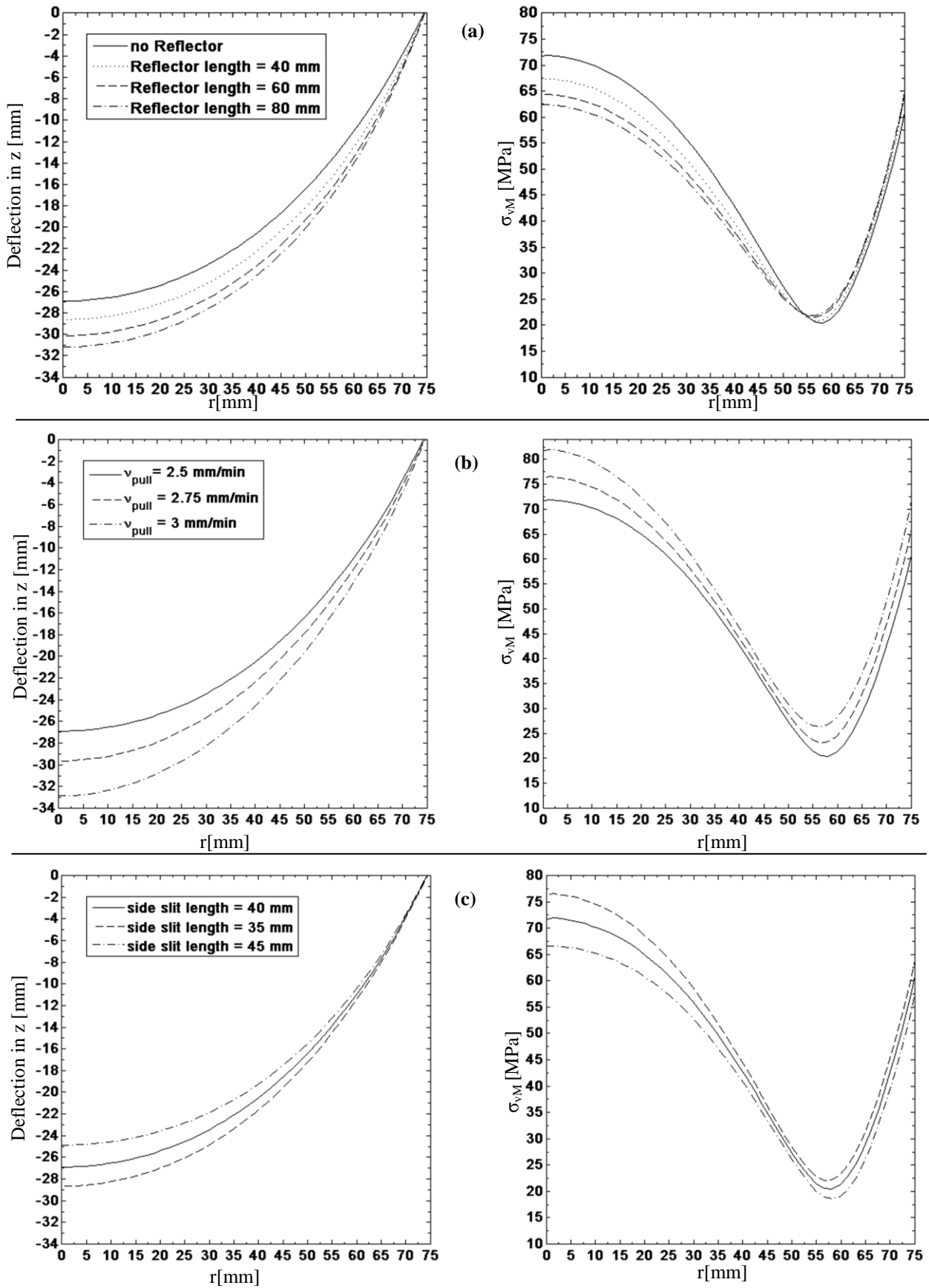
Figure 4-5   Crystallization interface shape and von Mises stress along the interface for:
      a) different lengths of the reflector
      b) variation of the pull rate
      c) variation of the lengths of the side slits in the inductor

The Figure 4-5a shows the influence of a prolongation of the reflector in vertical direction, for a fixed upper position horizontally aligned to the ETP. The case without reflector is shown for comparison. The presence of a short reflector of 40mm length increases the interface deflection by 2mm and the maximum of the von Mises stress in the center is only reduced by -4 MPa. The prolongation of the reflector to 60 mm intensifies the positive effect (-7MPa), whereas the effect of a prolongation further to 80 mm brings a smaller additional benefit regarding the maximum stress level. In all the considered cases the reflector increases the maximum interface deflection and decreases the axial component of the temperature gradient in the center. The presence of a reflector can lead to a decrease of the interface deflection if its top is mounted close to the three-phase-line like in Figure 4-4c and its length is much smaller than in the cases shown here. That a short reflector can lead to a decrease of the maximum interface deflection was experimentally found by Luedge et al. in [18].

An increase of the pull speed basically influences the temperature field in two ways. The faster transport of heat by the downward movement of the crystal decreases the axial gradient in the lower part and stretches the isotherms in axial direction. The lower part of the crystal becomes hotter. Secondly, the stronger production of latent heat increases the temperature gradient in the hot zone below the crystallization interface. The interface deflection and the maximum von Mises stress in the center are increasing.

It should be pointed out that in the case of a reflector the maximum interface deflection is increasing but the stress maximum is decreasing, whereas in the case of a higher pull speed an increase of the maximum deflection is related to higher thermal stress (see Figure 4-4b,c). The crystallization interface deflection, which can be measured, gives only limited information about the stress present in the crystal during growth.

As can be seen in Figure 4-5b, the interface shape and in particular the stress is very sensitive to variations of the pull speed. An increase of the pull speed from 2.5 mm/min by only ¼ mm/min increases the maximum deflection by 3 mm. The stress in the center as well as at the crystal rim increases by 5 MPa. Therefore, decreasing the pull speed is a potent measure to lower the thermal stress. The pull speed has to be significantly lowered the larger the diameter of the crystal in the process is. On the other hand, a too low pull speed promotes the generation of dislocations, i.e. as a result of local back melting at the three-phase line due to the inhomogeneity of the EM field below the main slit as explained earlier in 3.3. This underlines again the necessity to reduce the inhomogeneity of the EM field. Furthermore, a too low pull speed causes instabilities of the melt neck and leads to a deteriorated melting behavior as the production of melt at the open melting front diminishes.

Also the extents of the side slits in the inductor have a strong influence on the thermal stress level. Figure 4-5c shows the influence of different lengths of the side slits. The EM power distribution in dependence of the side slits in the inductor has been discussed in section 3.2. The 3D EM power distribution and the azimuthal average of the Joule heat dissipation for the specific slit configurations used for the computation of thermal stress can be found in Figure 3-3 and Figure 3-4, respectively. It has been shown that the application of longer slits reduces the power dissipation in the center. Consequently, longer slits lead to a smaller deflection of the crystallization interface and vice versa.

Furthermore, it can be concluded that increasing the length of the side slits reduces the thermal stress in particular in the center, while the magnitude at the rim is only marginally affected by a change of the slit length. Therefore, prolonging the side slits is potentially a measure to reduce the stress in the crystal. However, it has to be emphasized that this is a result of the quasi-stationary axisymmetric simulation only. The local temperature perturbations, which may increase if the slit length is increased, are not taken into account. The adverse impact of a huge increase of the extents of the side slits, e.g. regarding the melting behavior of the feed, has already been discussed in 3.2.

4.4   Additional Radiation Heater

The influence of a reflector is limited by the fact that it is a passive heating element. Radiation from the crystal surface is reflected according to its emissivity and the local temperature at the crystal. It is well known that the radiative intensity steeply rises with the fourth power of the temperature, as expressed by the Stefan-Boltzmann law. The influence of a reflector diminishes with decreasing temperature of the crystal surface and is, therefore, less efficient at the lower part of the crystal, below the hot zone. In the following it is elaborated on the possibility to actively heat the crystal surface by infrared radiation, additional to the inductive heating. The benefit of actively heating the crystal by radiation is that the irradiated power is adjustable at will, which allows influencing the thermal field on a larger scale than it could be done by modifying the extents of a passive reflector ring.

For the purpose to experimentally investigate the principal applicability of an additional radiation heating system in a FZ growth process, the setup shown in Figure 4-6 was used. Near infrared (NIR) tube emitters were evenly arranged concentrically around the crystal. The arrangement provides a homogeneous axisymmetric distribution of the radiant power absorbed by the crystal surface. The emissivity of solid silicon is temperature dependent,

increasing with decreasing temperature, and amounts to a relatively high value of about 0.5 in the given temperature range. Hence, good absorption of the irradiated power is provided. Each of the 9 emitters delivers a maximum radiant power of 600W. The radiation emitters are encased by a water-cooled reflector ring to minimize the losses to the surroundings. The applied radiant heating system has proven applicability and robustness in the harsh conditions in the growth chamber. The quartz tubes of the emitters are vacuum-tight and do not contaminate the gas atmosphere or the growing crystal. Vacuum tightness is necessary as the chamber is usually evacuated prior to the process to evaporate water residues, which may be present at the chamber walls after cleaning. A photograph of the radiation heater setup can be found in the appendix (see Figure 7-4).

In the experiment a crystal of 5 inches diameter was grown. Three different cases were investigated in one process. At first a reference case was studied in which no voltage was applied to the emitters. In this case radiation is reflected by the reflector behind the lamps. Afterwards two cases were investigated in which the radiation heater was switched on, supplying a power of 1.3 kW and 2.6 kW, respectively. At each level, about 7 cm of crystal length were grown to allow the temperature field to return to an approximately stationary state. The corresponding crystallization interface shape for each case was measured by the LPS method.

The results of the measurements are shown in Figure 4-7. In the reference case, in which the radiation heater was switched off, the maximum interface deflection measured is 27.6 mm. For the case where the radiation heater irradiated a total power of 1.3kW a higher maximum interface deflection of 28.4 mm was measured. Increasing the power of the radiation heater to 2.6 kW consistently led to an increase of the interface deflection by 1 mm. To exclude any influence of the increasing crystal length another measurement (not shown here) was conducted on a crystal section, which was grown after the radiation heater was switched off again. This measurement showed a maximum deflection of 27.3 mm and revealed that the maximum interface deflection returned to about its value before the heater was switched on. It is known that the interface deflection tends to slightly decrease as the surface area of the crystal is increasing during growth. It can be concluded that applying the radiation heater increased the interface deflection.
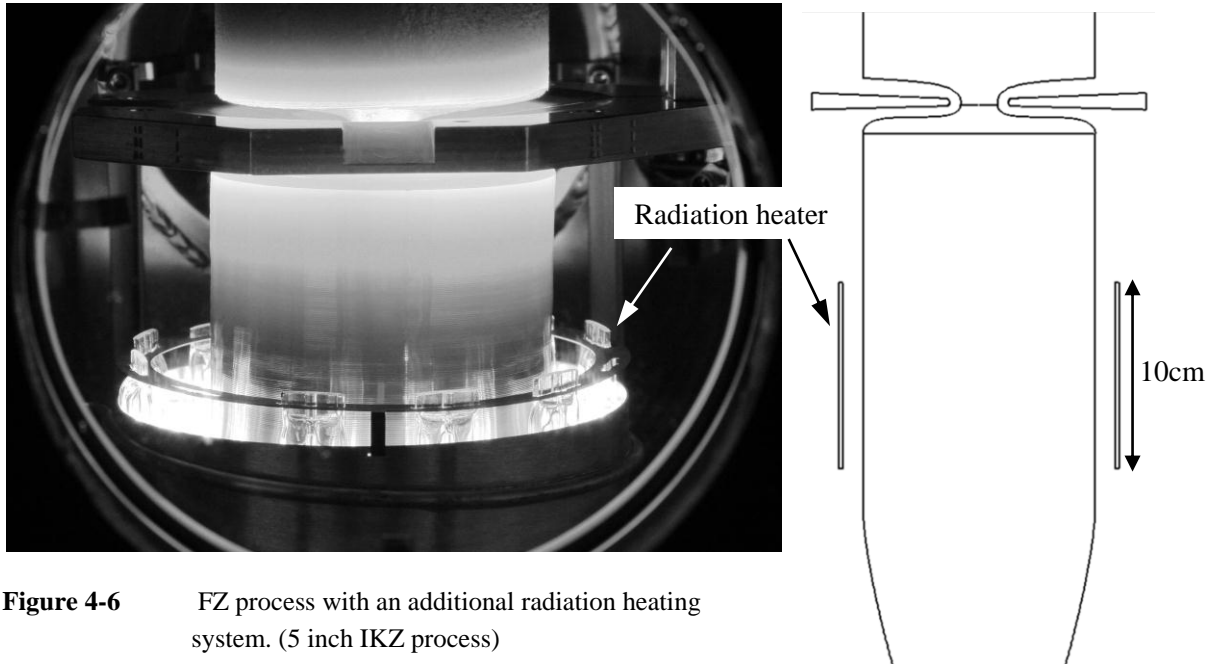
Figure 4-6   FZ process with an additional radiation heating
                      system. (5 inch IKZ process)
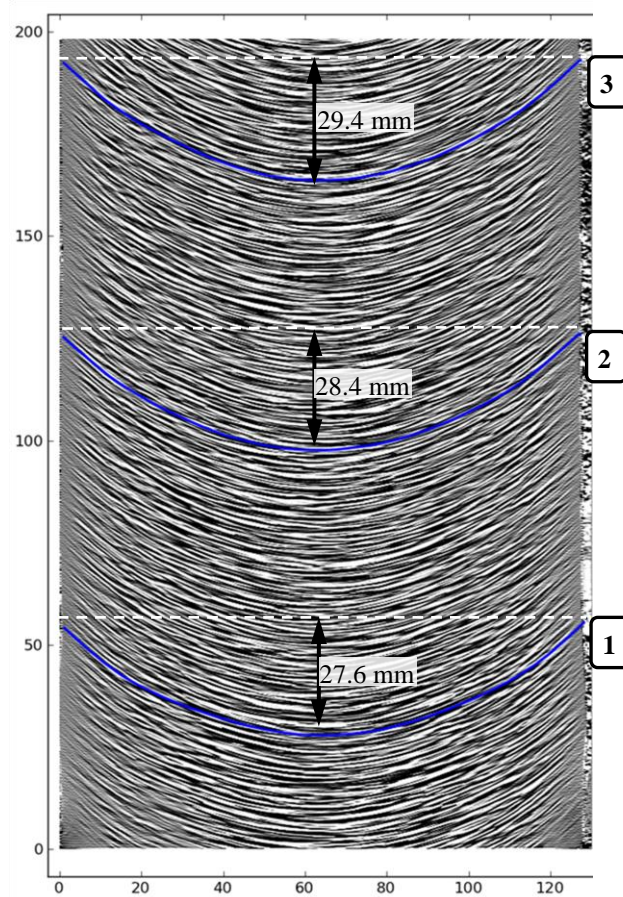

Figure 4-7   The LPS method was used to measure the crystallization interface shape on an axial
                      cut of a crystal grown with an additional radiation heater.
                      1: Reference: radiation heater is off.
                      2:1300 W radiated power.
                      3: 2600 W radiated power.

Based on this experiment no direct conclusion can be drawn whether the additional radiation heater is effective in reducing thermal stress as the stress cannot be measured. Augmented thermal stress becomes only visible if the crystal cracks or dislocations are generated, which usually does not happen in the growth of a crystal of 5 inch diameter at standard process conditions. Nevertheless, it shows that the dislocation-free growth with an additional radiation heating system is possible and that the temperature field near the crystallization interface can be influenced by actively heating the lower part of the crystal. The increase of the crystallization interface deflection indicates a lower axial temperature gradient near the interface. A similar result was obtained in the simulations considering a long reflector. In contrast to a reflector, a radiation heating system allows to influence the temperature field in the lower, colder part of the crystal. Reducing stress in the lower region could be beneficial if crystal fracture is a result of high thermal stress in the temperature region below 1000°C, without prior generation of dislocations. If cracking of the crystal is only a consequence of the prior generation of dislocations, the stress in the vicinity of the crystallization interface is relevant.

Therefore, also the question is investigated if a radiation heating system can be more efficient than a reflector in diminishing the thermal stress near the crystallization interface. Figure 4-8 shows the result of a calculation, in which a radiation heater is assumed being close to the ETP, similar to the position of the reflector considered earlier. The radiation heater is modeled as described in 2.4. A radiative heat flux is specified at the emitter surface with a vertical extent of 60mm, so the crystal surface is irradiated by a total power of 6kW. The result is compared to the case without a reflector and the case with a reflector of 60 mm length. It can be seen that a radiation heater can be superior to the reflector in reducing thermal stress in the center. On the other hand, a reflector is an efficient measure to reduce stress. More efficient is the combination of reflector and radiation heater shown in Figure 4-9. The radiation heater is placed below the reflector. A total power of 4kW is specified. This configuration drastically increases the maximum interface deflection and diminishes the stress in the center (see Figure 4-10). In this case the maximum von Mises stress is located near the ETP.

All the measures to reduce stress having been investigated have in common that only the stress in the center of the crystallization interface could be influenced, whereas the von Mises equivalent near the ETP remains practically unaffected or slightly increases. The stress reduction is related to a decrease of the axial temperature gradient in the center. However, the presence of an axial temperature gradient is the precondition for solidification and cannot be avoided.
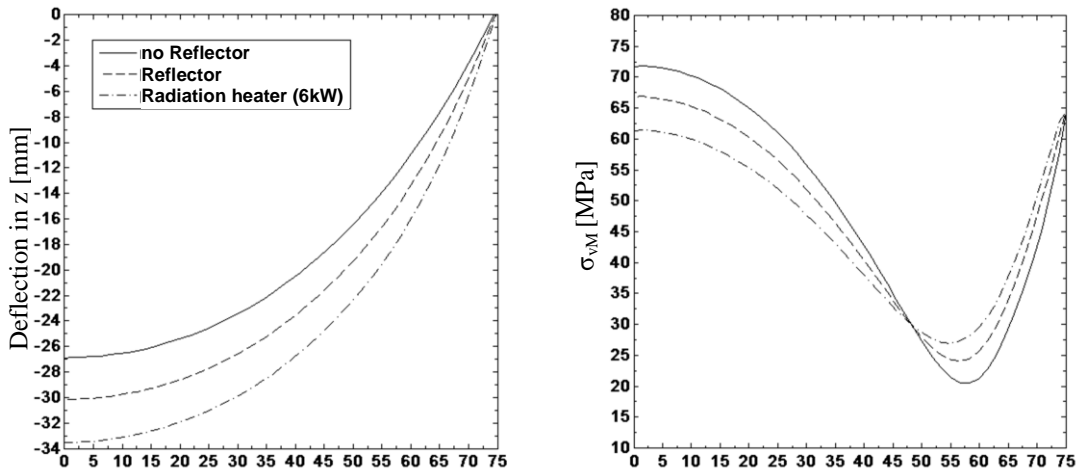
Figure 4-8   Influence of a radiation heater near the ETP on the interface deflection
                       and von Mises stress in comparison to the case without a reflector and
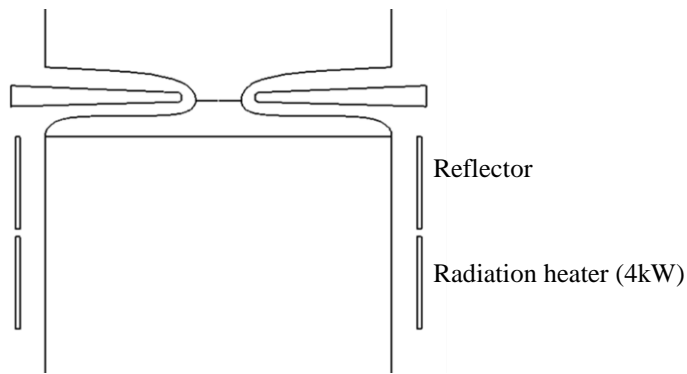   a 60 mm long reflector.

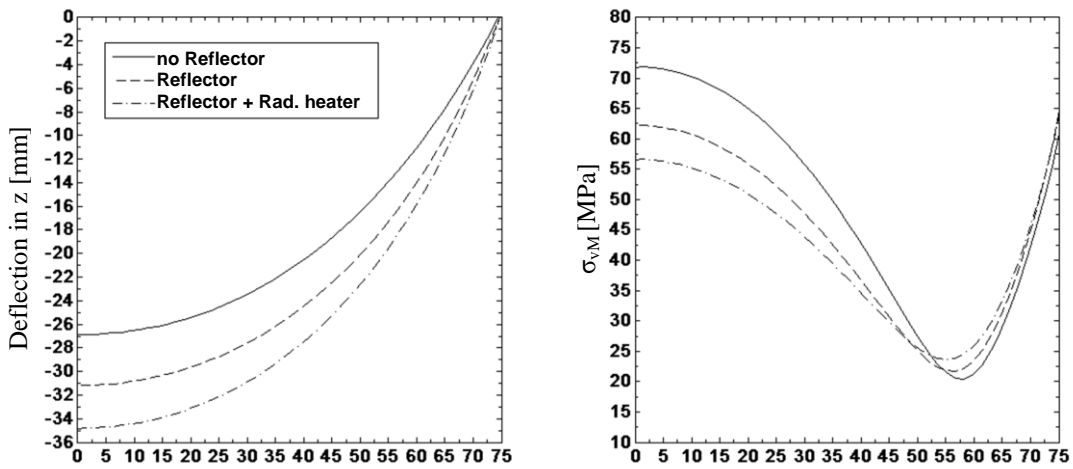**Figure 4-9**   Combination of reflector and radiation heater.

Figure 4-10   Interface deflection and von Mises stress for a configuration, in which the radiation
                        heater is mounted below a reflector as shown in Figure 4-9.

4.5   Impact of Convective Cooling

The following discussion is motivated by the observation that, in a large-diameter process, crystal cracking and generation of dislocations occurs more frequently at higher pressure of the argon gas atmosphere in the chamber. In the industrial FZ process, high gas pressure is preferred as this reduces the risk of arcing at the inductor. Higher gas pressure promotes natural convection and may increase convective cooling of the crystal. The heat in the crystal is dissipated mainly by radiation to the sourrounding chamber walls, which are water-cooled. Especially at elevated temperatures, radiation is the dominant heat transfer mechanism. Nevertheless, there is an additional heat transfer to the gas. It is well known that convective cooling depends on the flow characteristics and the fluid properties, which are a function of temperature and pressure. In the FZ system the gas flow is driven by bouyancy forces as a result of the temperature differences between crystal, gas atmosphere and chamber wall. A fluid flow driven by bouyancy forces can be characterised by the dimensionless Grashof number:

$$Gr = \frac{g\alpha\rho^2\Delta T L^3}{\eta^2}$$

g gravitational constant	α coeff. of thermal expansion
ρ density	ΔT Temperature difference
L characteristic length	η dynamic viscosity

(4.3)

A higher pressure increases the density and, hence, strongly promotes natural convection. Published data for the characteristics of the gas flow during an FZ process is scarce. In [35] Larsen et al. estimate the heat transfer by convective cooling in the FZ system with the help of an empiric formula, which is valid for a vertical, free-standing and isothermal cylinder surrounded by a gas. Based on the same relation, in [25], a significant influence of the gas pressure on the temperature in the crystal was rejected. However, depending on the scope the applicability of empiric relations is limited.

To shed more light on this issue, temperature measurements were conducted to roughly estimate the impact of the gas pressure on the temperature and thermal stress field in the crystal. Measuring the crystal temperature during an FZ process is difficult to realize. Therefore, a configuration was used, which is assumed to be similar to the FZ process. A cylindrical silicon rod was heated up to melting temperature at the top using a standard HF inductor. The generator power was increased until the center of the top of the rod was molten. With several thermocouples the decline of the temperature in the rod due to radiation and convective cooling was measured at the circumferential surface. The use of thermocouples has shown to be more suitable than a pyrometric measurement, as interferences due to reflection of radiation from the chamber walls is hard to avoid. Thermocouples allow a precise measurement in a wide temperature range.
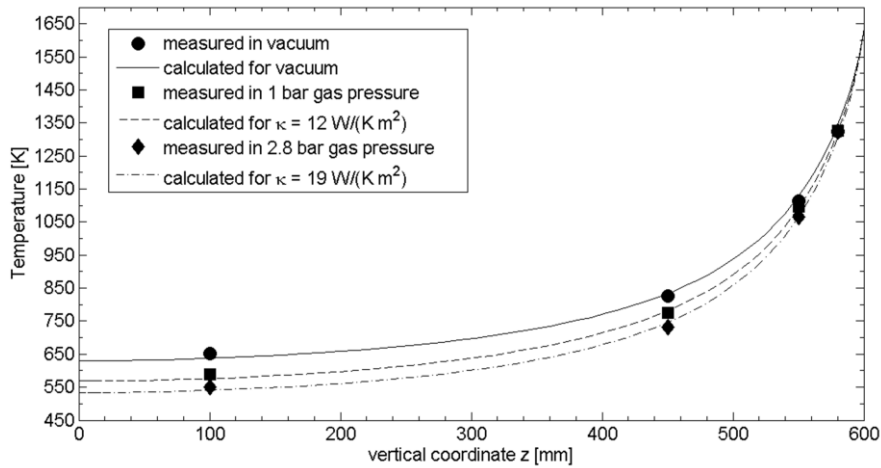
Figure 4-11   Measured temperatures along the rod surface at different
                       gas pressures and calculated temperature slope for different
                       heat transfer coefficients.

The sheathed thermocouples of type K were brought in close contact to the rod by inserting them into small holes of 3mm depth, which were drilled in the rod. No interference due to the EM field was observed. The temperature along the rod surface was measured at an absolute pressure of 1 bar, 2.8 bar and in vacuum for comparison. The temperatures measured at the 4 thermocouples vertically distributed along the rod surface are shown in Figure 4-11. The measurements reveal the steep temperature gradient due to radiation, which is the governing heat transfer mechanism in the upper part of the rod. The impact of convective cooling is better visible in the lower part of the rod. In comparison to the measurement in vacuum, lower temperatures are obtained in the pressurized chamber. Comparing the values at 1bar and 2.8 bar, lower temperatures are obtained for higher gas pressure. It can be concluded that higher gas pressure increases the heat transfer to the gas, as the rod in the lower part was colder. The measuring method used is not very accurate. It cannot be excluded that the thermocouples were directly cooled by the gas and, hence, lower temperatures were obtained than actually present at the rod surface. However, a small but distinct difference between the temperatures at 1bar and 2.8bar was measured.

In a simulation the heat transfer to the gas atmosphere can be described with:

$$q^c = \kappa \left(T - T_G \right) \tag{4.4}$$

where κ is the average heat transfer coefficient, T the local temperature of the crystal surface and T_G the temperature of the ambient gas, i.e. the temperature of the filling gas far away from the crystal surface. To consider the impact of the pressure, κ must be expressed as a function of the gas pressure.

The procedure applied to obtain an average value for the heat transfer coefficient κ for a specific pressure was to bring a simulation of the experiment in agreement with a calculation,

in which heat transfer to the gas is modeled with eq. (4.4). The top of the cylinder in the model is set to melting temperature and heat transfer by conduction and radiation is modeled as described in 2.4. It is accounted for the temperature dependence of the emissivity and thermal conductivity of solid silicon. A thermocouple measurement yielded an average gas temperature of $T_G = 490K$.

The measurement in vacuum allowed determining the emissivity of the chamber wall. The emissivity of the chamber wall in the model was adjusted to bring the calculated temperature slope in agreement with the temperatures measured in vacuum. The emissivity was set to 0.2 in all calculations. Similarly, by varying κ and minimizing the sum of squared residuals, an approximate value for the heat transfer coefficient corresponding to the specific gas pressure is obtained. The least-square minimization can be written as:

$$\min_{\kappa} \sum_{n=1}^{N} \left(T_n^{measured} - T_n^{calculated} \right)^2 \tag{4.5}$$

In this way a heat transfer coefficient of $\kappa=12$ W/(Km^2) for 1 bar and $\kappa=19$ W/(Km^2) for 2.8 bar is obtained. Assuming the conditions during FZ growth are similar to those in the experiment, the result can be adapted to the global model of the FZ process.

Figure 4-12 shows the shape of the crystallization interface and the von Mises equivalent stress along the interface for the case without convective cooling and two other cases, in which heat transfer coefficients as obtained for different gas pressures are considered.

The interface deflection is decreasing if convective cooling is taken into account. The difference between the calculations with different heat transfer coefficients is relatively small but it can be seen that, with higher heat transfer coefficient, the interface deflection is further
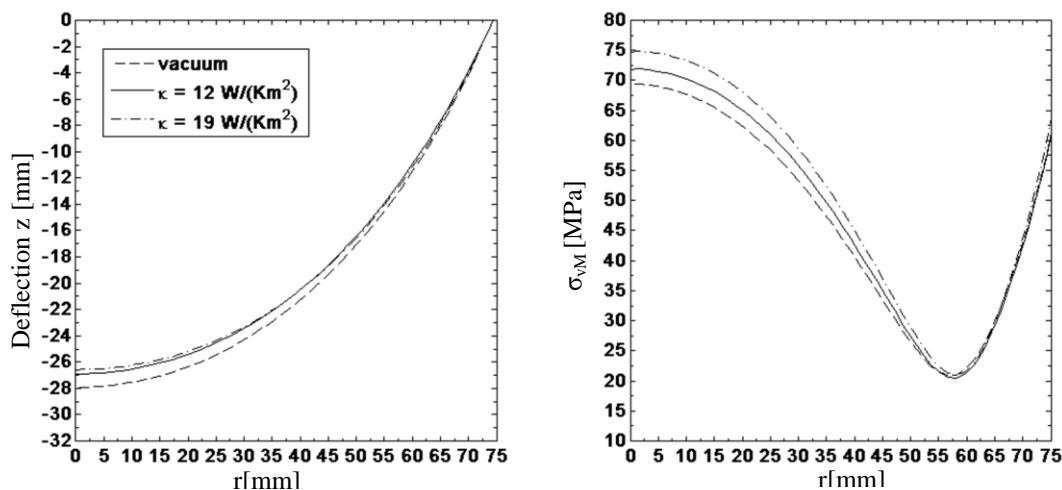
Figure 4-12   Crystallization interface shape and von Mises stress along the interface without convective cooling and for different heat transfer coefficients.

decreasing. This result is qualitatively in agreement with the result of Larsen [36], who also experimentally found that the interface deflection is smaller at higher gas pressures. The experiment with the radiation heater described earlier in this chapter revealed that the interface deflection is increasing if the crystal is additionally heated at its surface. The current result is consistent in this respect as increased heat transfer to the gas is virtually the reverse effect.

It has been mentioned that the mechanism and the origin of crystal cracking and generation of dislocations is not precisely known so far. As the impact of convective cooling on the temperature field is more pronounced in the lower part, also the thermal stress is more influenced in the region far away from the crystallization interface. Nevertheless, the calculation of thermal stress reveals, that the von Mises equivalent is also considerably higher at the crystallization interface as a result of the stronger heat transfer to the gas (see Figure 4-12). This could explain why crystal cracking and generation of dislocations is more frequently observed if higher gas pressure is used. The investigated pressure range is comparably small, as the crystal puller used does not allow pressures higher than 2.8 bar. In the industrial growth of large-diameter crystals much higher gas pressures are applied to suppress arcing.

5.   FZ Crystal Growth at Reduced Frequency

5.1   Working Frequency and Risk of Arcing

A limiting factor in the FZ growth of large crystal diameters is the risk of arcing. At high voltages at the inductor corona discharges can be observed. If the voltage at the inductor exceeds the breakdown voltage of the filling gas, an arc forms usually in the main slit of the inductor. Arcing immediately breaks the growth process and must be avoided. The larger the diameter of the growing crystal the more EM power is necessary to melt the large feed and to compensate the losses due to radiation being proportional to the surface area of the hot zone. Hence, more generator power is required and the voltage across the inductor main slit increases.

In the following it is shown that the use of a lower frequency of the inductor current will allow the FZ crystal growth at reduced voltage. Therefore, the higher risk of arcing in the growth of larger crystal diameters can be compensated by using a lower working frequency. The frequency currently used in the industrial FZ growth is $f = 2.6 - 3$ MHz. It is widely known that this frequency allows a stable homogeneous melting of the feed rod. In this chapter it is explained in detail how using a lower frequency deteriorates the melting behavior and what counter measures are applicable. The FZ crystal growth at two lower working frequencies of $f = 2$ MHz and $f = 1.7$ MHz was experimentally investigated.

To give a relation between the frequency and the voltage at the inductor in the FZ system, one may presume that, in a process operated at a reduced frequency, all other process conditions remain unchanged. If the same inductor is applied and all process parameter like pull speed and zone height remain constant, the same Joulean heat flux distribution must be generated to create the temperature field, which is known to allow the growth at the standard frequency.

Indeed, if the frequency is only slightly reduced and the skin depth is still much smaller than the conducting structures, there will be practically no change of the distribution of the surface current density. This is also a consequence of the high-frequency approximation often used to model the EM field in the FZ process [28], [29]. In frame of the high-frequency approximation, assuming that the skin depth is small compared to the conductor dimensions

and the volume current density and the magnetic field in the skin layer are parallel to the surface, the dissipated EM power density can be approximated with:

$$q^{EM} = \frac{i_{ef}^2}{\delta\sigma}, \tag{5.1}$$

where i_{ef} is the effective value of the surface current density. Hence, given that the dissipated EM power density is constant and with the definition of the skin depth $\delta = (\mu\pi_0\sigma f)^{-1/2}$ it follows that:

$$q^{EM} = \frac{i_{ef}^2}{\delta\sigma} = const \qquad \mapsto \qquad i_{ef}^2 \propto \frac{1}{\sqrt{f}} \tag{5.2}$$

Consequently, also the total inductor current I is related to the frequency as:

$$i_{ef} \propto I \propto f^{-1/4} \;. \tag{5.3}$$

It can be seen that a higher current is required to grow at a lower frequency. Assuming that the geometry and the inductance L are independent of the frequency, the proportionality between the voltage across the inductor and the frequency can be found:

$$U = 2\pi f L I \qquad \mapsto \qquad U \propto f I \propto f^{3/4} \tag{5.4}$$

Thus, it can be concluded that the use of a lower working frequency requires less voltage at the inductor terminals to achieve the necessary EM power density on the silicon surfaces.

Generally, the probability for a local breakdown in the main slit is determined by the product of the width of the main slit and the dielectric strength of the filling gas. The filling gas commonly used in the growth chamber is mainly argon. It is well known that a small amount of nitrogen (<1%) added to the gas atmosphere, mainly for the purpose of suppressing the aggregation of voids, significantly increases the dielectric strength of the filling gas. According to Paschen's law the breakdown voltage is a function of the gap distance and the pressure of the gas [77]. However, the risk of arcing during crystal growth is influenced by several process conditions:

- the voltage across the main slit of the inductor
- the width of the main slit in the inductor
- the surface properties of the inductor (sharp edges)
- the pressure and the temperature of the filling gas
- the presence of impurities due to outgassing

Increasing the width of the main slit in the inductor would reduce the risk of arcing but increases the local maximum of the power distribution at the crystal rim, which promotes the generation of dislocations as explained earlier in 3.3. Similarly, increasing the pressure of the gas in the chamber reduces the risk of arcing but may increase thermal stress in the crystal as shown in the previous chapter. Since these measures are exhausted, decreasing the working frequency is another promising option to reduce the risk of arcing.

Experimental Investigation on the Risk of Arcing

To quantitatively evaluate the benefit of reducing the frequency from 3 MHz to 2 MHz and 1.7 MHz respectively, experiments at each of these three frequencies were conducted. In each experiment a crystal cone was grown, whose diameter was increased until arcing was observed. The crystals were grown in a pure argon atmosphere. No nitrogen was added to reduce the breakdown voltage of the filling gas, which was necessary to ensure arcing to happen at a power level within the capability of the HF generator employed for these experiments. In all experiments the same inductor with a main slit width of 1.5 mm was used. The absolute gas pressure was 2 bar.

The results are shown in Table 5-1. At the standard working frequency of 3 MHz, the diameter of the crystal could only be increased up to D=65 mm. It is known that it is not possible to grow a crystal of 4 inch diameter in a pure argon atmosphere at the standard operating frequency. In the experiment in which the frequency was reduced by 1 MHz, a crystal diameter of more than 4 inches could be achieved until arcing ended the experiment. At a frequency of 1.7 MHz the diameter of the crystal could be increased to more than 145 mm.

These results clearly indicate that using lower working frequencies in the given range significantly reduces the risk of arcing. Larger crystal diameters, involving more EM power and higher voltage across the inductor, could be pulled without occurrence of arcing. If nitrogen is added as usual, growing crystals of much larger diameter than achieved in these experiments should be possible.

Table 5-1   Crystal diameters at which arcing was observed

Frequency	Crystal Diameter
f = 3.0 MHz	D= 65mm
f = 2.0 MHz	D=105mm
f = 1.7 MHz	D>145mm

5.2   Melting Behaviour of the Feed Rod

A principal issue when using lower working frequency is to ensure a stable melting behaviour of the feed rod. The homogeneous melting of the feed rod by the inductor is a crucial part in the FZ process. At the typical push rates of the feed rod a layer of 2-5 mm thickness is melted per minute. Due to the surface tension the molten silicon sticks to the solid feed material above and is flowing down through the inductor hole to the molten zone. The temperature in the solid and liquid silicon near the feed surface is governed by the heat balance of the induced EM power, the consumption of latent heat and heat dissipation as a result of radiation and heat conduction into the feed rod. The melting process can be deteriorated by a number of factors and especially a low frequency of the inductor current is known to negatively influence the melting behaviour, which is related to the increase of the skin depth.

Published experimental data on the relationship between melting behaviour and the working frequency is scarce. In [14] Gupta et al. investigate the possibility of using kilohertz frequencies (200 to 500 kHz) in the melting process of silicon rods. It is reported that it is impossible to initiate the melting process at such low frequencies. The penetration depth in solid silicon at 500 kHz is 4mm. The EM heating deep in the feed rod material in combination with the radiative heat loss at the surface leads to melting of inner regions and the formation of solid shells, making it impossible to start the growth process. The precondition for a molten film is that melting temperature at the feed surface can be established by inductive heating. Therefore, a sufficient amount of EM power has to be introduced in the vicinity of the surface of the feed rod. As a result of the skin effect a sufficiently high working frequency is required. In [49] Muiznieks et al. derive a mathematical model to describe the formation and stability of the open melting front on the basis of an overheating concept.

The open melting front of the feed rod is a complicated structure of solid and liquid silicon. In an idealized way this structure can be considered as a thin continuous layer of liquid silicon flowing down below the solid feed rod material above (see Figure 5-1). The melting process can then mathematically be described with a model of a viscous fluid film flowing down the open melting front. The negative influence of the increased skin depth at reduced frequency must be related to the thickness of the thin liquid silicon film.

For modelling the FZ process, an expression for the thickness of such a liquid film at the open melting front was derived by Virbulis [22]. This fluid film model was further improved by Ratnieks et. al in [50]. Gravitation is considered as the driving force for the downward fluid flow. Bioul concludes in [34] that the influence of the Lorentz force on the fluid film is negligibly small.
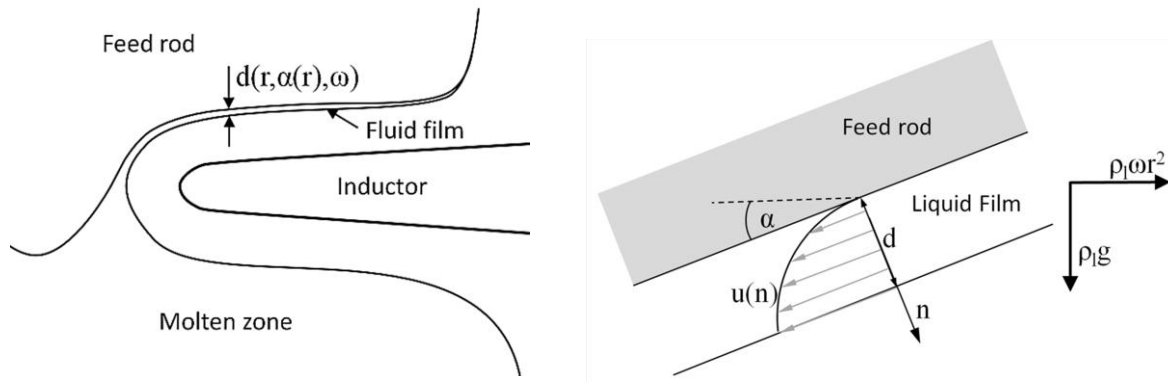
Figure 5-1 Sketch of the open melting front and fluid film.

For the sake of considering the impact of feed rod rotation, in the following the film thickness is given as a function of gravitation and the centrifugal force. It is an experimental evidence that the rotation rate of the feed rod plays an important role for the melting behaviour. While the choice of the crystal rotation rate is more restricted with respect to the stability of the molten zone and the impact on the melt motion (resistivity distribution in the crystal), there are no such restrictions for the feed rod rotation rate, which may be varied in a wide range. Of course due to the centrifugal force, there is an upper limit for the feed rotation rate after which the silicon flows in outward direction. A lower limit exists as the impact of the non-axisymmetric EM power distribution, due to the specific inductor shape, must be averaged by rotating the feed rod.

The film thickness can be given considering a stationary laminar fluid flow in direction of the melt neck. Assuming the velocity u of the liquid silicon in the thin layer does not vary in azimuthal direction, u(n) obeys the Navier-Stokes equation for the specific case:

$$\eta \frac{d^2u}{dn^2} + \rho_l \left(g \sin \alpha - \omega^2 r \cos \alpha \right) = 0,$$

η dynamic viscosity ρ_l density of liquid   (5.5)
g   gravitational constant ω angular velocity

where the inclination angle $\alpha(r)$ is a function of the radial position r and n the coordinate normal to the solid-liquid boundary (see Figure 5-1). Applying the boundary conditions zero velocity at the solid-liquid interface and zero shear stress at the liquid-gas interface the solution for u is

$$u(n) = \frac{\rho_l \left(g \sin \alpha - \omega^2 r \cos \alpha \right)}{2\eta} \left(d^2 - n^2 \right),$$

(5.6)

where d is the thickness of the fluid film. The fluid discharge at a fixed location r is proportional to the integral of the velocity over n and is a function of the local melting rate.

The law of mass conservation gives:

$$\rho_l \, 2\pi r \int\limits_{-d}^{0} u(n)dn = \rho_s \pi \left(R_F - r^2\right)v_F \tag{5.7}$$

where ρ_s is the density of the solid, v_F the push rate and R_F the radius of the feed rod. The integral over u gives the local thickness of the fluid layer:

$$d = \sqrt[3]{\frac{3\eta\rho_s v_F \left(R_F^2 - r^2\right)}{2\rho_l^2 \left(g\sin\alpha - \omega^2\cos\alpha\right)r}} \tag{5.8}$$

The thickness depends on the slope of the open melting front, the local position r and on the specific process parameters. In Figure 5-2 the thickness of the fluid film is plotted for typical process parameters in dependence of the rotation rate $\Omega_F = \omega/2\pi$ and for several typical feed push rates v_F. Comparing the values with the skin depth in liquid silicon ($\delta_l(3\ \text{MHz}) = 0.26\ \text{mm}$), it can be stated that the thickness is in the order of magnitude of the skin depth. Certainly, the thickness is increasing with increasing push rate or feed rotation rate.

Gupta et. al. [48] elaborated on the liquid film thickness during zone refining of silicon rods of smaller diameter (D=65 mm). A film thickness is reconstructed by measurements on longitudinal cuts of an abruptly solidified zone. The measured thicknesses vary from 0.185 mm to 2.03 mm.
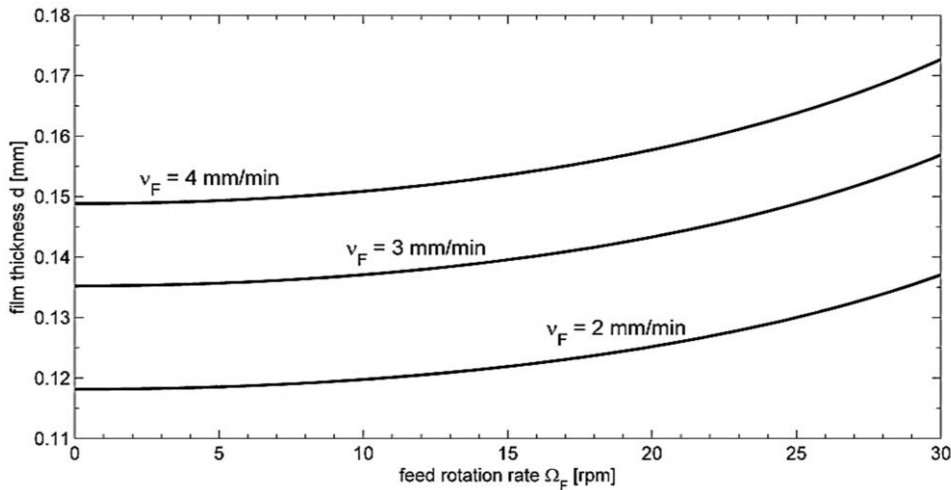
Figure 5-2   Fluid film thickness for typical process parameters.
                        (R_F=51mm, r=R_F/2,α=4°)

Depending on the thickness of the fluid film, some fraction of the Joulean heat flux density q^{EM} is induced into the liquid silicon and the other fraction is induced into the solid bulk of the feed rod. Like in [50], this can be expressed by the power densities as:

$$q^{EM} = q_M^{EM} + q_F^{EM}, \tag{5.9}$$

where q_M^{EM} is the power density generated in the liquid layer and q_F^{EM} the power density induced in the solid covered by the liquid silicon.

The melting behaviour of the feed rod is more favourable if the EM power is mainly induced into the liquid layer. For a stable liquid film, q_M^{EM} must at least exceed the heat dissipation due to radiation and the consumption of latent heat. For modelling the FZ process Ratnieks et al. have derived expressions for the EM power densities in relation to a fictitious power density, which would be induced into a liquid film of infinite thickness (see [50],[31]). Similarly, the dimensionless heat flux ratio between the EM power density in the melt film and the solid can be found as:

$$\frac{q_M^{EM}}{q_F^{EM}} = \frac{e^{\frac{2d}{\delta_l}} - 1}{\sqrt{\sigma_s / \sigma_l}}. \tag{5.10}$$

The heat flux ratio is a function of the film thickness d, the skin depth in the liquid $\delta_l(f)$ and the conductivities. In Figure 5-3 the heat flux ratio is plotted for different frequencies over the range of the film thickness d in question. This allows studying qualitatively at which frequency and thickness of the film the EM power induced into the liquid layer diminishes, if the fluid film model is taken as a basis.

For all frequencies the ratio is zero if no melt film is present (d=0) and tends to infinity if the thickness is very large in comparison to the skin depth, which is the case where practically no EM power is introduced into the solid. It is known that the operating frequency of f = 3MHz allows stable melting of the feed rod. For lower frequency the ratio is decreasing which leads to a lower temperature gradient near the surface of the feed rod.

The heat flux ratio is smaller where the melt film is thinner. The film thickness tends to zero at the feed rod rim, the transition between open melting front and solid feed surface. In this respect the result is in agreement with experimental observations as the melting behaviour becomes instable in the vicinity of the feed rod rim.
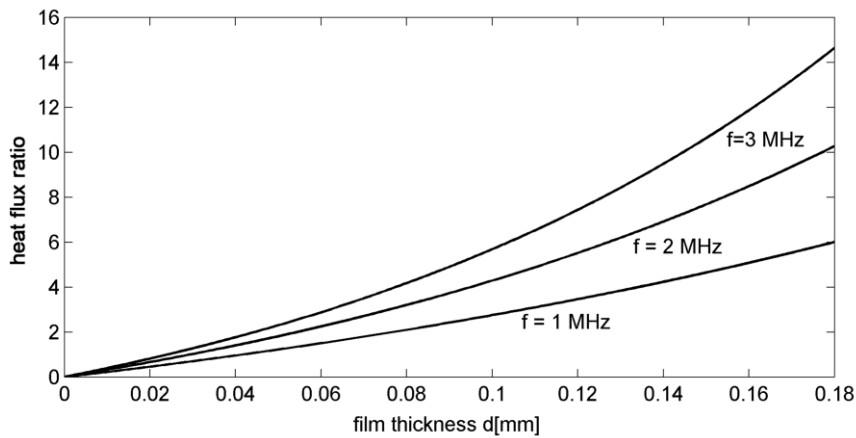
Figure 5-3   Heat flux ratio for different frequencies over the film thickness.

On the other hand, the film thickness can only be regarded as an average value as the solid-liquid structure at the open melting front is much more complicated (Figure 5-4). Due to surface tension effects the liquid silicon does not homogeneously cover the solid feed surface and forms drops or puddles resulting in a liquid structure of non-homogeneous thickness. Regions may appear, where the melt does not cover the solid at all.
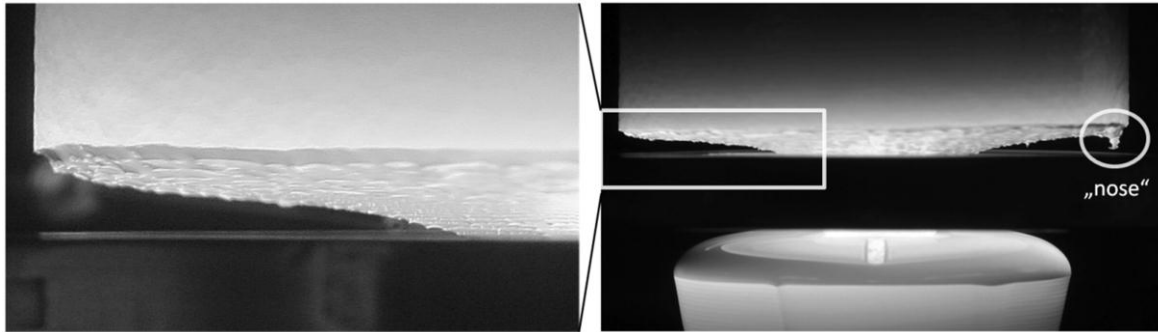

Figure 5-4   The open melting front and formation of a large "nose" during the FZ process. The liquid silicon does not homogeneously cover the feed rod front. The formation of a nose is often observed at the rim of the feed rod.

Formation of Noses

From growth experiments a phenomenon is known, which cannot be explained by the fluid film model only and is scarcely mentioned in the literature: the formation of so-called "noses" at the open melting front (Figure 5-4). The formation of a solid silicon nose often begins in the vicinity of the feed rod rim, where the liquid silicon barely covers the solid. This observation is in agreement with the above conclusion that the melting behaviour deteriorates where the melt film is very thin. Furthermore, the formation of noses is related to the quality of the feed rod. Especially in the case of large grains and a rough surface structure of the feed, nose formation is observed. In this case the melting front is of more non-uniform shape and it is possible that small solid artefacts remain, which are not covered by the liquid and not molten by the induced EM power (see Figure 5-5). Due to the fact that the solid silicon surface of the nose has a higher emissivity ($\varepsilon_s/\varepsilon_l=2.3$) it radiates more heat than the surrounding liquid. Consequently, the nose can self-stabilize and rapidly grow in size as the feed rod is moved downwards with the push rate v_F. As the conductivity of the liquid is about 25 times higher than the conductivity of the solid, the eddy currents are displaced to the thin melt film surrounding the nose as it evolves. The formation of such noses must be avoided as it will break the process if the nose touches the inductor.
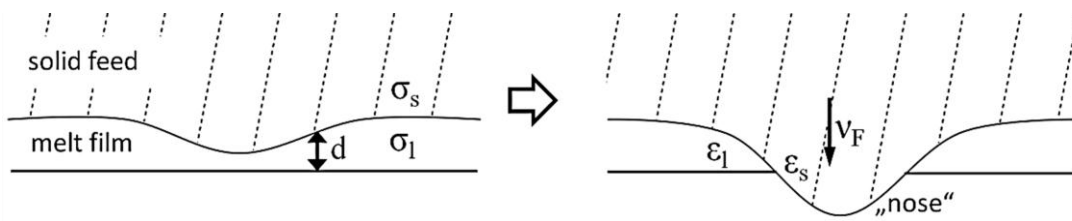
Figure 5-5   The formation of a nose is related to the grain structure of the feed rod and is strongly promoted if lower working frequency is used.

The formation of a nose is a rather stochastic process. The probability of nose formation is strongly related to the frequency of the inductor current. At a high working frequency of about 2.6 to 3 MHz, as currently used in industrial processes, the formation of noses can, usually, be avoided. Nevertheless, also at high frequencies small noses may evolve but they usually do not stabilize. If a small solid artefact has evolved, it is molten by the surrounding melt film such that the formation of a larger nose can be prevented at an early stage. It can be observed that a nose tilts back as it is heated at its base, where it is in contact with the liquid. At reduced frequency less Joulean heat is generated near the surface of the thin liquid film surrounding the nose. Due to the heating in deeper regions the prominent small volume of a solid relict at the surface remains cold. Once a nose of a certain size has evolved, it will be impossible to melt it and break the process.

In [78] it is reported by Wuenscher on nose formation at the open melting front during the growth of germanium single crystals by the FZ technique. The noses appeared if the growth chamber was filled with helium but not in the cases where argon was used. It is concluded that a reduced temperature gradient near the feed surface promoted the formation of noses. Helium has a higher thermal conductivity than argon. Motivated by this observation and solely for the purpose to investigate the influence of the melting behavior in the growth of silicon crystals, an experiment was conducted in a helium atmosphere.

A dislocation-free silicon crystal of a diameter of 30 mm was grown. The growth and melting behavior was found to be not significantly different from that observed in growth experiments in an argon atmosphere. No formation of noses was observed. The growth conditions were similar to those applied in the described growth of germanium, where nose formation was promoted by helium. In a silicon hot zone heat transport by radiation is more dominant than in the case of germanium as a result of the higher melting temperature of silicon. The use of helium as a filling gas in the FZ process for silicon is of no practical benefit and argon is usually preferred because of its low price and higher breakdown voltage reducing the risk of arcing. Hydrogen, which has been used as an ambient for silicon crystal growth is available in high purity and also provides a higher breakdown voltage but gives rise to generation of defects in the crystal [54].

Preventing the Formation of Noses

In the experiments conducted, nose formation was scarce. The formation of a nose is a rather stochastic process. In several growth experiments at 2 MHz no nose formation was observed at all or only small noses formed, which did not stabilize. In most of the cases the noses appeared at the feed rod rim but sometimes noses appeared also in the vicinity of the melt neck during melting the cone of the tapered feed. At f=1.7 MHz frequently larger noses developed and stabilized. This proves that reducing the frequency increases the probability for the formation of noses.

From the observation that nose formation frequently occurs at the feed rod rim where the melt film is thin, one can conclude that by increasing the film thickness the melting behaviour can be improved. The average film thickness can be increased by increasing the rotation rate as shown earlier. In growth experiments conducted at the IKZ Berlin with high feed rotation rates of up to 30 rpm, an improved melting behaviour has been observed [79]. However, high rotation rates can cause undesirable vibrations and oscillations as the feed rod is often not perfectly cylindrical.

In contradiction to the argument above, the formation of noses could be diminished by choosing a relatively low feed rotation rate. The positive influence of the low rotation rate on noses can be explained as follows. At higher rotation rates the impact of the non-axi-symmetric EM field created due to the specific shape of the inductor is averaged over time. The Joulean heat distribution at the open melting front has distinct maxima near the end of the inductor slits. A decrease of the rotation rate of the feed increases the time a nose is exposed to the stronger impact of the EM field above the main slit and the side slits of the inductor. If the timespan the nose is exposed to the impact of the slits is long enough, the Joulean heat induced in the surrounding liquid is sufficient to completely melt the nose. A nose can also be melted if the feed rotation is temporarily stopped in the moment the nose is near to the inductor slit. However, a too low rotation rate will cause a non-uniform temperature field and an asymmetric shape of the melting front. Therefore, only certain rotation rates are appropriate to prevent noses. The region of stability is at very high and low rotation rates, whereas in between these cases, the melting behaviour deteriorates. At moderate feed rotation rates of 2 to 6 rpm the nose formation was strongly promoted. In the 4 inch IKZ process a rotation rate of Ω_F=0.8 rpm was found to be ideal to diminish the formation of noses at reduced frequency.

In the industrial FZ process, the formation of noses must be absolutely avoided. The formation of only one nose will break an expensive process. Therefore, a new concept was investigated to ensure a stable melting process. A key factor in the formation and stabilisation of a nose is the higher emissivity of the solid silicon and the resulting heat dissipation due to radiation at its surface. Therefore, the melting by inductive heating can be

improved if an additional radiation heating system is applied. At reduced frequency, the diminished generation of Joulean heat near the surface can be compensated by thermal radiation, which is well absorbed by the nose due to the relatively high emissivity of the solid. An additional radiation heater can prevent the stabilization of noses.

The setup used to investigate the impact of additional radiative heating is shown in Figure **5-6**. An infrared round tube emitter and a reflector is mounted on top of the inductor. The emitter provides a maximum radiative power of 2 kW and irradiates the open melting front. The water-cooled copper reflector is shaped elliptically at the inside to focus the light at the rim of the feed rod. The ring reflector is not in direct contact to the inductor but it was necessary to slot it near the inductor main slit to avoid inductive coupling. As the reflector on top of the inductor limits the range of vision for the crystal grower, a notch is cut into the inductor to provide visibility of the melting front. The combination of inductive and radiative heating was tested by melting feed rods with very coarse grains, which arise in large fast deposited feed material. Such structures are known to cause noses during the melting process. Therefore, the surface of those feed rods is usually ground prior to the FZ process.

The application of the additional radiative heater completely inhibited the formation of any noses at the open melting front. It is therefore an effective tool for the growth of large diameter crystals at reduced frequency. Furthermore, it can save a step in surface processing of low-quality feed material and reduce costs. The costs of the feed rod material are a substantial factor in the price of an FZ wafer.
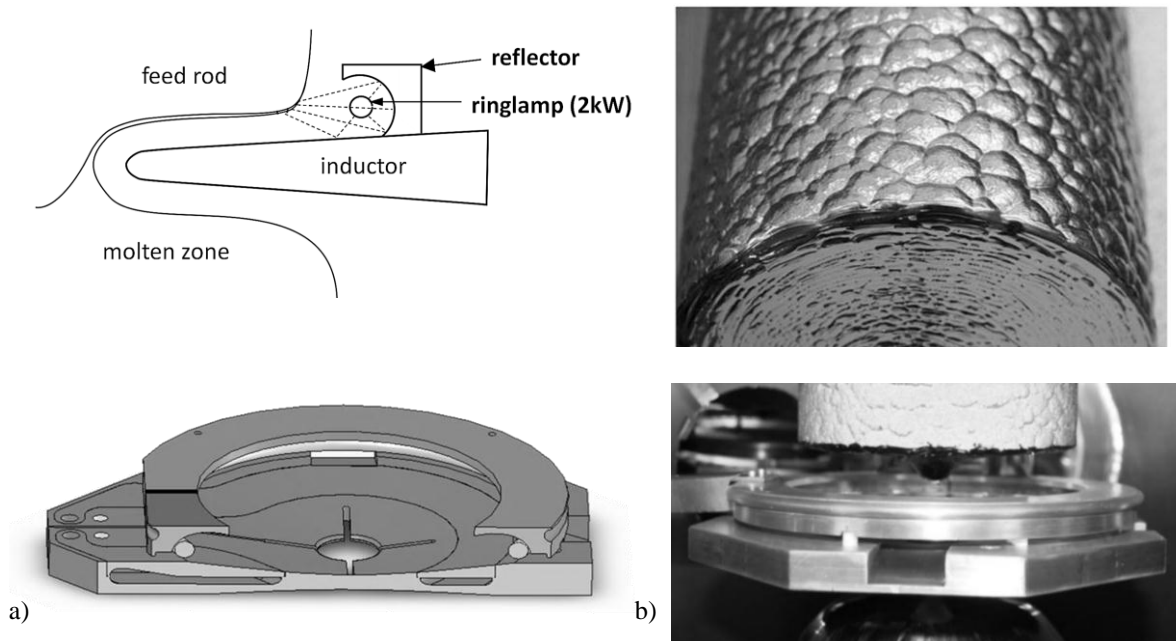
Figure 5-6   a) Radiation heater setup to melt noses.

b) Melting of a feed rod with coarse grains and rough surface structure

5.3   EM Forces

The lower the frequency of the inductor current the stronger is the EM force acting on the molten zone. The EM force influences the molten zone in two ways. It has an impact on the shape of the free melt surface and it is a driving force for the fluid flow in the molten zone. Due to the high frequency, the Lorentz force density is present only in a thin skin layer. In frame of the high-frequency approximation, assuming the magnetic field and the volume current density in the skin layer are parallel to the surface, Ratnieks et al. [29], [50] derived expressions for the time-averaged EM forces at the free melt surface and have shown their applicability for the FZ process [80]. With the definition of the volume force density and the Maxwell equation for the specific case:[1]

$$\mathbf{f} = \mathbf{J} \times \mathbf{B}, \qquad \mu_0 \mathbf{J} = \nabla \times \mathbf{B}, \tag{5.11}$$

the volume force density $\mathbf{f}$ can be decomposed into conservative and non-conservative components:

$$\mathbf{f} = -\frac{1}{2\mu_0} \nabla \left(B^2 \right) + \frac{1}{\mu_0} \left(\mathbf{B}\nabla \right) \mathbf{B}. \tag{5.12}$$

The second part in eq. (5.12) is non-conservative and provides a measure of the ability of the Lorentz force to stir the liquid silicon. It can be written as the force density parallel to the surface:

$$\mathbf{f} = \frac{1}{2\mu_0} \nabla_s \left(B^2 \right), \tag{5.13}$$

where ∇_s is the surface gradient operator. Due to the distinct skin effect it can be assumed that the magnetic field varies only in normal direction and write:

$$B^2 = \mu_0 i_{ef}^2 \exp(-2\xi / \delta), \tag{5.14}$$

where ξ is the local coordinate normal to the surface. By integrating the volume force density over the skin layer the force tangential to the free melt surface can be obtained:

$$\mathbf{F}^{EM} = \frac{1}{4} \mu_0 \delta \nabla_s \left(i_{ef}^2 \right), \tag{5.15}$$

which is also called the EM shear stress. The first part in eq. (5.13) describes a potential force, which causes no flow and is compensated by a pressure gradient in the melt. It gives rise to the EM pressure:

$$p^{EM} = \frac{\mu_0 i_{ef}^2}{2}, \tag{5.16}$$

which can be evaluated at the free surface of the liquid silicon. For a detailed derivation see [29], [50].

---

[1] All quantities are considered as effective in time.

Presuming that the generated EM power density $q^{EM} = i_{ef}^2 / (\sigma\delta)$ is constant, the EM force tangential to the free surface and the EM pressure can be conveniently related to the frequency. Both quantities can be written as a function of the power density as follows:

$$F^{EM} = \frac{1}{4}\delta^2\mu_0\sigma\nabla_s\left(q^{EM}\right), \qquad p^{EM} = \frac{q^{EM}\sigma\delta\mu_0}{2}. \qquad (5.17)$$

Hence, with the definition of the skin depth the following proportionalities are in force:

$$F^{EM} \propto \delta^2 \propto \frac{1}{f}, \qquad\qquad p^{EM} \propto \delta \propto \frac{1}{\sqrt{f}}. \qquad (5.18)$$

It can be seen that the tangential EM force is proportional to the reciprocal of the frequency, whereas the EM pressure is proportional to the reciprocal of the square root of the frequency. Thus, a reduction of the frequency causes strongly increasing EM shear stress but also a higher EM pressure.

Figure 5-7 shows the distribution of the EM force tangential to free melt surface. The surface current distribution is obtained for a 4 inch process and the vectors of the force are calculated with eq. (5.15). The tangential force depends on the surface gradient and the force vectors are directed towards increasing magnitude of the surface current density. Hence, the force vectors at the periphery are directed towards the center of the free surface, where most of the current is induced. Because of the distinct maximum of the surface current below the end of the three side slits of the inductor, also the EM shear stress is particularly strong at these locations in the central region. As a result of the specific shape of the inductor a non-uniform EM force field is acting on the molten zone. Together with the centrifugal force, the buoyancy force and the Marangoni force, the EM force is one of the driving forces for the fluid flow. Therefore, its distribution and magnitude has influence on the resistivity profile in the crystal, which is determined by the flow scheme. In the industrial FZ growth a low radial resistivity variation in the crystal is crucial for the wafer quality and controlling the melt flow is of such high relevance that the literature on this topic is very extensive (see eg. [24], [29]). Raming et al. [27] calculated the melt flow and the resistivity distribution in almost the same range of working frequencies as has experimentally been investigated as a part of this work. The melt flow is calculated for the frequencies 4, 2.8, 2 and 1.5 MHz using a transient, axisymmetric model with spatially fixed phase boundaries. It is concluded that the radial resistivity distribution in the crystal should be more homogeneous at lower frequency, which is in good agreement with the experimental results shown later.

While the melt flow has been extensively studied in the relevant literature, less attention has been paid to the impact of the EM pressure. The EM pressure has not necessarily a stabilizing influence on the melt meniscus. A sudden shutdown of the generator power during growth does not instantly cause a large visible relaxation or collapse of the molten zone, which indicates that the overall impact of the EM pressure is small.
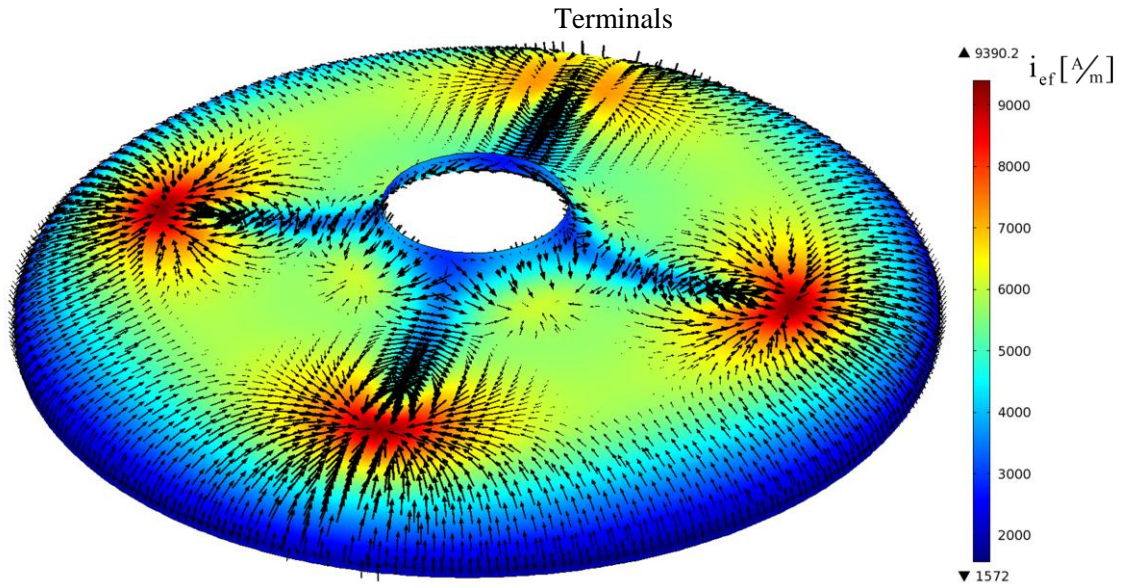
Figure 5-7   Surface current density and vectors of the EM force tangential to the free surface.
              The maximum arrow length in the plot corresponds to a shear stress of 1.1 N/m^2
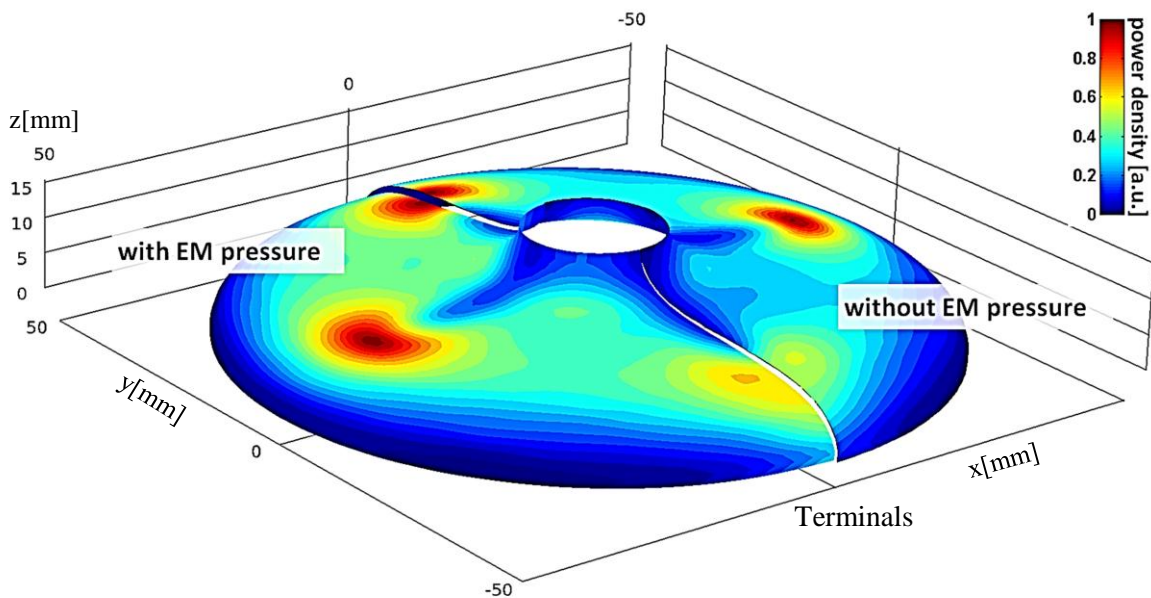   (IKZ 4 inch process, f=3MHz)

Figure 5-8   Calculated EM power density if the EM pressure is neglected (right) and for a case, in
              which the free melt surface is deformed due to the EM pressure (left). Each result is
              mirror-symmetrical to the intersecting plane. (IKZ 4 inch process, f=3MHz)

Figure 5-8 shows the influence of the EM pressure in the numerical model. Two cases are compared. In the first case, the EM power density is calculated for a fixed shape of the free melt surface as it is given by the Laplace-Young equation if the EM pressure is neglected. The sharp maximum of the EM power density near the side slits of the inductor is visible. In the second case, the EM pressure is considered in the calculation as described in (2.3). Taking into account the EM pressure leads to an increase of the distance between melt and inductor in particular in the vicinity of the side slits, where the EM pressure is strong. In this case the maximum is less pronounced and the EM power is more evenly distributed, which is related to the proximity effect causing a concentration of surface current, where the melt is relatively closer to the inductor. The small deflection of the free surface below the slits in the inductor is visible during a process but is hard to photograph or to measure due to light reflections by the inductor and the adverse view angle from the chamber window.

The impact of the EM pressure on the free melt surface shape and, hence, on the EM power distribution increases if the frequency is reduced. Figure 5-9 shows the EM power distribution at the free melt surface for the cases f = 3 MHz and f = 1 MHz. It can be seen that the "smearing" effect is more pronounced. However, as the overall impact of the EM pressure is small, an increase of the pressure has only a minor influence on the free surface shape.

The calculated impact of this change on the azimuthal average of the EM power density is shown in Figure 5-10. This impact is negligibly small for the global temperature field. Considering the isolated influence of the EM pressure no significant impact on the shape of the crystallization interface can be expected.
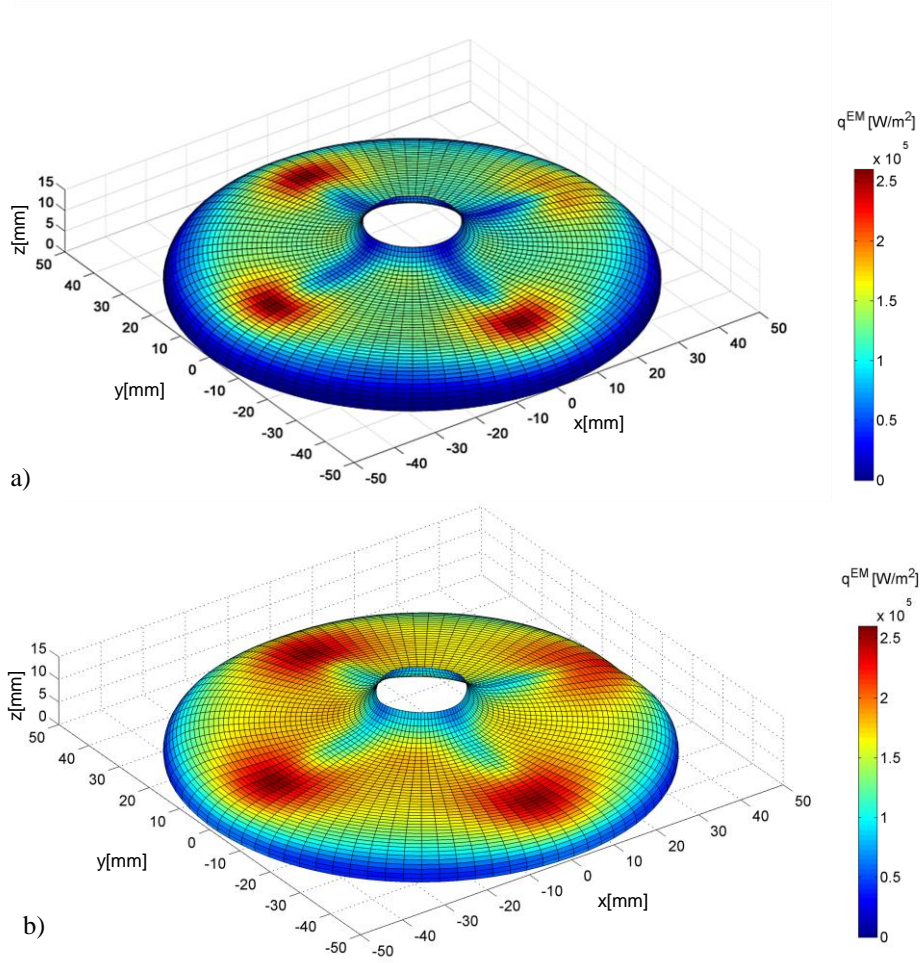
Figure 5-9   EM power density distribution for a frequency of a) 3MHz and b) 1 MHz
                      The free melt surface is deformed due to the EM pressure, which increases
                      with lower frequency. (4 inch process)
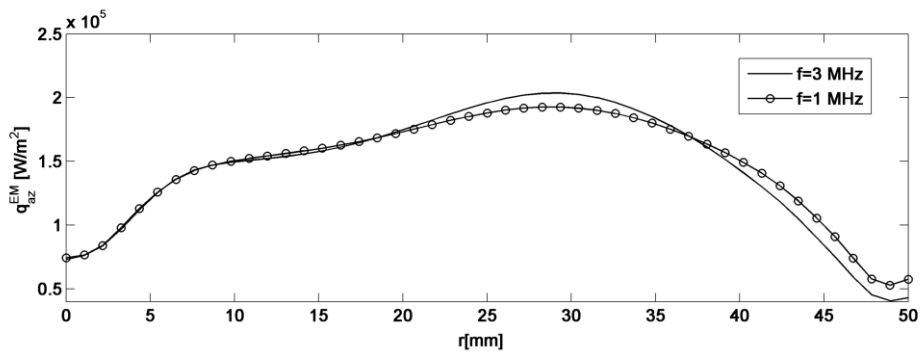
Figure 5-10   Azimuthal average of the EM power density at the free melt surface
                      for different frequencies.

5.4   Formation of Bulges

In the growth experiments at reduced frequency the problem of bulge formation occurred. Moreover, dislocations were generated in the crystals even though all other process conditions were identically to those in the standard process at high frequency allowing the growth of dislocation-free crystals. A main task to enable the dislocation-free growth at lower operating frequency was to overcome these problems. In the following it is shown that both issues can be related to the increased EM pressure. The generation of dislocations as a result of the inhomogeneous Joulean heat generation near the three-phase line in combination with crystal rotation is explained in chapter 3. The inhomogeneity of the EM field is caused by the specific shape of the inductor, i.e. the side slits and the main slit.

Similarly, bulge formation can be a consequence of intense local Joulean heat introduction near the inductor slits. The three-phase line is locally deflected downwards and the melt meniscus bends outwards due to gravity (see Figure 5-11a). It can be observed that the formation of a bulge begins at a crystal facet. At a facet the three-phase line inherently bends downwards and a small melt overhang is formed above it. Once a small bulge has formed, which protrudes from the rim, the deviation from the cylindrical shape is increasing as more Joulean heat is generated in the bulge whenever it is below the inductor slit. At these specific conditions a self-enhancing process is stimulated and the bulge grows in size as the crystal is growing. This causes strong local temperature perturbations near the three-phase line, and this is often followed by generation of dislocations. Later on, a large melt overhang may form above the bulge. This finally leads to melt spillage if the stabilizing surface tension force is exceeded. (see Figure 5-11b).

The principle that the crystal extends in lateral direction near the side slits of the inductor is used in the growth of square-shaped crystals by the FZ method [68]. For the growth of square-like crystals the rotation is fully stopped during the process and, hence, the bulge size is intentionally increased in a controlled manner. Later, corners and faces emerge from the bulges and constitute the square-shaped crystal. Melt spillage is avoided by a special inductor shape. However, the formation of bulges must be avoided if the crystal is rotating.

At some stage during the growth of the cone of the crystal, the radial position of the three-phase line coincidences with the end of the side slits (as explained in (3.2)). During this stage a relatively large amount of Joulean heat is introduced locally at the rim of the crystal, this being a potential risk for the formation of bulges as well as for the generation of dislocations.
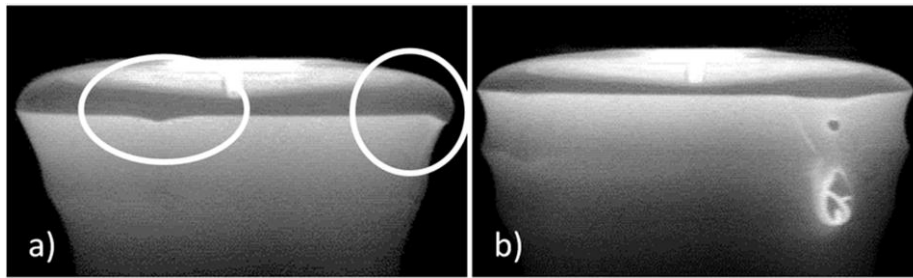
Figure 5-11   Formation of bulges.

a) Bulge formation can be caused by the inhomogeneous Joulean heat generation near the three-phase line in combination with crystal rotation. The three-phase line is locally deflected downwards and a melt overhang forms, which causes irregular lateral growth of the crystal.

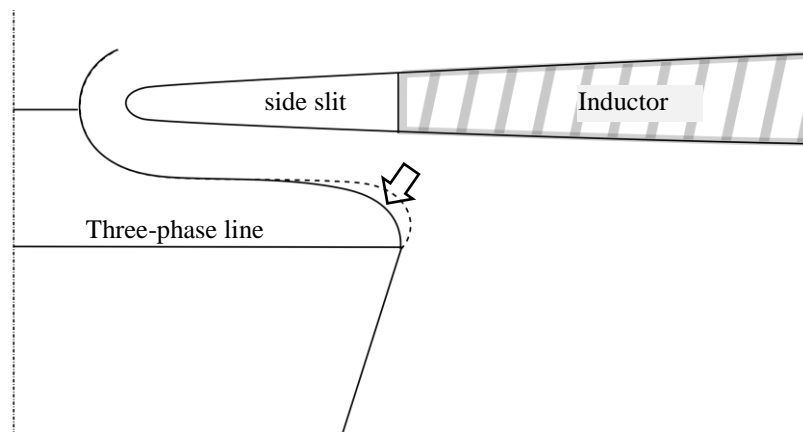b) The formation of a large melt overhang breaks the process due to melt spillage.

Figure 5-12   The EM pressure causes a downward deflection of the free surface below the slit.
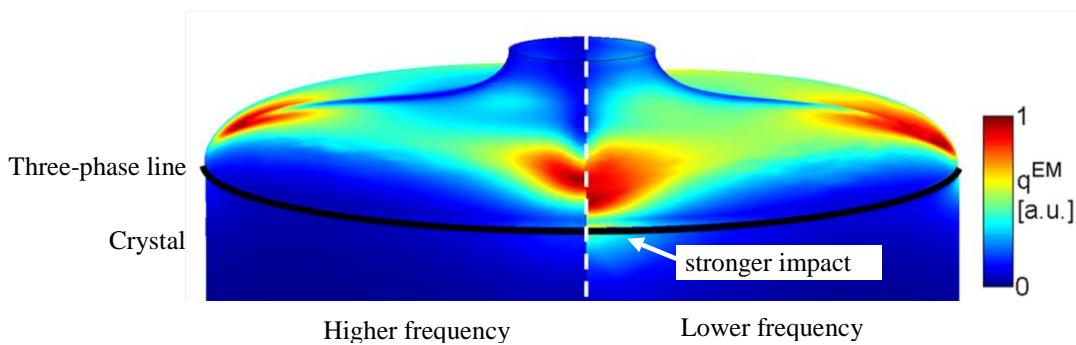
Figure 5-13   Impact of the slit at higher and lower frequency.

Figure 5-12 illustrates the impact of the EM pressure on the free melt surface shape below the inductor slit. Generally, as a result of the positive growth angle there is a melt overhang. For stationary growth conditions this angle has been determined to be 11° in [42]. During the cone phase the growth angle is larger. The melt overhang can be regarded as a shield for the EM field. The presence of a melt overhang prevents a strong generation of Joulean heat near the three-phase line. The deformation of the melt meniscus due to the EM pressure counteracts this alleviating effect. The EM pressure is higher if the frequency is reduced. This leads to a stronger deflection of the free melt surface and, hence, more Joulean heat is generated near the three-phase line below the inductor slits (see Figure 5-13). Therefore, the increase of the EM pressure at reduced frequency causes larger temperature fluctuations near the three-phase-line. This can explain why the generation of dislocations and bulge formation occurred in the growth at reduced frequency.

On the other hand, the observed higher probability for the generation of dislocations could also be related to the stronger EM-forced convection in the molten zone. At lower frequency of the inductor current the convection in the molten zone is more unstable [26], which can lead to higher temperature fluctuations near the crystallization interface. Generally, hydrodynamic instabilities and the resulting temperature oscillations near the crystallization interface can possibly induce dislocations in the crystal [59]. A vertical static magnetic field can suppress oscillations of convection as shown by Raming et al. in [26] by means of a numerical simulation of the melt flow. However, in the conducted experiments generation of dislocations and bulge formation was avoided by modifying the shape of the inductor.

5.5   The Inductor

In the first experiments conducted at a reduced frequency an inductor was used, which was known to allow the stable dislocation-free growth at the standard frequency of 3MHz. The principal shape of this inductor designed for the growth of crystals of a diameter of 4 inches is shown in Figure 5-14a. This inductor showed worse performance in the growth experiments at lower frequency. In many experiments dislocations were generated in the crystal and the described problem of bulge formation occurred even at small crystal diameters, which often led to melt spillage. While it was possible to obtain a 4 inch diameter crystal at a frequency of 2MHz by tuning the growth parameters, the efforts to grow a dislocation-free crystal at 1.7 MHz were not successful.

To overcome these problems a specialized inductor design was developed. The general shape of this optimized inductor is shown in Figure 5-14b. It can be seen that, in comparison to the standard shape, where the slits are of constant width, the slits in the new inductor are uniformly tapered. The area described by the slits is approximately the same in both inductors. This new inductor shape allowed the growth of dislocation-free crystals at reduced working frequency. Photographs of the two different inductor types are given in Figure 5-16 and Figure 5-17. The positive effect of the tapered slits can be explained as follows.

It has been pointed out that the low frequency's adverse effects can be related to the concentration of the generated EM power density near the end of the side slits. The inhomogeneous generation of Joulean heat near the three-phase line can be promoted by the increased EM pressure at lower frequency as explained in (5.4). In Figure 5-15 the impact of the new inductor is compared to that of the standard inductor. It can be seen that the new inductor slit shape leads to a reduction of the maximum of the induced EM power density. Comparing the maxima of the induced EM power densities, in the case with the inductor having tapered side slits the maximum is reduced. The azimuthal average of the power density distribution for the new inductor is approximately similar to that of the standard inductor and, hence, the influence on the global temperature field and the crystallization interface deflection should be comparable, too.

The concentration of the induced current in the vicinity of the end of the side slits is a general problem in the growth of large-diameter crystals. The impact at the end of the side slits is larger if length or width of the slits is increased. This is usually the case in inductors used in growth processes for crystals of larger diameter than the considered 4 inches. Therefore, the proposed slit modification can be beneficial for the growth of large-diameter crystals.
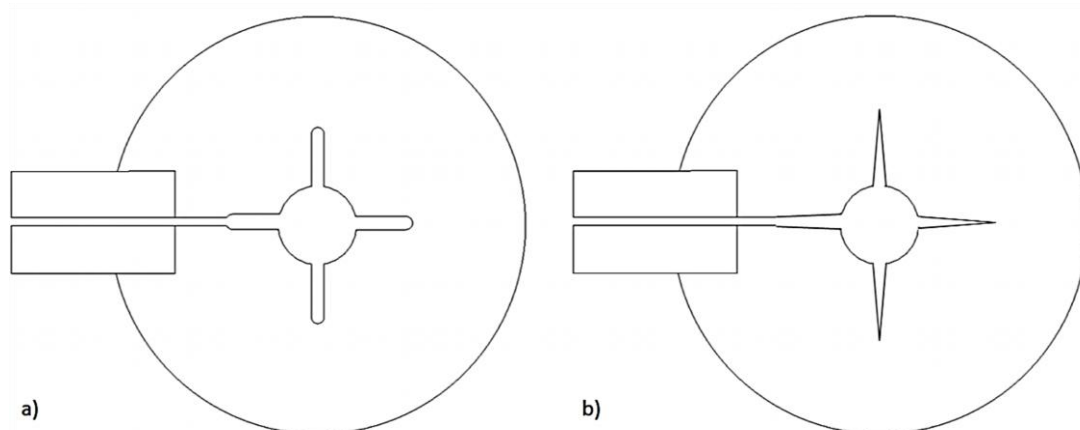
Figure 5-14   Sketch of the different side slit shapes of the standard inductor and the inductor optimized
for the growth at reduced frequency.
a) Side slits of the standard inductor for the 4 inch IKZ process at 3MHz.
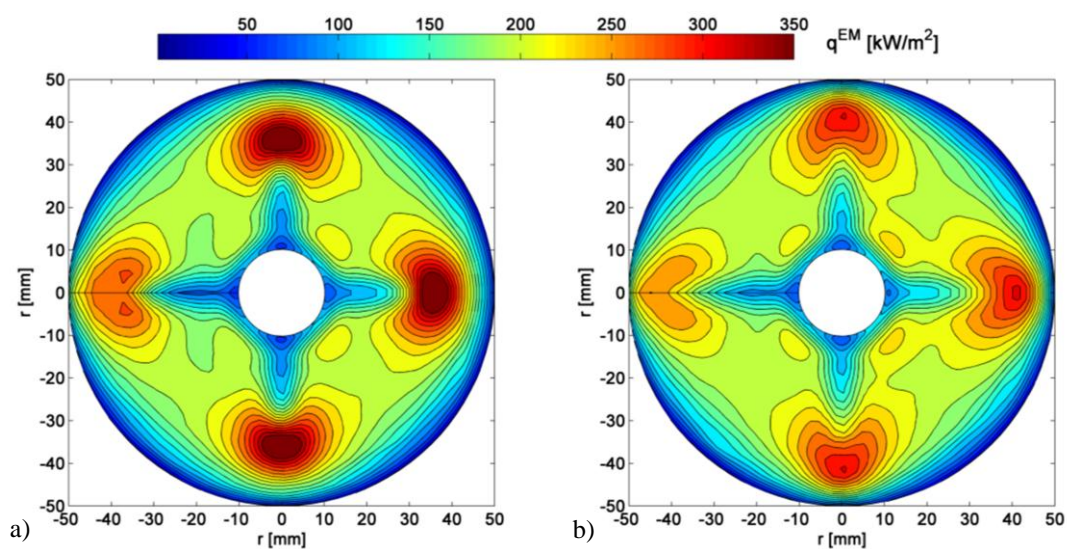b) Modified side slits for the growth at lower working frequency.

Figure 5-15   Calculated EM power density distribution at the free melt surface for
a.) the standard inductor for 3MHz. (distinct maxima near the end of the side slits)
b.) the inductor optimized for use at lower frequency. (the maxima are less pronounced)
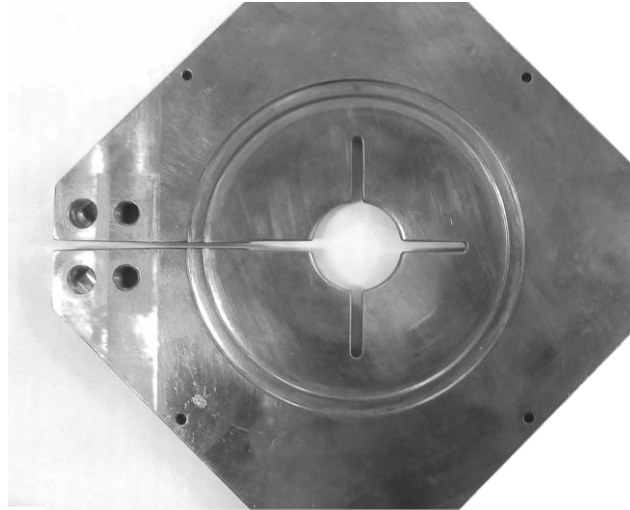
Figure 5-16   A standard inductor for the 4 inch IKZ process at 3MHz operating frequency
                    A standard inductor did not allow the dislocation-free growth at reduced
                    operating frequency.
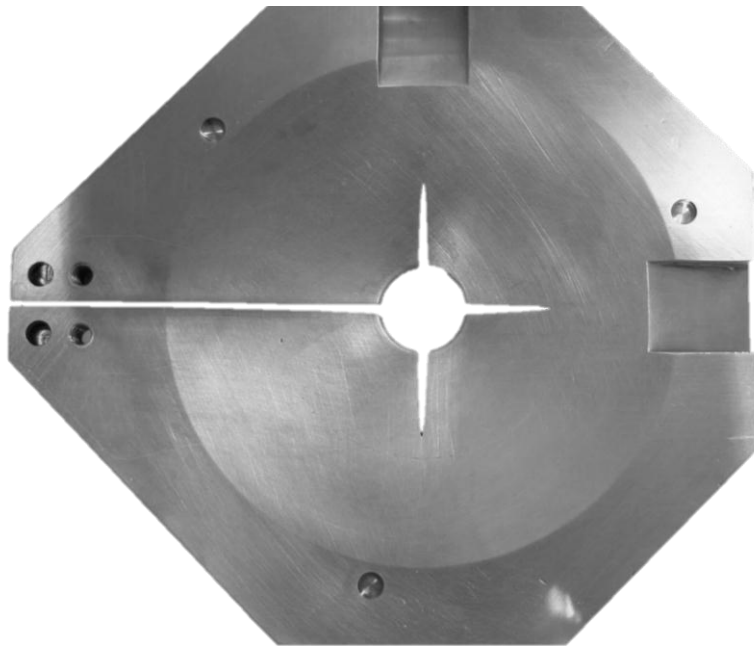
Figure 5-17   Inductor with tapered side slits, optimized for the dislocation-free growth
                    of crystals at lower frequency

The three holes at the periphery were drilled to mount the radiation heater for nose melting
on top of the inductor (see Figure 5-6). The notches at the sides were necessary to allow
view for the operator and to study the melting behavior. The shape of the inductor
periphery has practically no influence on the Joulean heat distribution at the molten zone if
the diameter of the inductor is significantly larger than the diameter of the growing crystal.
The diameter of the inductor for lower frequency was chosen large enough to principally
allow the growth of crystals up to 6 inch.

5.6   Experimental Results

With the inductor optimized for use at reduced frequency, dislocation-free single crystals of 4 inch diameter were grown at 2 MHz and 1.7 MHz (Figure 5-18). The process parameters are shown in Table 5-2. The process parameters are virtually identically to those in the standard IKZ 4 inch process with a frequency of 3 MHz. The difference is the low feed rod rotation rate of only 0.8 rpm, which prevented the formation of noses at the open melting front. The radiation heater on top of the inductor has shown to be an effective measure to prevent nose formation but it was not necessary to apply it as it was possible to prevent noses by tuning the feed rotation rate.
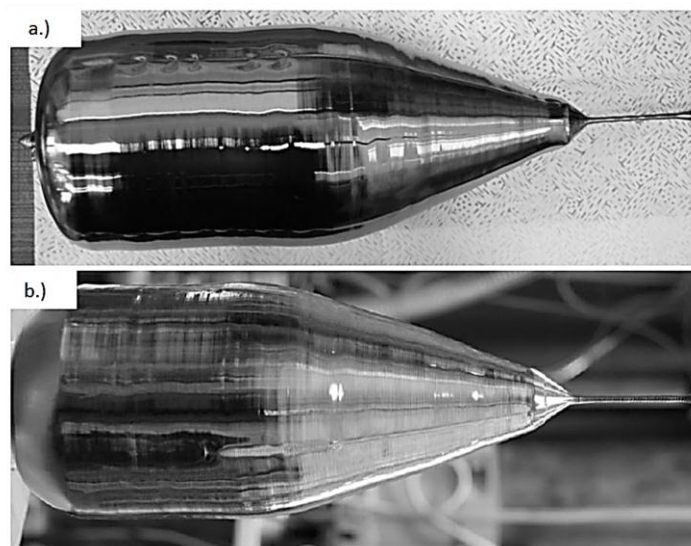
Figure 5-18   Dislocation-free silicon single crystals grown
                              at a.) 2 MHz and b.) 1.7 MHz

Table 5-2   Process parameters for the IKZ 4 inch process at reduced working frequency

Growth parameter	Symbol	Unit	Value
Crystal radius	R_C	mm	51
Crystal rotation	Ω_C	rpm	6
Crystal pull speed	v_C	mm/min	3.4
Feed radius	R_F	mm	50
Feed rotation	Ω_F	rpm	0.8
Zone height	H_C	mm	34

A reference crystal was grown at 3 MHz with identical process parameters and with the same inductor to compare measurements and to study the impact of frequency change on the crystals, independent of the inductor shape. The grown crystals were cut in longitudinal direction to perform resistivity and LPS measurements of the crystallization interface shape.

The LPS measurements of the crystallization interface are shown in Figure 5-19. The maximum deflection of the crystallization interface is considerably increasing the lower the frequency at which the crystal was grown. While the maximum deflection in the crystal grown at f=3 MHz is about 18 mm, it is 20 mm in the crystal grown at f=2 MHz and even 24 mm in the crystal grown at f=1.7 MHz. As the precision of the LPS measurements are in the range of 1 mm, these changes are significant. A deflection of 18mm at 3MHz is typical for the IKZ 4 inch process, whereas the deflection of 24 mm found at 1.7 MHz represents a strong increase of the maximum deflection of the crystallization interface.

It has been shown earlier that the impact of the increased EM pressure is negligible for the global temperature field. Therefore, it must be assumed that the increase of the interface deflection is caused by the stronger EM-forced convection in the molten zone. Three-dimensional transient calculations of the melt motion in the considered IKZ system show, that the frequency decrease leads to an increase of the melt velocity in the whole melt volume and to a totally different vortice structure [81]. However, the influence of the melt flow on the interface deflection on such a large scale could not be explained by the calculations.
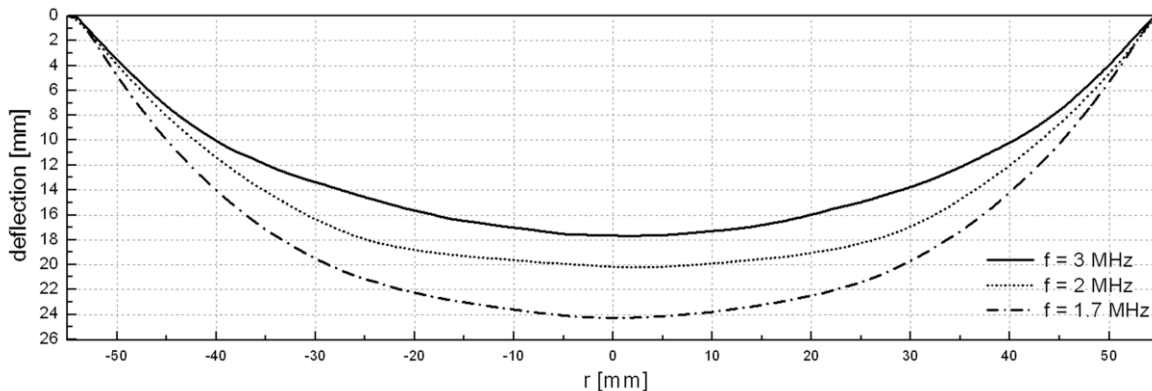
Figure 5-19   Interface shapes measured by the LPS method. The lower the frequency in the process, the larger is the interface deflection measured in the grown crystal.

The combination of buoyancy, surface tension and electromagnetic forces acting on the molten zone creates a characteristic flow scheme. Many authors have calculated the fluid flow in the molten during FZ growth (see e.g. [36], [82]). The impact of the three-dimensionality of the EM field on the melt flow and resistivity distribution in the grown crystals has been studied in [29] by Ratnieks et al. The principal flow pattern can be described as two large counter rotating vortices, which are driven by the buoyancy force acting in the whole melt volume (see Figure 5-20). The Marangoni force, which originates from the temperature dependence of the surface tension, is only present near the free surface and has a weaker influence on the flow. It is directed towards decreasing temperature and, hence, away from the hot center of the free surface in direction to the triple points. The Marangoni force additionally drives the two main vortices. The EM force is directed in opposite direction of the Marangoni force and creates another, smaller vortice near the ETP. In [36] Larsen compares the relative impact of the forces. At the standard working frequency of f=3MHz, the tangential EM force is of the same order of magnitude as the Marangoni force.

If dopants are added, the flow scheme determines the resistivity profile in the crystal. Generally, the radial resistivity profile shows distinct minima, which can be related to the separation point between the two larger vortices, where the flow is directed away from the crystallization interface [26]. As a result of segregation, the dopants in the melt accumulate near the crystallization interface. The flow drags the dopants along the crystallization interface, which results in a high dopant concentration near the flow separation point and, hence, to a resistivity minimum. The position and the sharpness of the resistivity minimum depends on the flow characteristics. Therefore, a principal change of the melt flow due to an increased EM-forced convection can be determined by means of resistivity measurements.
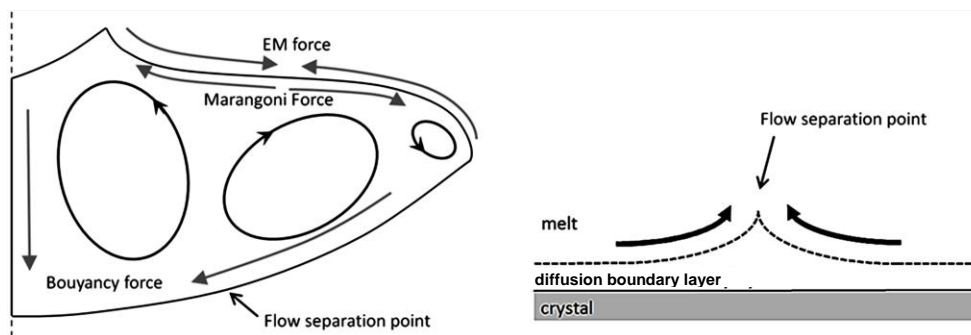

Figure 5-20. Model to explain the resistivity minimum. Source: Raming et al. [25], [26].

The 4-point probe method was used to measure the radial resistivity distribution on longitudinal cuts of the crystals grown at reduced frequency. The results are shown in Figure 5-21. The data points shown are averaged values over measurements at three nearby axial positions at each sample cut from a crystal grown at a specific frequency.

The resistivity distribution measured in the crystal grown at f= 3MHz has the classical shape of a "W". It shows a distinct minimum at $r \approx R_C/2$ and a maximum at r=0. This profile is typically measured in crystals grown at standard process conditions. In comparison to the typical distribution at 3 MHz, the crystals grown at reduced frequency show essential differences in their radial resistivity profile. In the crystal grown at 2MHz, the minimum has moved closer to the crystal center and the maximum in the middle is significantly diminished. The resistivity profile measured in the crystal grown at 1.7 MHz has a completely different character. The resistivity minimum is now at the crystal axis and no "W" shape can be observed at all. In summary, it can be seen that the radial resistivity variation is lower and more homogeneous at reduced frequency.

In [26] Raming et al. predict a better mixing of the dopants in the molten zone and a more homogeneous radial resistivity profile at lower frequency on the basis of a numerical simulation of the melt flow for a similar process. The current experimental result proofs that the increased EM force drastically affects the flow in the molten zone and causes a totally different resistivity distribution.
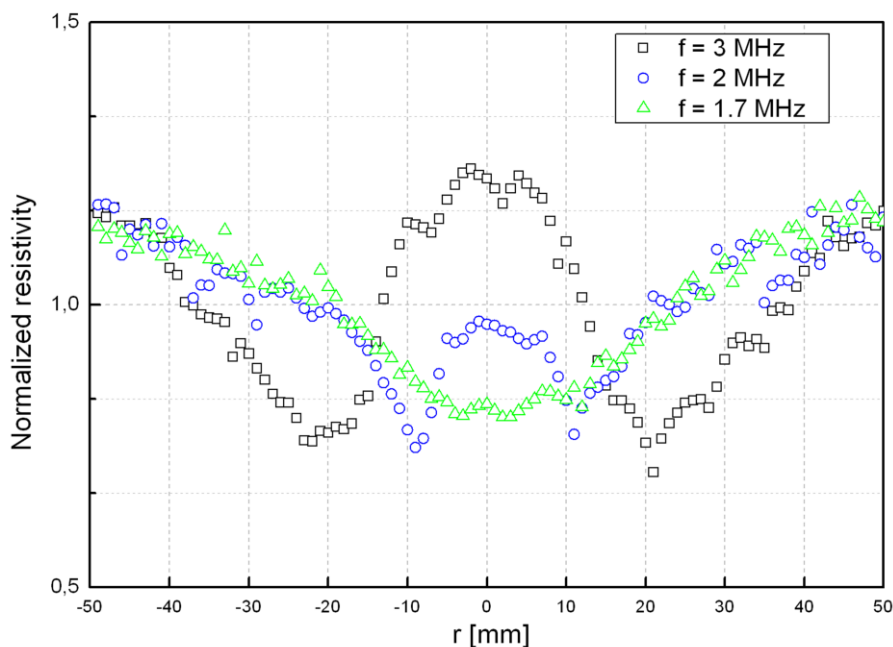
Figure 5-21   RRV measured on longitudinal cuts of the crystals grown at different working frequencies. The crystals grown at reduced frequency show a more homogeneous resistivity profile.

In the industrial FZ process pronounced resistivity variations deteriorate the quality of the wafer, as resistivity specifications in tight bounds have to be met for the electronic device. Therefore, different means are already adopted to decrease the radial resistivity variation and avoid a promoted "W" shape in the industry, for example the counter rotation of the crystal. However, it can be concluded that a reduction of the frequency in the industrial FZ process would not only reduce the risk of arcing but also reduce the radial resistivity variation in the grown crystal.

6.   Summary and Conclusions

In this thesis measures were investigated to overcome known limiting factors in the industrial growth of large-diameter silicon crystals with the FZ method. With the help of numerical simulation solutions were proposed and examined on feasibility by experiments.

As the risk of arcing is a limiting factor in the growth of crystals with large-diameter, a FZ process at lower operating frequency than commonly used was developed. It was exemplarily shown that reducing the frequency from the currently used 2.6-3 MHz down to 2 MHz or 1.7 MHz significantly diminishes the risk of arcing in a growth process. The problem of nose formation at the open melting front was described. It was shown that certain rotation rates or a radiation heater on top of the inductor is effective in avoiding the problem of nose formation at the open melting front. A special inductor shape was presented, which allowed the dislocation-free growth.

For the first time, dislocation-free silicon single crystals of 4 inch diameter were grown with the FZ method using a frequency of the inductor current of 2 MHz and 1.7 MHz respectively. Measurements revealed an increased crystallization interface deflection during the process and a more homogeneous radial resistivity variation in the crystals grown.

For the analysis of the electromagnetic, temperature and thermal stress fields during FZ growth of silicon crystals, a numerical model of the FZ process has been implemented in the software package COMSOL Multiphysics. The model allows calculating the Joulean heat flux distribution in 3D, whereas temperature and thermal stress is computed assuming axial symmetry. The model was validated by comparing calculated and measured crystallization interface shape, which are in good agreement.

The influence of the specific inductor shape was investigated by means of the Joulean heat distribution at the free surface of the molten zone. The impact of a variation of the extents of the slits in the inductor has been studied. Limiting factors for a variation of the slit parameters were explained. The calculations have shown that the inhomogeneity of the EM field due to the impact of the inductor main slit, being a source for the generation of dislocations, is increasing with larger crystal diameter. It was concluded that reducing the width of the main slit is in favor for the dislocation-free growth but increases the risk of arcing.

As high thermal stress is a reason for the generation of dislocations and may cause cracking of large-diameter crystals, the impact of different growth conditions on the thermal stress field was evaluated by numerical simulation. A result was that a reflector decreases thermal stress in the crystal mainly in the center near the crystallization interface and that its influence is limited because it is passive. A calculation showed that an additional radiation heater can be more effective in reducing thermal stress than a reflector. The possibility to grow dislocation-free crystals using an additional radiation heater was shown exemplarily in a growth process for smaller diameters. A temperature measurement indicated that using higher gas pressures may promote convective cooling of the crystal during the FZ process. From a simulation it was concluded that increased heat transfer by convective cooling generates higher thermal stress in the crystal.

7. Appendix

Figure 7-1 and Figure 7-2 show details of the 3D mesh used for the EM field calculation.
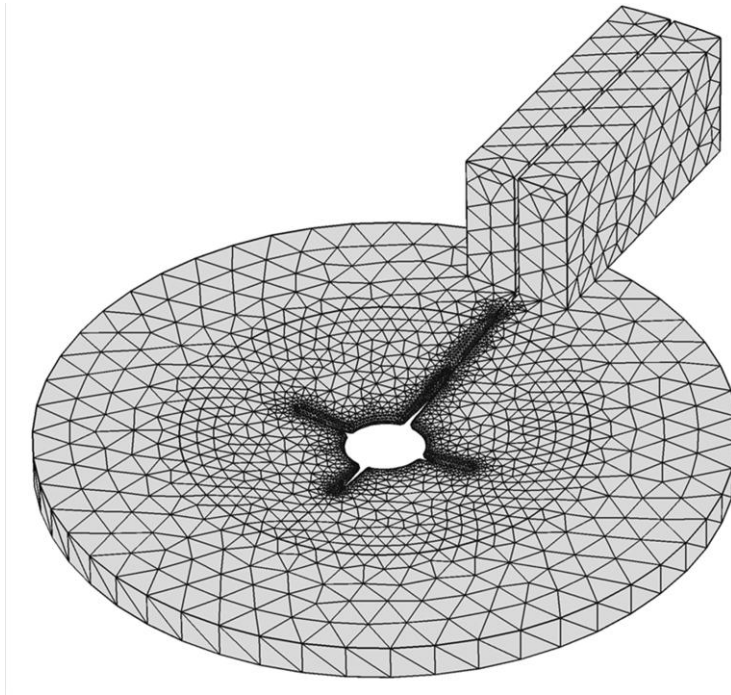
Figure 7-1   18400 triangular elements are used to discretize the surface of the inductor. A
fine mesh is used at the inner edges of the inductor.
(IKZ inductor for a 6 inch process).
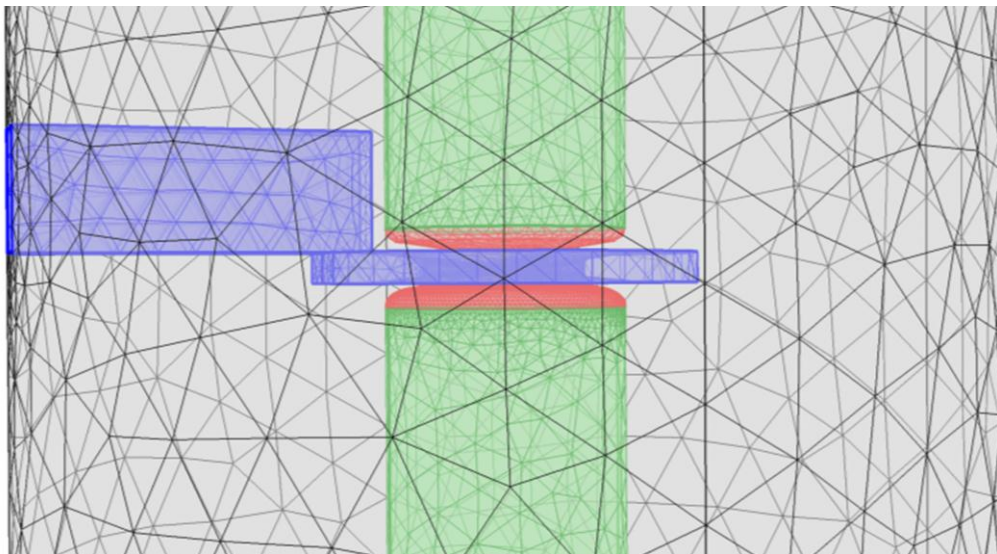
Figure 7-2   The total mesh consists of 65000 3D elements. The calculation time on an Intel®
Core Duo CPU @ 2.66 GHz is about 10 min.

Figure 7-3 shows the mesh used for the temperature and thermal stress analysis

.
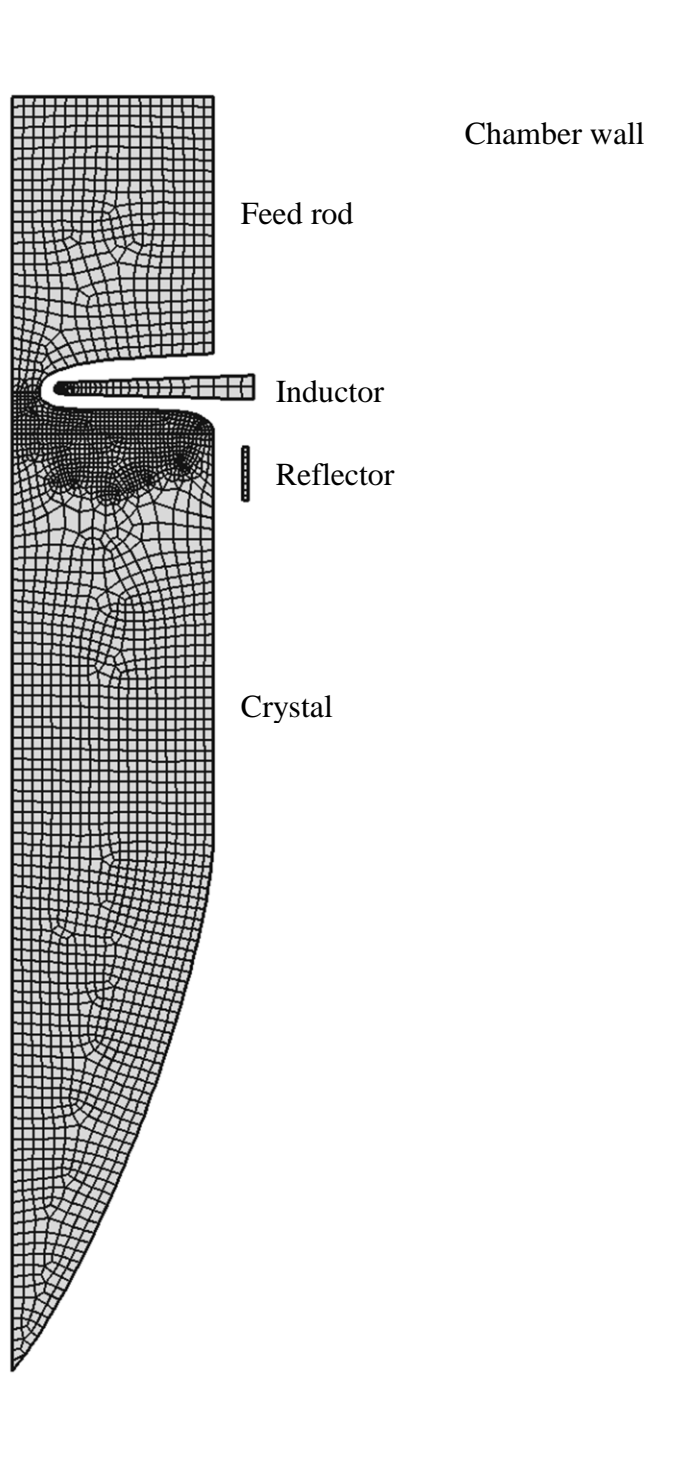
Figure 7-3 2800 quadrilateral 2D mesh elements were used for the thermal stress model.

Figure 7-4 shows the setup for the use of an additional radiation heater in the FZ process.
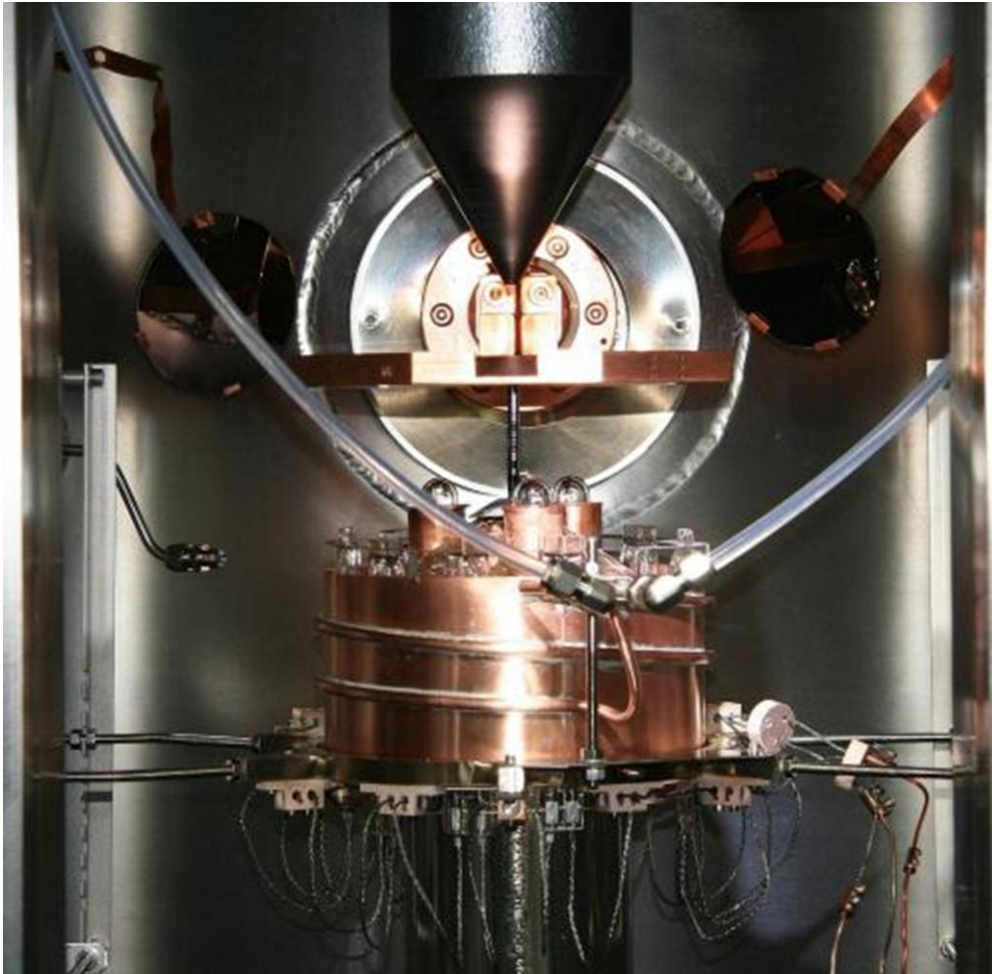
Figure 7-4   The additional radiation heater is mounted below the inductor and is fixed
                    to the chamber walls. The reflector surrounding the lamps is water-cooled.

8.   Bibliography

[1]   P. Becker et al., "Large-scale production of highly enriched 28 Si for the precise determination of the Avogadro constant", *Measurement Science and Technology*, vol. 17, no. 7, pp. 1854–1860, Jul. 2006.

[2]   H. Huang, M. Uder, R. Barthelmess and D. Joerg, "Application of High Power Thyristors in HVDC and FACTS Systems," Siemens AG/Infineon Bipolar, 2008.

[3]   B. J. Baliga, *Fundamentals of Power Semiconductor Devices*. Springer, 2008.

[4]   W. Heywang, "Zur Stabilität senkrechter Schmelzzonen," *Z. Naturforsch*, vol. 11a, p. 238ff, 1956.

[5]   H. J. Fenzl, W. Erdmann, A. Mühlbauer and J.-M. Welter, "Casting of silicon   rods for float-zone crystal growth," *Journal of Crystal Growth*, vol. 68, no. 3, pp. 771–775, Oct. 1984.

[6]   W. von Ammon, "Verfahren zur Herstellung eines Einkristalls aus Silizium durch Umschmelzen von Granulat," Patent EP 2322695B1, 2010.

[7]   M. Bourbina, R. James and McCormick, "Floating Zone Processing of particulate Silicon," Patent US 5.108.7201992, 1991.

[8]   K. Nakajima and N. Usami, *Crystal Growth of Silicon for Solar Cells (Advances in Materials Research)*. Springer, 2009.

[9]   C. W. Dash, "Growth of Silicon Crystals Free from Dislocations.," *Journal of Applied Physics*, vol. 30, pp. 459–474, 1959.

[10]   A. Lüdge, H. Riemann, M. Wünscher, G. Behr and W. Loeser, *Crystal Growth Process Based on Capillarity*. Wiley-Blackwell, 2010, pp. 210 –213.

[11]   W. von Ammon et al., "The impact of nitrogen on the defect aggregation in silicon", *Journal of Crystal Growth*, vol. 226, no. 1, pp. 19–30, Jun. 2001.

[12]   E. Wolf, W. Schröder, H. Riemann and B. Lux, "The influences of carbon, hydrogen and nitrogen on the floating zone growth of four inch silicon crystals," *Materials Science and Engineering: B*, vol. 36, no. 1–3, pp. 209–212, Jan. 1996.

[13] R. Menzel, H.-J. Rost, A. Luedge and H. Riemann, "Influence of reduced working frequencies on the floating-zone growth of silicon single crystals," *Crystal Research and Technology*, vol. 46, no. 10, pp. 1003–1009, Oct. 2011.

[14] H.-J. Rost, R. Menzel, A. Luedge and H. Riemann, "Float-Zone silicon crystal growth at reduced RF frequencies," *Journal of Crystal Growth*, Mar. 2012.

[15] W. Zulehner, "Historical overview of silicon crystal pulling development," *Materials Science and Engineering*, vol. B73, no. 7, 2000.

[16] K. P. Gupta, R. Gregory and M. Rossnick, "Limitations in using kilohertz radio frequencies for float zone silicon crystals," *Journal of Crystal Growth*, vol. 44, no. 44, pp. 526–532, 1978.

[17] H. J. Rost, H. Riemann, A. Luedge and K. Boettcher, "Melting Behavior of As-Deposited Silicon Ingots During the Floating Zone Single Crystal Growth," in *Proceedings of the Fourth International Symposium on High Purity Silicon*, pp. 33–40, 1996.

[18] A. Luedge, S. Hansjoachim, H. Riemann, H. J. Rost and K. Boettcher, "Application of Thermal Shields in the Floating Zone Growth of Silicon," in *Proceedings of the Fourth International Symposium on High Purity Silicon*, pp. 41–48, 1996.

[19] H. Riemann, A. Luedge and K. Boettcher, "Silicon Floating Zone Process: Numerical Modelling of RF Field, Heat Transfer, Thermal Stress and Experimental Proof for 4 inch Crystals.," *Journal of The Electrochemical Society*, vol. 142, no. 3, pp. 1007–1014, 1995.

[20] A. Mühlbauer, A. Muiznieks and G. Raming, "System of Mathematical Models for the Analysis of Industrial FZ-Si-Crystal Growth Processes," *Crystal Research and Technology*, vol. 34, no. 2, pp. 217–226, Feb. 1999.

[21] A. Mühlbauer, A. Muiznieks, J. Virbulis, A. Lüdge and H. Riemann, "Interface shape, heat transfer and fluid flow in the floating zone growth of large silicon crystals with the needle-eye technique," *Journal of Crystal Growth*, vol. 151, no. 1–2, pp. 66–79, May 1995.

[22] J. Virbulis, "Numerische Simulation der Phasengrenzen und Schmelzenströmung bei der Züchtung von Siliziumeinkristallen mit dem Floating-Zone Verfahren," Ph.D. thesis, University of Latvia, Latvia, 1997.

[23] A. Mühlbauer, A. Muiznieks and J. Virbulis, "Analysis of the dopant segregation effects at the floating zone growth of large silicon crystals," *Journal of Crystal Growth*, vol. 180, no. 3–4, pp. 372–380, Oct. 1997.

[24]   A. Mühlbauer et al., "Numerical modelling of the microscopic inhomogeneities during FZ silicon growth," *Journal of Crystal Growth*, vol. 198–199, pp. 107–113, Mar. 1999.

[25]   G. Raming, "Modellierung des industriellen FZ-Prozesses zur Züchtung von Silizium Einkristallen," Ph.D. thesis,Institut für Elektroprozesstechnik, Universität Hannover, 2000.

[26]   G. Raming, A. Muižnieks and A. Mühlbauer, "Numerical investigation of the influence of EM-fields on fluid motion and resistivity distribution during floating-zone growth of large silicon single crystals," *Journal of Crystal Growth*, vol. 230, no. 1–2, pp. 108–117, Aug. 2001.

[27]   G. Ratnieks, "Modelling of phase boundaries for large industrial FZ silicon crystal growth with the needle-eye technique," *Journal of Crystal Growth*, vol. 255, no. 3–4, pp. 227–240, Aug. 2003.

[28]   A. Mühlbauer, A. Muižnieks, A. Jakowitsch, and J. Virbulis, "Berechnung des dreidimensionalen Hochfrequenzfeldes beim Zonenschmelzen von Silizium.," *Archiv für Elektrotechnik*, no. 76, p. 161, 1993.

[29]   G. Ratnieks et al., "Influence of the three dimensionality of the HF electromagnetic field on resistivity variations in Si single crystals during FZ growth," *Journal of Crystal Growth*, vol. 216, no. 1–4, pp. 204–219, Jun. 2000.

[30]   G. Ratnieks, G. Raming, A. Muižnieks and A. Mühlbauer, "Numerical 3D study of FZ growth: dependence on growth parameters and melt instability," *Journal of Crystal Growth*, vol. 230, no. 1–2, pp. 48–56, Aug. 2001.

[31]   G. Ratnieks, "Modelling of the Floating Zone Growth of Silicon Crystals with Diameter up to 8 Inch", Ph.D. thesis, University of Latvia, Latvia, 2007.

[32]   A. Rudevičs, A. Muižnieks, G. Ratnieks, A. Mühlbauer and T. Wetzel, "Numerical study of transient behaviour of molten zone during industrial FZ process for large silicon crystal growth," *Journal of Crystal Growth*, vol. 266, no. 1–3, pp. 54–59, May 2004.

[33]   R. Assaker, "Magnetohydrodynamics in Crystal Growth," Ph.D. thesis, Belgium, June, 1998.

[34]   F. Bioul, "Use of Mathematical Expansions to Model Crystal Growth from the Melt under the Effect of Magnetic Fields," Universite Catholique de Louvain,Belgium, 2007.

[35]   T. L. Larsen, A. Luedge, H. Riemann, J. Leif, A. Nielsen and M. P. Sorensen, "Convective cooling of floating zone silicon crystal during growth," in *Proceedings of the International Colloqium, Modelling of Material Processing*, pp. 18–23, 1999.

[36] T. L. Larsen, "Phosphorus Diffusion in Float Zone Silicon Crystal Growth,", Ph.D. thesis, Technical University of Denmark, Denmark, 2000.

[37] J. D. Jackson, *Classical Electrodynamics Third Edition*. Wiley, 1998.

[38] S. V. Yuferev and N. Ida, *Surface Impedance Boundary Conditions: A Comprehensive Approach*. CRC Press, 2009.

[39] D. J. Hoppe, *Impedance Boundary Conditions In Electromagnetics (Electromagnetics Library)*. CRC Press, 1995.

[40] T. B. A. Seniour, "Impedance boundary conditions for imperfectly conducting surfaces," *Applied Scientific Research, Section B*, vol. 8, pp. 418–436, 1960.

[41] S. CORIELL, S. HARDY and M. CORDES, "Stability of liquid zones," *Journal of Colloid and Interface Science*, vol. 60, no. 1, pp. 126–136, Jun. 1977.

[42] M. Wuenscher, A. Luedge and H. Riemann, "Growth angle and melt meniscus of the RF-heated floating zone in silicon crystal growth," *Journal of Crystal Growth*, vol. 314, pp. 43–47, 2011.

[43] D. N. Riahi and J. S. Walker, "Float zone shape and stability with the electromagnetic body force due to a radio-frequency induction coil," *Journal of Crystal Growth*, vol. 94, no. 3, pp. 635–642, Mar. 1989.

[44] K. H. Lie, J. S. Walker and D. N. Riahi, "Free surface shape and AC electric current distribution for float zone silicon growth with a radio frequeny induction coil," *Journal of Crystal Growth*, vol. 100, pp. 450–458, 1990.

[45] H. Kohno and T. Tanahashi, "Three-dimensional GSMAC-FEM simulations of the deformation process and the flow structure in the floating zone method," *Journal of Crystal Growth*, vol. 237–239, pp. 1870–1875, Apr. 2002.

[46] A. Rudevics, "Non-stationarity and 3D character of the shape of molten silicon during the floating zone crystal growth process,", Ph.D. thesis, University of Latvia, Latvia 2007.

[47] F. P. Incropera and DeWitt, D.P., *Fundamentals of Heat and Mass Transfer*, 4th ed. John Wiley & Sons, 1996.

[48] Z. Guo, S. Maruyama, and S. Togawa, "Radiative Heat Transfer in Silicon Floating Zone Furnace with Specular Reflection on Concave Surfaces," *JSME international journal. Ser. B, Fluids and thermal engineering*, vol. 41, no. 4, pp. 888–894, 1998.

[49] Z. Guo, S. Maruyama, and S. Togawa, "Combined heat transfer in floating zone growth of large silicon crystals with radiation on diffuse and specular surfaces," *Journal of Crystal Growth*, vol. 194, no. 3–4, pp. 321–330, Dec. 1998.

[50]   G. Ratnieks, A. Muižnieks and A. Mühlbauer, "Modelling of phase boundaries for large industrial FZ silicon crystal growth with the needle-eye technique," *Journal of Crystal Growth*, vol. 255, no. 3–4, pp. 227–240, Aug. 2003.

[51]   A. B. Boley and J. H. Weiner, *Theory of thermal stresses*. Mineola: Dover Publications, 1988, p. 243 ff.

[52]   H. A. Mang and G. Hofstetter, *Festigkeitslehre (German Edition)*. Springer, 2008.

[53]   J. F. Nye, *Physical Properties of Crystals*. Oxford University Press, 1985.

[54]   J. P. Hirth and J. Lothe, *Theory of Dislocations*. Krieger Pub Co, p. 872ff, 1992.

[55]   N. Miyazaki, S. Hagihara and T. Munakata, "Elastic constant matrix required for thermal stress analysis of bulk single crystals during Czochralski growth," *Journal of Crystal Growth*, vol. 106, no. 2–3, pp. 149–156, Nov. 1990.

[56]   N. Miyazaki, H. Uchida, S. Hagihara, T. Munakata, and T. Fukuda, "Thermal stress analysis of bulk single crystal during Czochralski growth (comparison between anisotropic analysis and isotropic analysis)," *Journal of Crystal Growth*, vol. 113, no. 1–2, pp. 227–241, Aug. 1991.

[57]   N. Miyazaki, H. Uchida, T. Munakata, K. Fujioka and Y. Sugino, "Thermal stress analysis of silicon bulk single crystal during Czochralski growth," *Journal of Crystal Growth*, vol. 125, no. 1–2, pp. 102–111, Nov. 1992.

[58]   A. Luedge and H. Riemann, "Doping Inhomogeneities in Silicon Crystals Detected by the Lateral Photovoltage Scanning (LPS) Method," *Inst. Phys. Conf. Ser.*, vol. 160, p. 145ff, 1997.

[59]   A. Muižnieks, G. Raming, A. Mühlbauer, J. Virbulis, B. Hanna and W. v. Ammon, "Stress-induced dislocation generation in large FZ- and CZ-silicon single crystals— numerical model and qualitative considerations," *Journal of Crystal Growth*, vol. 230, no. 1–2, pp. 305–313, Aug. 2001.

[60]   W. Keller and A. Muhlbauer, *Floating-Zone Silicon (Preparation and Properties of Solid State Materials 5,* Marcel Dekker Inc, 1981.

[61]   L. D. Landau, *Theory of elasticity*, 3rd English ed., Pergamon Press,, 1986.

[62]   J. Völkl,"Stress in the cooling crystal" in: *Handbook of Crystal Growth: Volume 2 Bulk Crystal Growth.*, p. 823ff,1994.

[63]   W. F. Hosford, *Mechanical Behavior of Materials*. Cambridge University Press, 2005.

[64]   J. Frenkel, *Zeitschrift für angewandte Physik*, vol. 37, no. 572, 1926.

[65]   S. M.-M. Dubois, G.-M. Rignanese, T. Pardoen and J.-C. Charlier, "Ideal strength of silicon: An ab initio study," *Physical Review B*, vol. 74, no. 23, pp. 1–7, Dec. 2006.

[66]   A. J. R. de Kock, P. J. Roksnoer and P. G. T. Boonen, "The introduction of dislocations during the growth of floating-zone silicon crystals as a result of point defect condensation," *Journal of Crystal Growth*, vol. 30, no. 3, pp. 279–294, Oct. 1975.

[67]   E. Schmid and W. Boas, *Plasticity of Crystals*, Chapman and Hall, 1968.

[68]   A. S. Jordan, R. Caruso and A. R. VonNeida, "A Thermoelastic Analysis of Dislocation Generation in Pulled GaAs Crystals," *Bell System Technical Journal*, vol. 59, no. 4, 1980.

[69]   A. S. Jordan, "A comparative study of thermal stress induced dislocation generation in pulled GaAs, InP, and Si crystals," *Journal of Applied Physics*, vol. 52, no. 5, p. 3331, May 1981.

[70]   R. Hull, *Properties of Crystalline Silicon (Emis Series)*, The Institution of Engineering and Technology (IET), 1999.

[71]   J. C. Lambropoulos, "Stresses near the solid-liquid interface during the growth of a Czochralski crystal," *Journal of Crystal Growth*, vol. 80, no. 2, pp. 245–256, Feb. 1987.

[72]   J. C. Lambropoulos and C. N. Delametter, "The effect of interface shape on thermal stress during Czochralski crystal growth," *Journal of Crystal Growth*, vol. 92, no. 3–4, pp. 390–396, Oct. 1988.

[73]   D. E. Bornside, T. A. Kinney and R. A. Brown, "Minimization of thermoelastic stresses in Czochralski grown silicon: application of the integrated system model," *Journal of Crystal Growth*, vol. 108, no. 3–4, pp. 779–805, Feb. 1991.

[74]   O. A. Noghabi, M. M'Hamdi, and M. Jomâa, "Impact of diameter fluctuations on thermal stresses during Czochralski silicon growth," *Journal of Crystal Growth*, doi:10.1016/j.jcrysgro.2011.11.025, Nov. 2011.

[75]   N. Miyazaki, "Solid mechanics and material strength studies on the melt growth of bulk single crystals," *Journal of Crystal Growth*, vol. 300, no. 2, pp. 452–459, Mar. 2007.

[76]   D. Maroudas and R. A. Brown, "On the prediction of dislocation formation in semiconductor crystals grown from the melt: analysis of the Haasen model for plastic deformation dynamics," *Journal of Crystal Growth*, vol. 108, no. 1–2, pp. 399–415, Jan. 1991.

[77]   H. Hess, *Der elektrische Durchschlag in Gasen,* Vieweg Friedr. + Sohn Verlag, 1982.

[78]   M. Wuenscher, "Crucible-free Crystal Growth of Germanium-Experiments and Simulations," Ph.D. thesis, TU Berlin, 2011.

[79]   H. J. Rost, Private communication,IKZ Berlin, 2011.

[80]   K. Dadzis, A. Muiznieks, A. Rudevics and G. Ratnieks, "Precise calculations of the influence of HF EM forces on the melt hydrodynamics for FZ silicon single crystal growth," *Magnetohydrodynamics*, vol. 41, pp. 105–122, Jun. 2005.

[81]   A. Muiznieks, K. Lacis, and A. Sabanskis, "Internal Report - Mathematical modelling of FZ process at lower frequencies," 2011.

[82]   A. Mühlbauer, A. Muižnieks, J. Virbulis, A. Lüdge and H. Riemann, "Interface shape, heat transfer and fluid flow in the floating zone growth of large silicon crystals with the needle eye technique.," *Journal of Crystal Growth*, vol. 151, p. 66, 1995.

Acknowledgements